Detailed Study of the 8 September 2023 Landslides on the Natural Hillside above Yiu Hing Road, Yiu Tung Estate, Shau Kei Wan

GEO Report No. 377

Fugro (Hong Kong) Limited

Geotechnical Engineering Office
Civil Engineering and Development Department
The Government of the Hong Kong
Special Administrative Region

[Blank Page]

Detailed Study of the 8 September 2023 Landslides on the Natural Hillside above Yiu Hing Road, Yiu Tung Estate, Shau Kei Wan

GEO Report No. 377

Fugro (Hong Kong) Limited

This report was originally produced in November 2024
as GEO Landslide Study Report No. LSR 8/2024
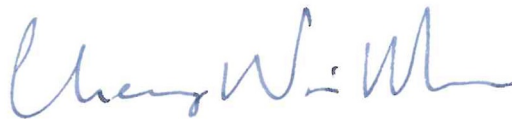
Preface

In keeping with our policy of releasing information which may be of general interest to the geotechnical profession and the public, we make available selected internal reports in a series of publications termed the GEO Report series. The GEO Reports can be downloaded from the website of the Civil Engineering and Development Department (http://www.cedd.gov.hk) on the Internet.

Raymond W M Cheung
Head, Geotechnical Engineering Office
August 2025

Foreword

This report presents the detailed study of a major landslide incident (Incident No. 2023/09/3235) that occurred on the natural hillside above two roadside registered cut slopes (slope Nos. 11SE-A/CR781 and 11SE-A/C782) on Yiu Hing Road near Yiu Hing House and Yiu Kwai House of Yiu Tung Estate, Shau Kei Wan. The incident occurred during a record-breaking severe rainstorm at around 2:36 a.m. on 8 September 2023. Both Black Rainstorm Warning and Landslip Warning were in effect at the time. Two landslides occurred with a total estimated failure volume of about 4,000 m^3. The upper landslide was a small-scale, translational debris avalanche on an open hillslope with an estimated failure volume of about 100 m^3 and the majority of the landslide debris was deposited on the natural hillside. The lower landslide was a massive-scale, structurally controlled translational rockslide on a spur with an estimated failure volume of about 3,900 m^3. Some of the landslide debris was deposited over the crest and berms of the cut slopes, and the rest of the debris blocked a section of Yiu Hing Road, leading to its closure for several months. While there were no casualties, the landslide debris caused varying degrees of damage to the nearby facilities. Given the severity and close proximity to densely populated high-rise residential buildings in urban area, it received widespread media coverage.

The key objectives of the study were to document the facts about the incident, present relevant background information and establish the probable causes of the landslides. The discussion and views expressed in this report are not intended to establish the existence of any duty of law on the part of the Government of the Hong Kong Special Administrative Region (HKSARG), its employees or agents, contractors, their employees or agents, or subcontractors, or any other party. This report neither determines nor implies liability towards any organisation or individual except so far as necessary to achieve the said objectives.

We gratefully acknowledge assistance from the Civil Aid Service, the Survey Division of the Civil Engineering and Development Department, and the technical support provided by AECOM Asia Company Limited, the 2022 to 2024 Landslide Investigation Consultants, and Ove Arup & Partners Hong Kong Limited, the Landslip Prevention and Mitigation Consultants.

This report was prepared for the Geotechnical Engineering Office of the Civil Engineering and Development Department under Agreement No. CE 29/2021 (GE). This is one of a series of reports produced during the consultancy by Fugro (Hong Kong) Limited. Unless otherwise agreed in writing, Fugro (Hong Kong) Limited accepts no responsibility for any use of, or reliance on any contents of this Report by any person other than HKSARG or its employees or agents and shall not be liable to any person other than HKSARG or its employees or agents, on any ground, for any loss, damage or expense arising from such use or reliance.

Y C Koo
Project Director
Fugro (Hong Kong) Limited

Agreement No. CE 29/2021 (GE)
Study of Landslides Occurring on
Hong Kong Island and Outlying
Islands between 2022 and 2024 –
Feasibility Study

Contents

List of Tables

List of Figures

1   Introduction

On the early morning of 8 September 2023, a major landslide incident (Incident No. 2023/09/3235) occurred on the natural hillside above Yiu Hing Road, Yiu Tung Estate, Shau Kei Wan, Hong Kong (Figures 1.1 and 1.2). The incident took place during a record-breaking severe rainstorm, with both Black Rainstorm Warning and Landslip Warning in force. Based on witness accounts and closed-circuit television (CCTV) footage, the incident occurred at about 2:36 a.m. It involved two landslides with a total estimated failure volume of about 4,000 m^3:

(a) a small-scale, translational debris avalanche at the upper southeast corner of the landslide site (upper landslide), and

(b) a massive-scale, structurally controlled, translational rockslide with a basal failure plane along a persistent, locally stepped, undulating to planar sheeting joint in the central and lower areas of the landslide site (lower landslide).

As a result, some landslide debris was deposited on two roadside registered cut slopes (slope Nos. 11SE-A/CR781 and 11SE-A/C782), and the remaining debris completely blocked both lanes of a section of Yiu Hing Road, leading to its closure for several months. Although there were no casualties, the landslide debris caused varying degrees of damage to the road, subsurface drainage pipes, a lamp post, a bus stop, several parked vehicles, basketball and volleyball courts and their steel perimeter fences, and a window pane on the first floor of Yiu Kwai House (Figure 1.3). The incident received widespread media coverage due to its severity and consequences.

Following the incident, Fugro (Hong Kong) Limited (Fugro) conducted a detailed study of the incident for the Geotechnical Engineering Office (GEO) of the Civil Engineering and Development Department (CEDD) under Agreement No. CE 29/2021 (GE). Fugro received assistance from the Civil Aid Service (CAS), the Survey Division of the CEDD, and technical support provided by AECOM Asia Company Limited (AECOM), the 2022 to 2024 Landslide Investigation Consultants, under Agreement No. CE 30/2021 (GE), and Ove Arup and Partners Hong Kong Limited (Arup), the Landslip Prevention and Mitigation Consultants under Agreement No. CE 24/2018 (GE).

The key objectives of the study were to document the facts about the incident, present relevant background information and establish the probable causes of the landslides. This report presents the findings of the study, which consists of the following tasks:

(a) a review of all known relevant documentation relating to the landslide site,

(b) interviews with eyewitnesses of the incident,

(c) aerial photograph interpretation (API), geological mapping, topographic surveys, site inspections, and field measurements at the landslide site,

(d) an analysis of rainfall records and engineering analyses, and

(e) a diagnosis of the probable causes of the landslides.
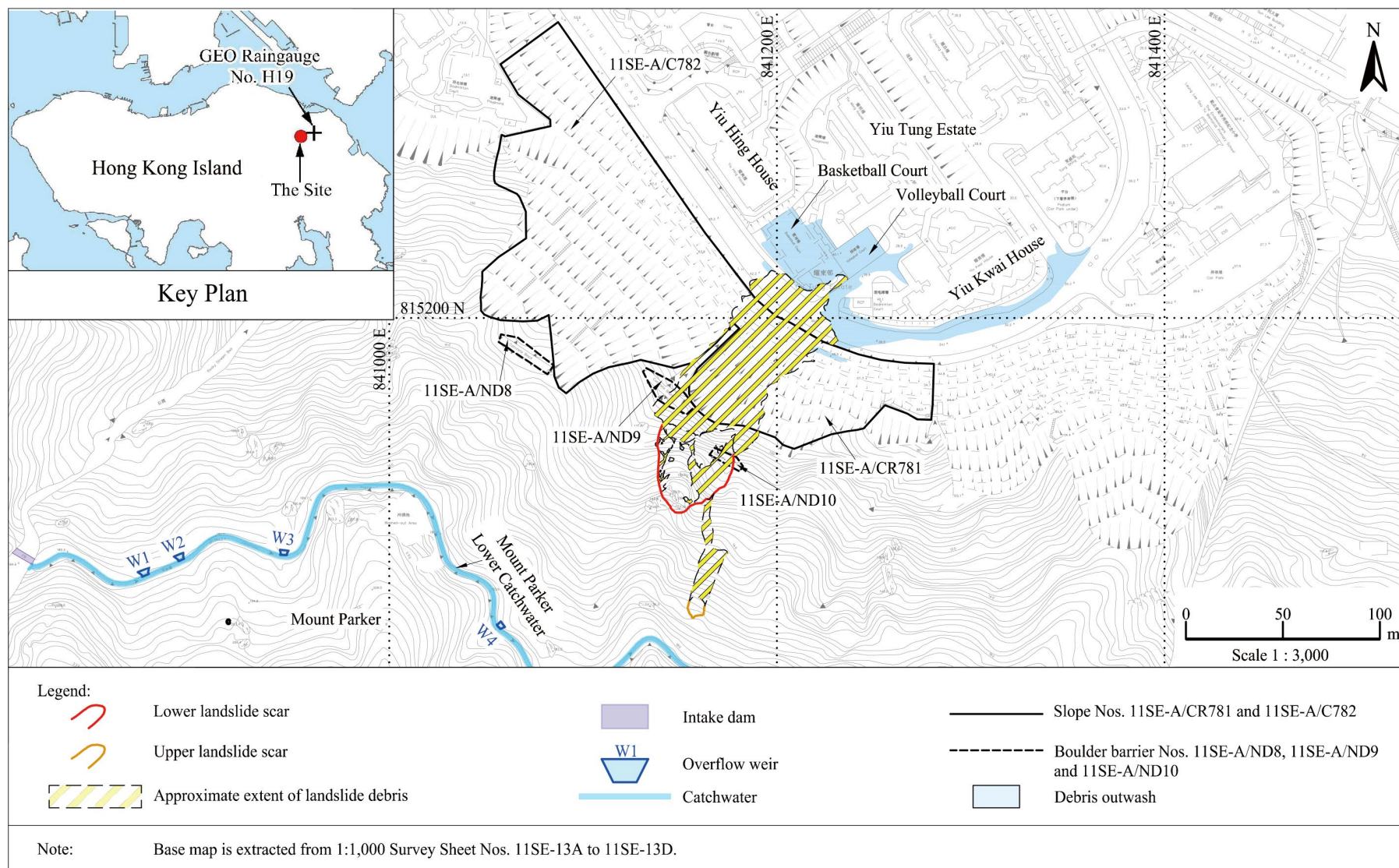
Figure 1.1   Location Plan
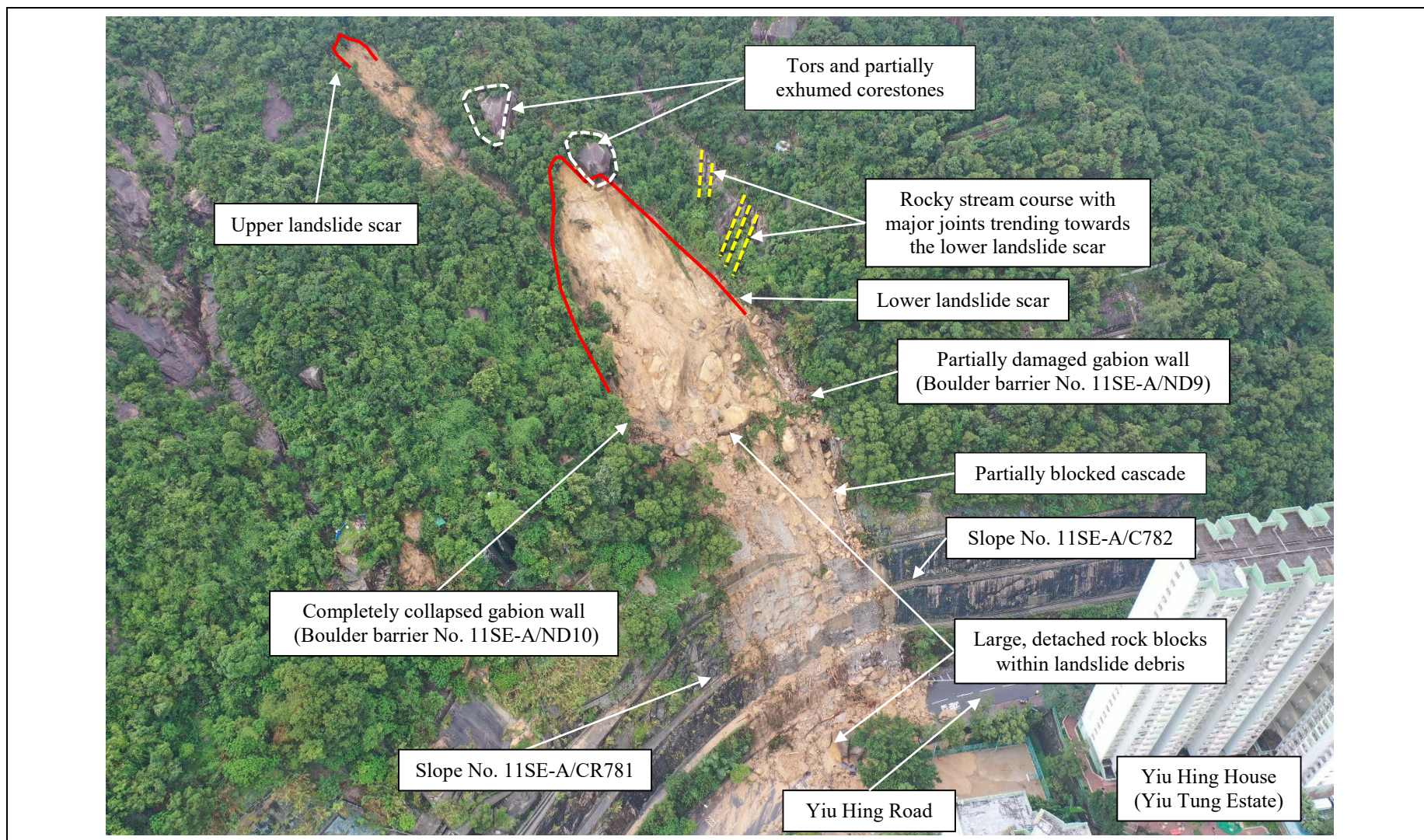
Figure 1.2   General View of the Landslide Site (Photograph taken on 9 September 2023)

Surface water overflowed to slope No. 11SE-A/CR781 after the cascade was partially blocked by landslide debris

Landslide debris completely blocked a section of Yiu Hing Road
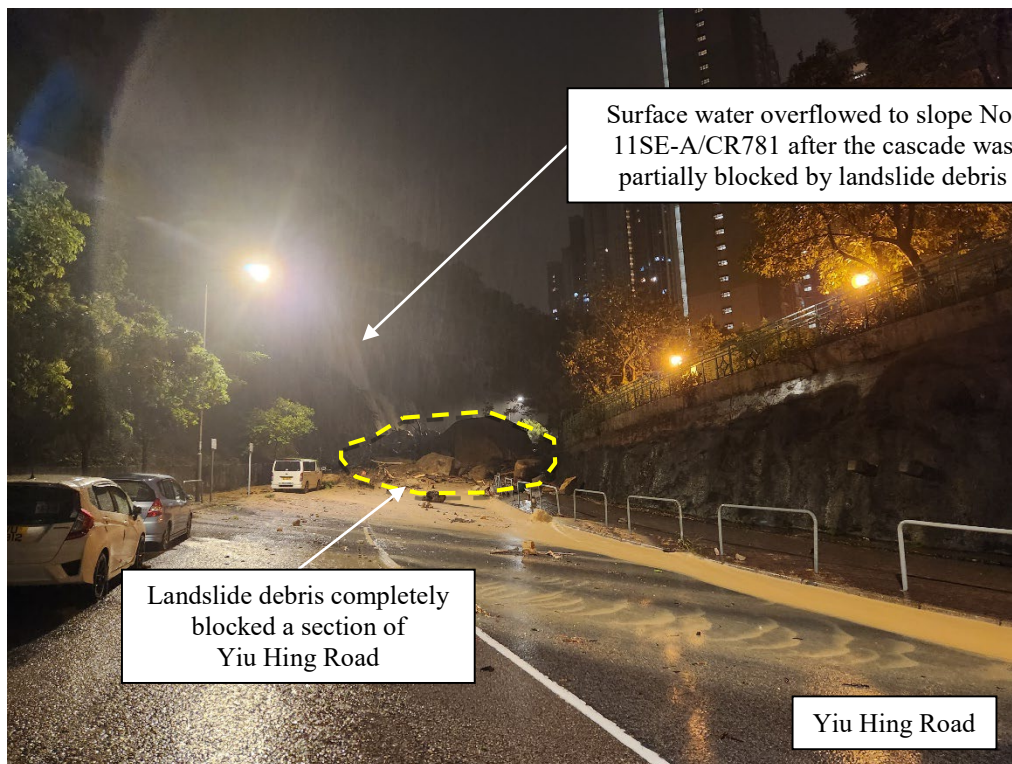
Yiu Hing Road

a)   General View of Yiu Hing Road after the Incident

Natural hillside

Slope No. 11SE-A/C782

Landslide debris comprised many sizable rock blocks

Bus stop

Yiu Hing Road

b)   Complete Blockage of Yiu Hing Road after the Incident

Figure 1.3   Consequences of the Incident (Photographs taken on 8 September 2023) (Sheet 1 of 2)

c) Minor Damage to Vehicles Parked along Yiu Hing Road

d) Basketball Court and Building Damaged by the Landslide Debris

Figure 1.3   Consequences of the Incident (Photographs taken on 8 September 2023) (Sheet 2 of 2)

2 The Site

2.1 Site Description

The landslide site is situated on a northeast-facing natural hillside above two registered slope Nos. 11SE-A/CR781 and 11SE-A/C782 (hereafter referred to as 'the cut slopes' unless otherwise specified) near Yiu Hing House and Yiu Kwai House of Yiu Tung Estate, Shau Kei Wan (Figures 1.1 and 1.2). The incident consisted of an upper landslide and a lower landslide. The lower landslide is significantly larger than the upper landslide, and most of the information and discussion in this study pertains to the lower landslide.

The natural hillside is characterised by an extensive broad catchment (hereafter referred to as 'the study area' unless otherwise specified) with a plan area of about 90,000 m^2. The study area extends from an elevation of about +456 mPD at its highest point to about +90 mPD at the crest of slope No. 11SE-A/CR781 adjacent to Yiu Hing Road. Yiu Hing Road is a two-lane, two-way carriageway that runs immediately along the toe of the study area and descends slightly to the southeast.

The lower landslide is situated on a spurline between a rocky stream course and a topographic depression, while the upper landslide is situated at the site of a topographic depression. The crown of the lower landslide scar is about 100 m (+138 mPD) above Yiu Hing Road, while the crown of the upper landslide scar is about 30 m (+168 mPD) above the lower landslide scar and about 12 m below the catchwater (Figure 2.1).

The hillside adjacent to the landslide site is densely vegetated with shrubs and mature trees and has an incline of approximately 40° to 45°. Exhumed corestones and tors are present on the spurline at the landslide site, and rock outcrops with distinct, persistent northeast-southwest joint patterns are present in the adjacent hillside and within the rocky stream course (Figure 1.2).

Within and near the study area, there are two cut slopes and three gabion walls (boulder barrier Nos. 11SE-A/ND8, 11SE-A/ND9 and 11SE-A/ND10) (hereafter referred to as 'gabion wall ND8', 'gabion wall ND9', and 'gabion wall ND10' respectively unless otherwise specified).

Slope No. 11SE-A/CR781 is a 120 m-long soil and rock cut slope, and has an average gradient of 50° and a maximum height of 55 m. The lower rock cut portion of the slope contains three 10 m-high, sub-vertical batters separated by 1.6 m-wide berms and has a maximum inclination of approximately 70°. The upper soil cut portion of the slope is partially vegetated, with stone pitching and occasional shotcrete cover on steepened slope faces. It has three 6 m-high batters separated by 1.6 m-wide berms inclining at 40°. A 7 m-high and 65 m-long concrete retaining wall separates the lower rock and upper soil cut portions.

Slope No. 11SE-A/C782 is a 180 m-long soil and rock cut slope with an average gradient of about 45° and a maximum height of 85 m. The lower rock cut portion of the slope contains seven 6.5 m-high, sub-vertical batters separated by 1 m-wide berms and has a maximum inclination of about 70°. The upper soil cut portion of the slope, inclining at 30° to 35°, is generally vegetated and has four 5 m-high batters separated by 1 m-wide berms.
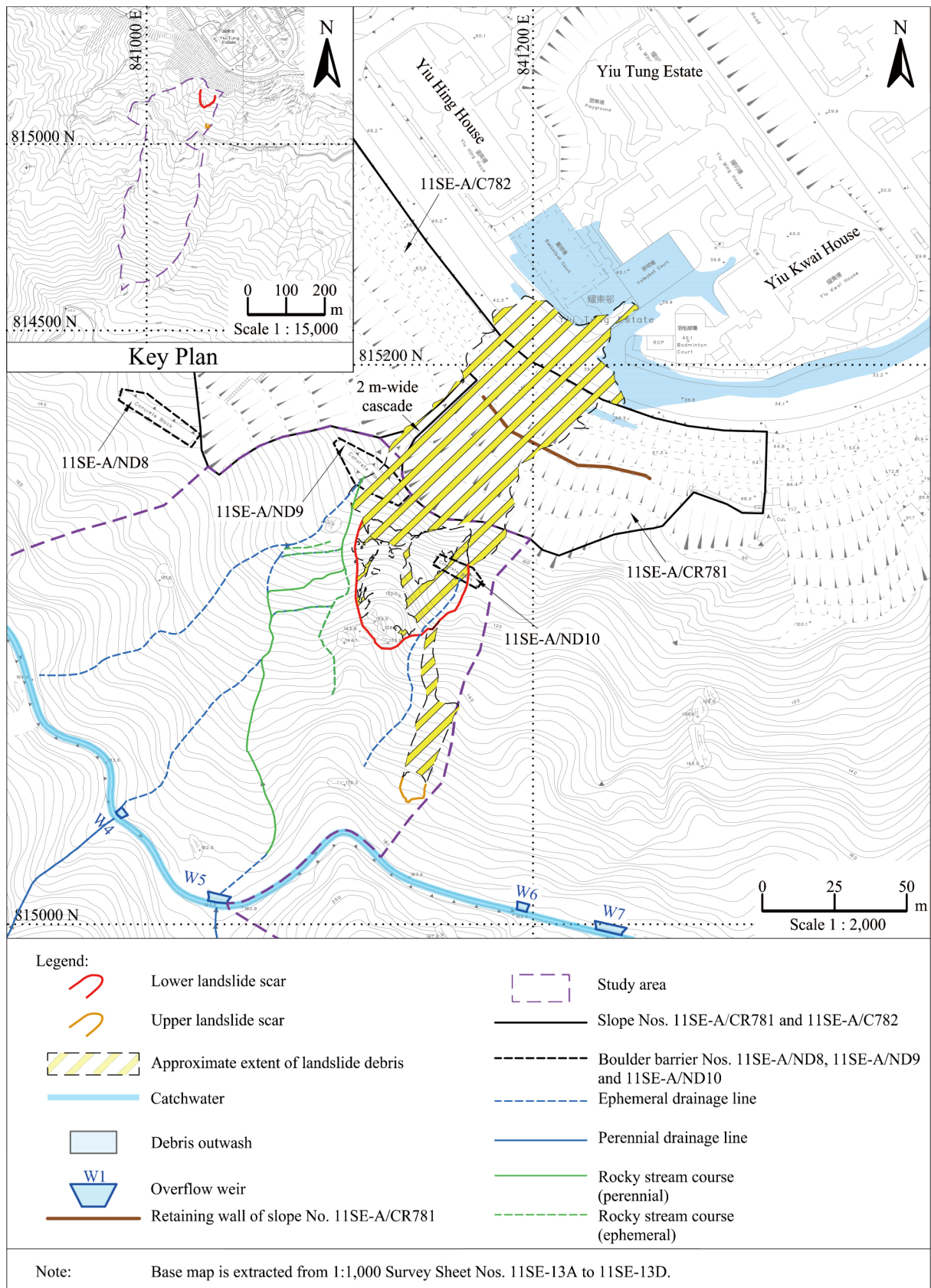
Figure 2.1   Site Layout Plan

Gabion wall ND8 is about 30 m long and has a maximum height of 5 m. Gabion wall ND9 is also about 30 m long, with a maximum height of 6 m, while gabion wall ND10 is about 20 m long and has a maximum height of 7 m. These walls are located above the cut slopes, and were built between 1980s to 1990s to arrest boulders of sizes up to 3 m and 4 m equivalent diameters at topographic depressions, the rocky stream course, and below colluvial boulder fields. Details of the boulder fall and rockfall hazards will be discussed in Section 3.3.4.

The Mount Parker Lower Catchwater is an approximately 3.6 km-long catchwater channel that runs along the hillside of Mount Parker, extending from Mount Parker in the north to the Tai Tam Tuk Reservoir in the south. The catchwater collects surface runoff from catchments above it, either through direct runoff or by intercepting natural stream courses. A small intake dam is positioned at the interception point of a major stream course at Mount Parker to regulate the water flow into the catchwater. Overflow weirs are placed along the catchwater, and the size of the catchwater channel varies.

The study area encompasses the rocky stream course, which is connected to several perennial and ephemeral drainage lines. Surface runoff from the catchments above the catchwater flows along drainage lines and is intercepted by the catchwater channel. A section of the catchwater channel, measuring 1.4 m wide and 1 m deep, truncates these drainage lines at approximately +180 mPD and diverts surface runoff eastward (Figure 1.1). Additionally, overflow weirs W4 and W5 are located above the landslide site to manage excessive surface water by diverting it into the rocky stream course as channel runoff, particularly on the western flank of the lower landslide scar (hereafter referred to as 'the western flank') (Figures 2.1 and 2.2). The channel runoff is then intercepted by three 675 mm-diameter drainage outlet pipes located underneath gabion wall ND9. Finally, the water drains to the stormwater drainage system beneath Yiu Tung Estate through a 2 m-wide cascade between the cut slopes.

Two high-rise public rental housing blocks, Yiu Hing House and Yiu Kwai House, are located about 25 m and 40 m away from the cut slopes at the bottom of the study area, respectively. Several facilities exist between these housing blocks and the cut slopes, including Yiu Hing Road, a refuse collection point, basketball and volleyball courts, as well as their steel perimeter fences. Additionally, there are metered parking spaces and a bus stop along Yiu Hing Road at the toe of the cut slopes.

2.2 Maintenance Responsibility

According to the Slope Maintenance Responsibility Information System of the Lands Department, the maintenance responsibility of gabion walls ND8, ND9 and ND10 lies with the owner of Lot No. SIL 852, which is the Hong Kong Housing Authority (HKHA).

Slope No. 11SE-A/CR781 is situated on Government Land, and the maintenance responsibility rests with the Highways Department (HyD).

Slope No. 11SE-A/C782 is divided into two sub-divisions. The maintenance of sub-division No. 1 is the responsibility of the owner of Lot No. SIL 831 (the owners of Tung Chun Court), while the maintenance of sub-division No. 2 falls under the responsibility of the HyD (Figure 2.3).

Flow direction along catchwater

Excessive surface water overflowed into the rocky stream course

a) Overflow Weir W4

Flow direction along catchwater

Excessive surface water overflowed into the rocky stream course
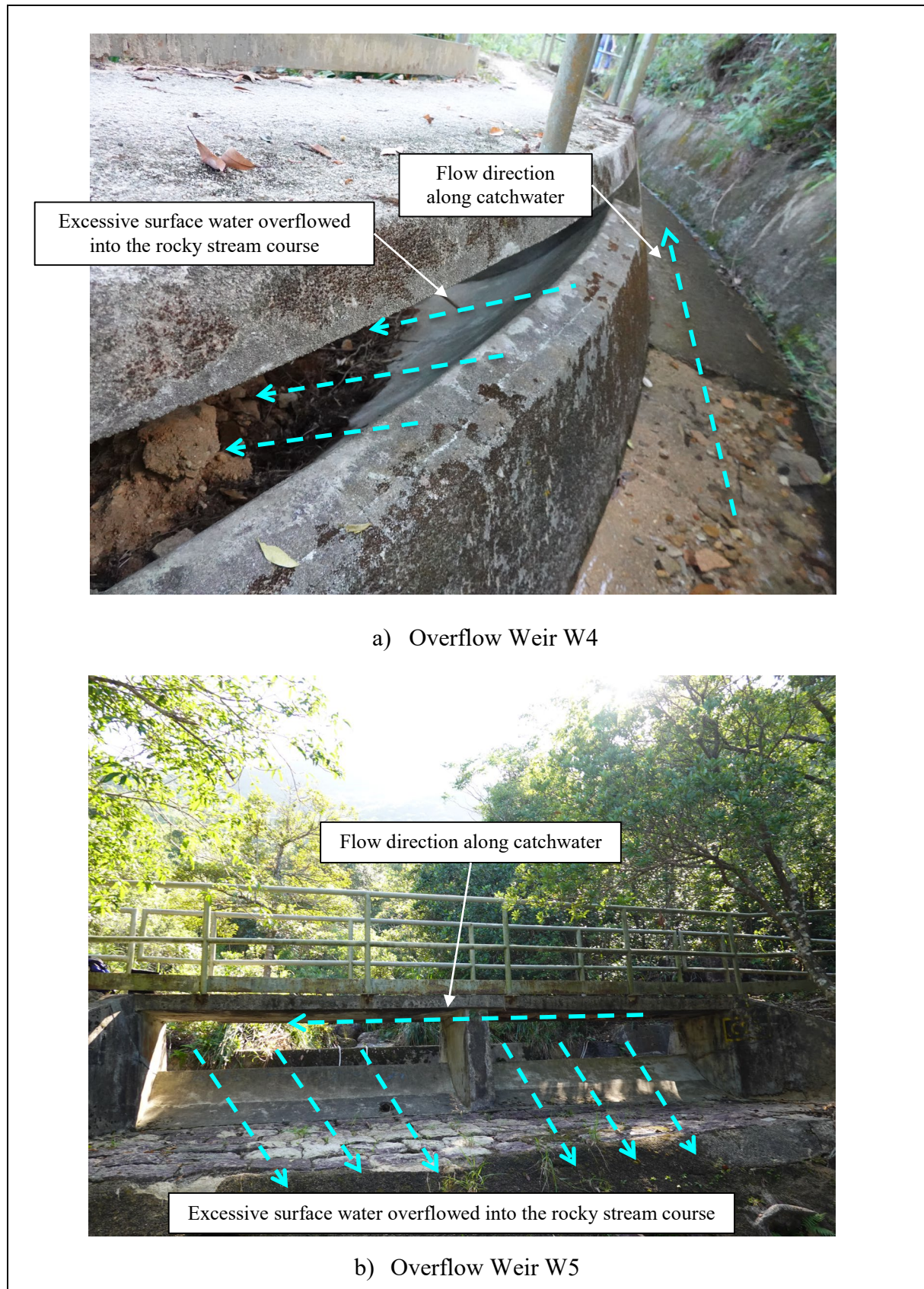
b) Overflow Weir W5

Figure 2.2   Overview of Overflow Weirs W4 and W5 above the Landslide Site (Photographs taken on 26 October 2023)
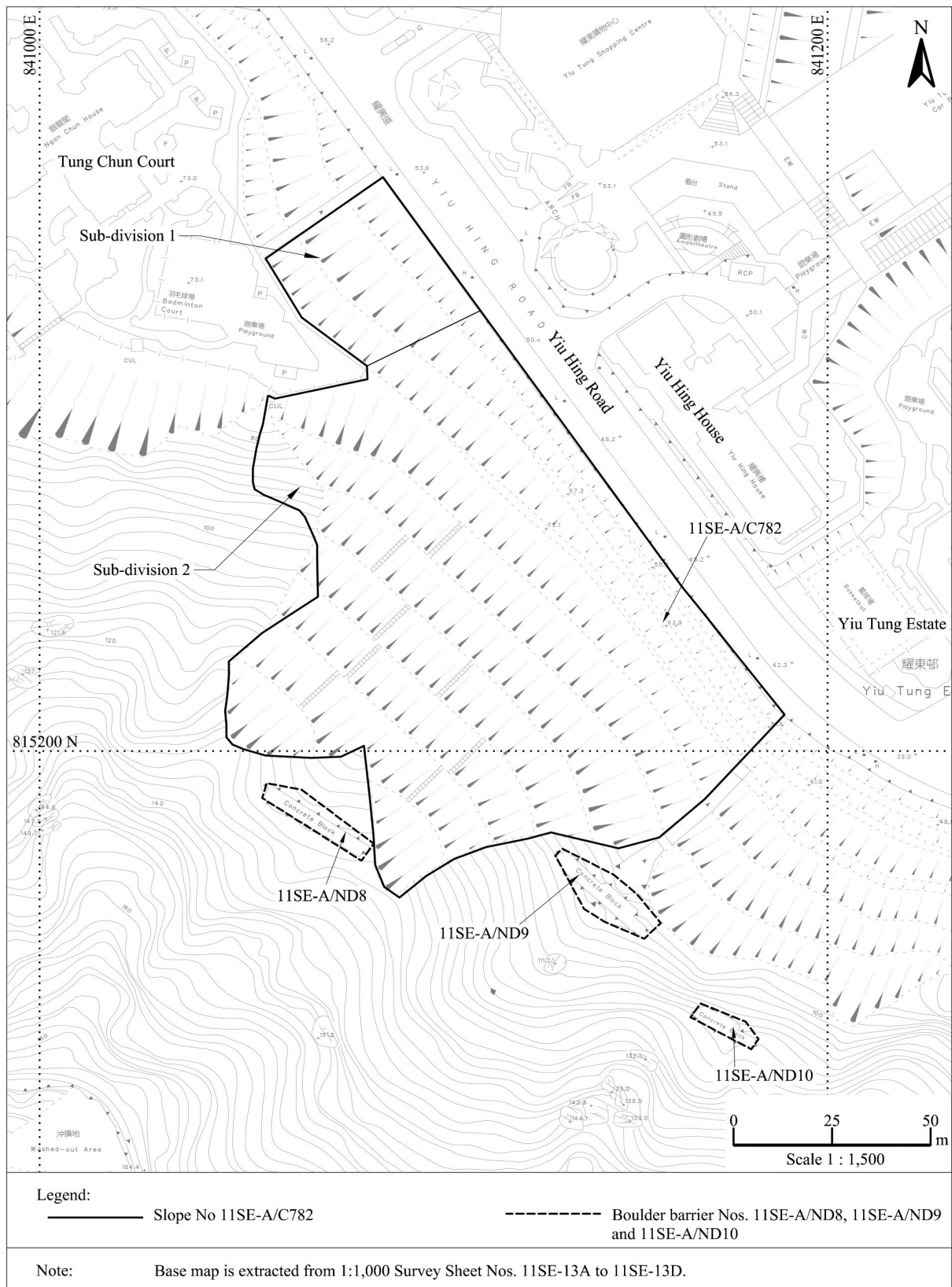
Figure 2.3   Maintenance Responsibility of Slope No. 11SE-A/C782

3 Site History, Past Slope Instability and Relevant Records

3.1 Site History

The site history has been determined from an interpretation of the available aerial photographs, a review of the relevant documentary information, and site observations. Appendix A and Figure A1 summarise detailed observations from the API, with the salient observations as follows:

The earliest available aerial photographs taken in 1945 indicate that the hillside below and up to the toe of the landslide site was significantly disturbed by anthropogenic activities, including artisanal mining, quarrying, and agriculture. The toe of the landslide site marked the upper extent of excavations and terraces associated with these activities. Larger-scale excavations are visible within the eastern side of the valley below, to the northeast of the landslide site, on the upper ridgeline, and to the southwest of the landslide site, where the scars of excavations are still evident. Additionally, there are indications of small-scale excavations within and near the landslide site, possibly associated with localised stone quarrying or artisanal mining of quartz veins.

Before 1945, a catchwater channel and an access road were built above the landslide site. While the construction of the catchwater might have involved some fill placed on the slopes below, there are no clear evidence of significant fill or signs of disturbance below the catchwater at the site. A distinct cut slope is visible at the toe of the landslide site, with agricultural terraces in 1945. There are small excavations along the eastern flank of the lower landslide scar and evidence of fresh excavations and localised erosion of existing excavations.

The 1963 aerial photographs show that natural and anthropogenic features in and around the landslide site. Tors and exhumed corestones are visible on the upper part and above the crest of the lower landslide scar and above the crest. These features are consistently matched with tors that either failed or remained at the crest of the lower landslide scar. There are bright-tone scars and a pile of stones in the rocky stream course along the western flank, suggesting minor excavations within the rock exposures. Additionally, a bright-tone scar extends along the depression to the eastern flank of the lower landslide scar, indicating additional minor excavations carried out between 1949 and 1963. Below the landslide site, huts were erected throughout the valley and along the east valley side as part of a substantial squatter development at that time. Agricultural terraces also extended up to and near the landslide site.

Between 1969 and 1972, there was a noticeable increase in human activities at the site. In the 1969 aerial photographs, a squatter hut was present on a pre-existing flat platform just below the toe of the lower landslide scar. By 1972, the number and extent of squatter huts on the gentle terrain below the lower landslide scar had significantly increased. Agricultural activities were also present on the flat ground at the western flank.

The 1989 aerial photographs mark the beginning of significant changes to the landslide site. They indicate the early stages of site formation works for the construction of Yiu Tung Estate below and adjacent to the landslide scars. Slopes were being cut, and gabion walls ND8, ND9, and ND10 were constructed. By 1991, the cut slopes, together with the culvert outlet and cascade below, were all constructed. Since the early 1990s, there have been no obvious significant changes to the landslide site.

3.2   Past Slope Instabilities

3.2.1   Enhanced Natural Terrain Landslide Inventory

The Enhanced Natural Terrain Landslide Inventory (ENTLI) recorded 15 relict landslides and one recent landslide in the study area (Figure 3.1). All ENTLI features in the study area are less than 22 m wide at their widest points.

ENTLI Nos. 11SEA0264E and 11SEA0265E are identified as broad depressions on the west side of the spurline directly above the lower landslide scar. The recent landslide (ENTLI No. 11SEA0277E) is an open hillslope failure first observed in 1963. It is situated above the catchwater and has a maximum source width of 10 m and a length of 12 m.

3.2.2   Large Landslide Database

The GEO's Large Landslide Database (Scott Wilson, 1999) shows that there are no large landslides within or in the vicinity of the study area (Figure 3.1).

3.2.3   Reported Landslide Incidents

According to the GEO's landslide database, two reported landslide incidents occurred to the east of the study area (Figure 3.1).

Incident No. HK87/5/5 involved a small soil slope failure behind squatter huts. This incident had an estimated failure volume of about 2 m^3 and occurred prior to the development of Yiu Tung Estate. The incident report suggested that the failure was possibly induced by infiltration.

Incident No. 2006/07/0681 was a rockslide on the natural slope above slope No. 11SE-A/CR781. This incident had an estimated failure volume of about 5 m^3. The incident report suggested that the failure was possibly caused by infiltration and the presence of adversely orientated joints.

There are no reported landslide incidents within the study area.

3.2.4   Landslides from Aerial Photograph Interpretation

The detailed API has identified three additional relict landslides in the study area that were not previously recorded in the ENTLI (Figure 3.1) (Section 3.2.1). Two of these landslides are located above the catchwater and are characterised by convex change-in-slopes with nearby drainage lines. The remaining landslide is situated close to the upper landslide scar, which is also characterised by a convex change-in-slope.
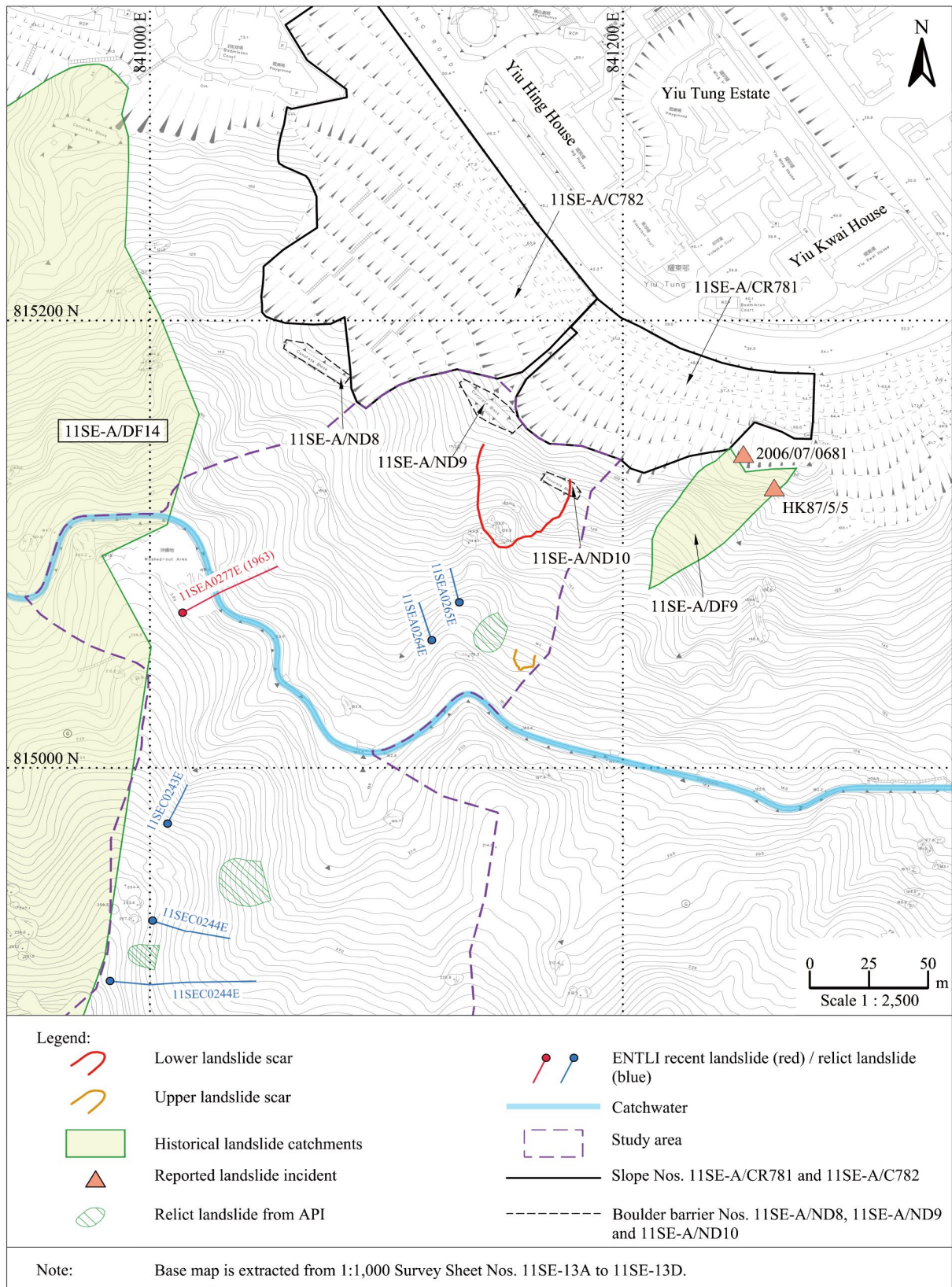
Figure 3.1   Past Slope Instabilities

3.2.5 Historical Landslide Catchments

Two Historical Landslide Catchments (HLCs) have been identified nearby. These include HLC Nos. 11SE-B/DF9 and 11SE-A/DF14, located to the east and west of the study area, respectively (Figure 3.1).

3.3 Previous Studies, Assessment and Inspections

3.3.1 SIFT and SIRST Studies

In February 1998, the cut slopes were identified under the GEO's project entitled 'Systematic Inspection of Features in the Territory' (SIFT) and categorised as a Class 'C2' feature, i.e. cut feature 'considered to meet the GEO criteria for slope registration' and 'have been formed or substantially modified after 30 June 1978'.

In May 1998, the cut slopes were inspected under the GEO's project entitled 'Systematic Identification and Registration of Slopes in the Territory' (SIRST). The SIRST field sheet stated that about 70% of slope No. 11SE-A/CR781 was covered by hard surface, while about 50% of slope No. 11SE-A/C782 was bare. No signs of seepage were observed on the cut slopes.

3.3.2 Catchwater Study

In 1979, the Water Supplies Department (WSD) and the Geotechnical Control Office (GCO, renamed GEO in 1991) conducted a study to investigate the stability of catchwaters and their associated slopes (GCO, 1980). The objective was to make recommendations to reduce the potential risks to downhill development.

Data for 48 catchwaters were collected, and after screening, walkover surveys of 19 catchwaters were carried out. API and mapping were conducted on six selected catchwaters, including the Mount Parker Lower Catchwater, which was found to have high potential risks of consequence failure.

The study concluded that the few cut slope failures were relatively small, and the overall condition of the catchwater appeared good (Phillipson et al, 1982). At the time of inspection, the general condition of the slopes along the catchwater appeared to be good, and the blockage risk was low for most of the catchwater. The study also identified that some areas, including the present-day Yiu Hing Estate, could potentially be at risk from a catchwater breach or blockage (Figure 3.2).

As part of the follow-up actions, the WSD conducted flooding studies of selected catchwaters, including Shing Mun Catchwater, Tai Lam Chung Catchwater and Beacon Hill Catchwater. However, the Mount Parker Lower Catchwater was excluded from this study. Several slopes along these catchwaters were nominated for action under the GEO's Landslip Preventive Maintenance (LPM) Programme (Martin, 2009). The LPM works on these slopes included soil nailing, repair of the slope surface covers, and provision of new drainage measures.

| Note: | Drawing is extracted from GCO Drawing No. GCE183. |

CONSEQUENCES

DOWNSLOPE AFFECTED AREA (DAA) IN THE EVENT OF CATCHWATER BREACH OR BLOCKAGE

PRINCIPAL INHABITED AREAS POTENTIALLY AT RISK FROM CATCHWATER BREACH OR BLOCKAGE

Approximate location of Yiu Tung Estate

Approximate location of the 8 September 2023 incident
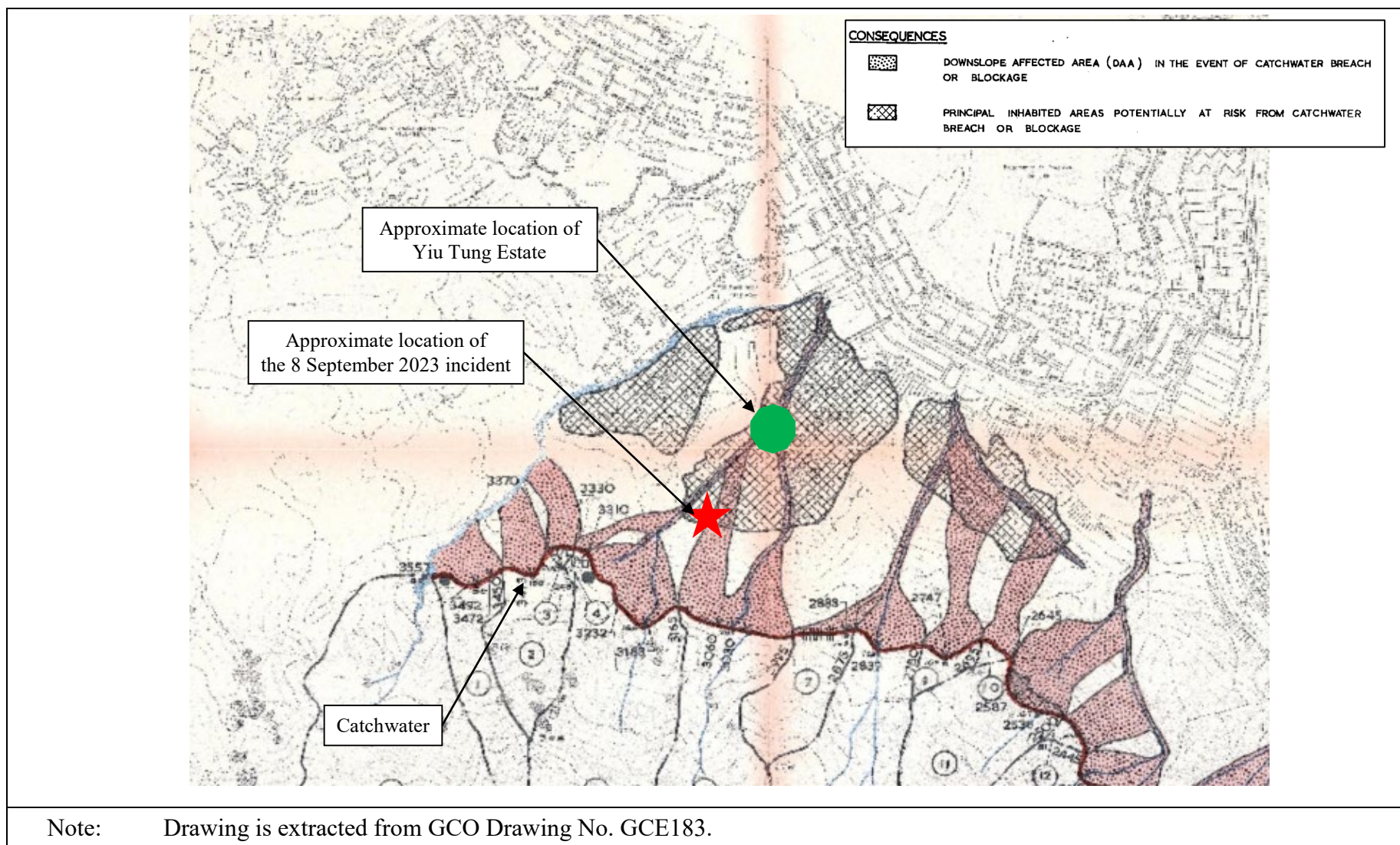
Catchwater

Figure 3.2   Catchwater Study in Mount Parker

3.3.3 Geotechnical Area Study

The study area where the landslides occurred was studied in the early 1980s as part of the territory-wide Geotechnical Area Study (GAS). This study aimed to provide a geotechnical basis for land use management and planning. The findings of the study are summarised in GAS Report No. 6 (GCO, 1981), which are based on API, field reconnaissance, and assessment of existing ground investigation records.

The study revealed that the study area mainly consisted of granitic terrain with bouldery colluvium in the drainage lines. It identified large perched boulders, in-situ corestones, and tors in the area. Sheeting joints were found in major areas of the exposed rock along the rocky stream course. Geological surveys at the lower end of the study area indicated apparent break-in-slope at the upper limit of squatter development, which were identified as old quarry faces (Figure 3.3a).

3.3.4 Studies of Shau Kei Wan East Public Housing Development

In the late 1980s, squatter settlements were cleared, and site formation works for the Shau Kei Wan East public housing development began. This development concluded with the completion of Yiu Tung Estate in the early 1990s. Before the site formation works, prominent corestones and tors were visible in the upper area of the lower landslide scar. During this process, a series of cut slopes, retaining walls and gabion walls, including slope Nos. 11SE-A/CR781 and 11SE-A/C782 and gabion walls ND8, ND9, and ND10, were formed above Yiu Hing Road (Figures 3.3b and 3.4).

Subsequent geotechnical studies were conducted as part of the proposed Shau Kei Wan East public housing development to redevelop the squatter settlements. The studies included desk study, visual inspections, site-specific ground investigation with groundwater monitoring, laboratory testing, geological surveys, boulder surveys, discontinuity surveys, and stability assessment.

The soil cut portions of the cut slopes were proposed to be trimmed at a gradient of 1(v) on 1.5(h) with 1.5 m-wide berms at a vertical interval of 7.5 m, while the rock cut portions of the cut slopes were proposed to be cut at a gradient of 3(v) on 1(h). It was proposed to install raking drains at 3 m centre-to-centre horizontal spacing and at about 1 m above every berm of the soil cut portions. Counterfort drains were also provided at locations where heavy seepage was encountered. With these measures, the groundwater table was expected to be effectively kept close to the bedrock. The stability assessment was based on the site-specific shear strength parameters of decomposed granite, and assumed design groundwater tables of 1 m and 3 m above the bedrock, corresponding to rainfall with a 10-year return period and the anticipated worst groundwater condition, respectively. The assessment showed that the cut slopes had adequate factors of safety against failures under the design scenarios.

Retaining walls were proposed in areas with limited space for forming cut and fill slopes. Three primary types of retaining walls were considered, including cantilever reinforced concrete retaining walls, counterfort reinforced concrete retaining walls, and mass concrete retaining walls. The section of slope No. 11SE-A/CR781 included one of the cantilever reinforced concrete retaining walls constructed as part of the development. Behind this

Localised excavations observed in API

Tors

Catchwater

Rocky stream course

Upper limit of main excavation characterised by a number of abandoned quarry faces

Cluster of exhumed corestones and tors which failed on 8 September 2023

Squatter development

a) Overview of the Hillside before Site Formation Works in the Mid-1980s

Retaining wall and soil portions above rock cut slope

Gabion wall ND9 and cascade constructed

Slope No. 11SE-A/C782

Slope No. 11SE-A/CR781

Three 675 mm-diameter drainage outlet pipes beneath gabion wall ND9

b) Overview of Site Formation Works in 1991

Figure 3.3   General View of the Landslide Site before and during Site Formation Works
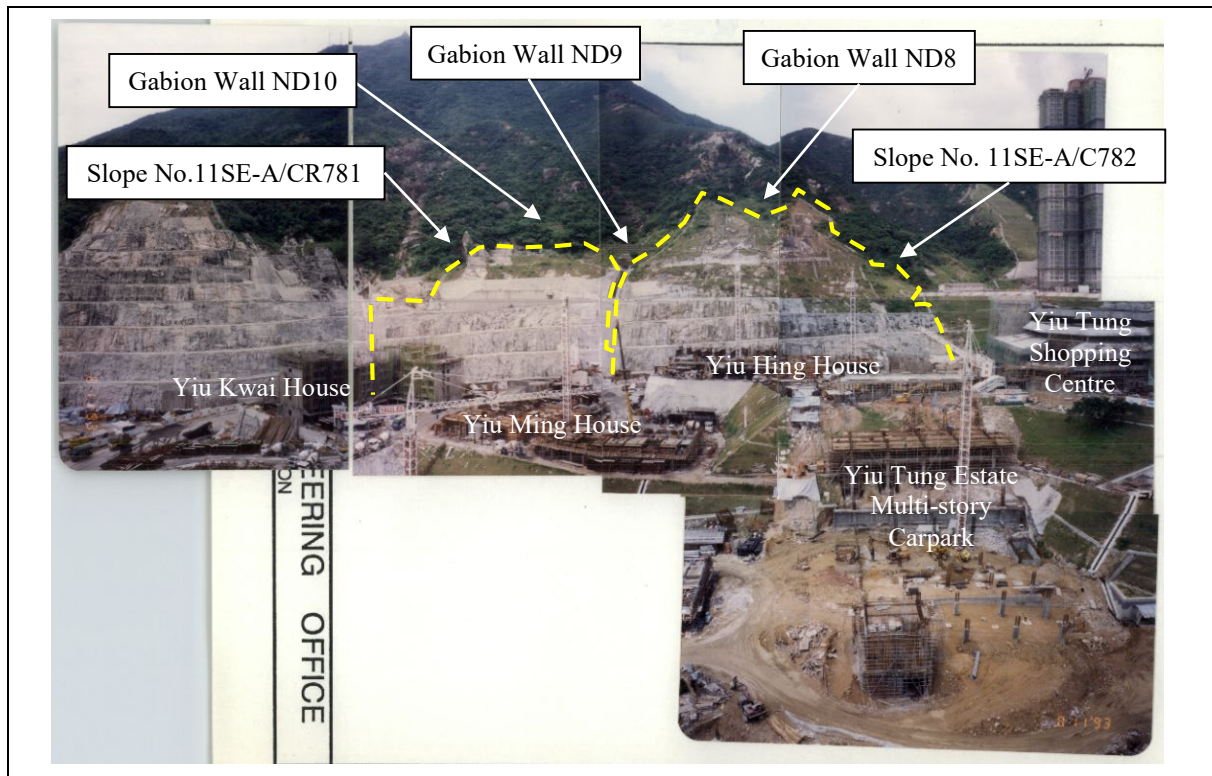
Figure 3.4 General View of the Cut Slopes and Gabion Walls during Site Formation Works (Photographs taken on 11 August 1993)

retaining wall, rockfill was backfilled at a gradient of 1:1.3 and was covered by a stone-pitching cover. Weepholes were incorporated into the retaining wall to facilitate drainage.

Discontinuity surveys were carried out on the exposed rock cut surface during the site formation works. Two sets of dominant sub-vertical joints dipping at 69°/270° to 89°/303° and a shallow dipping sheeting joint dipping at 17°/097° to 21°/001° were identified with potential toppling instability. Major global instability was unlikely to occur in the rock cuts. These observations were consistent with the potential failure modes identified in kinematic stability analyses, such as minor toppling failure.

For the rock cut portions of the cut slopes, in-situ rock slope stabilisation works such as mass concrete buttresses, rock dowels and rock bolts had been provided for potentially unstable rock blocks identified on site. For the areas where rocks were closely jointed, loosen, or weakened due to blasting and weathering, reinforced sprayed concrete or no-fines concrete covered by stone pitching with weepholes were provided.

As part of the geotechnical studies for the proposed housing development, the boulder surveys identified four types of boulders in the study area and the adjoining areas (Figure 3.5). They are:

(a) Corestones – Generally found on the spurs and within the saprolite. They are formed by weathering along sub-vertical and sub-horizontal joints,

(b) Tors – Formed by further erosion/weathering of corestones where the saprolite has been eroded,

(c) Transported boulders – Found in the vicinity of corestones/tors and along the rocky stream course, and

(d) Quarry waste – Several small, abandoned quarries were found in the lower area of the study area. Several angular boulders of size up to 2 m were found near these quarries.

Note: Key information of boulder assessment is based on HD Drawing No. CEP-SKWE-GS6.
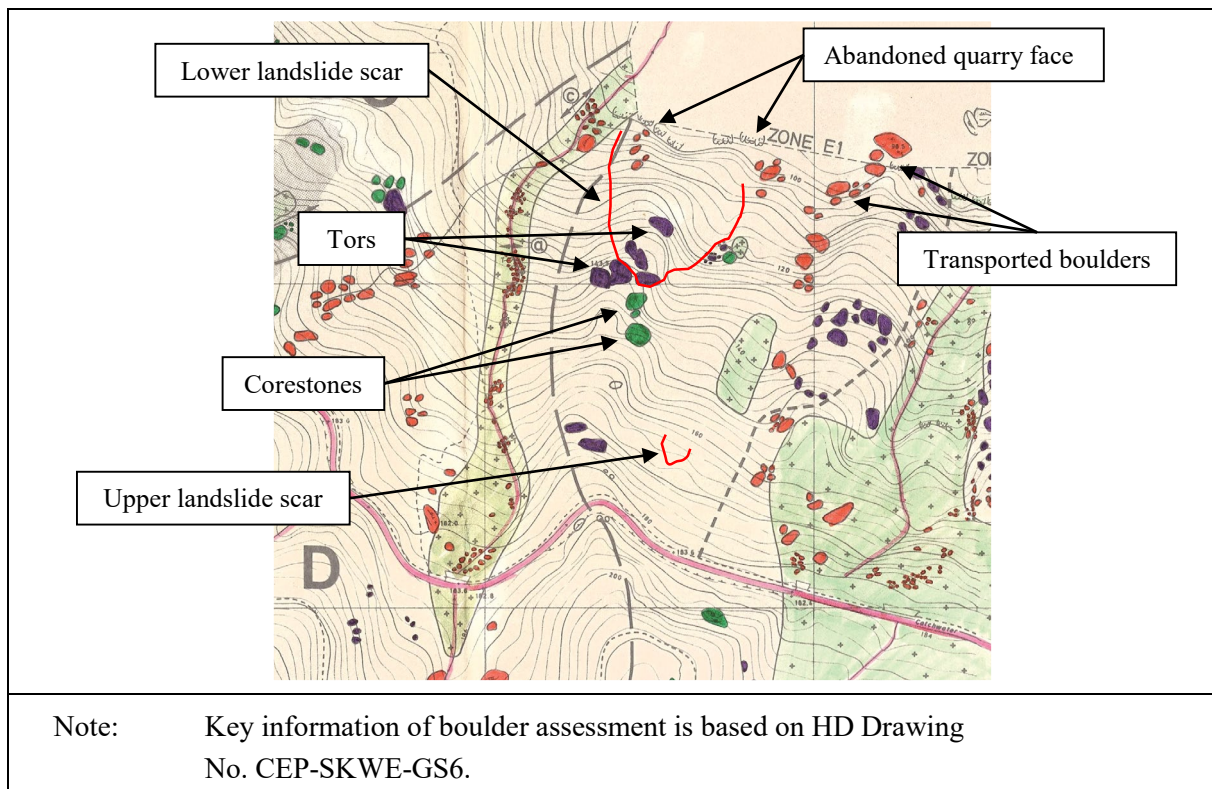
Figure 3.5 Boulder Assessment of Hillside above the Landslide Site

Based on the surveys, the studies identified numerous boulder fall and rockfall hazards from colluvial boulder fields with partially to fully exhumed corestones and tors. These hazards were identified, mapped, and mitigated in subsequent phases of works. To mitigate these hazards, the following works were carried out as part of the site formation works and boulder treatment measures:

(a) Removal and partial removal of hazardous boulders, corestones, tors or rock outcrops,

(b) In-situ stabilisation, including dentition and buttresses, and

(c) Gabion walls designed to withstand boulder fall or rockfall hazards up to 3 m and 4 m equivalent diameters at topographic

depression, drainage line outlets and below colluvial boulder fields. A total of ten gabion walls were constructed across the hillside above the development site, including three that were constructed on the western and eastern flanks of the landslide site, namely gabion walls ND8, ND9, and N10 (Figures 3.6 and 3.7).

The Civil Engineering Section of the Housing Department (HD) prepared the First, Second, and Third Geotechnical Design Reports for Shau Kei Wan East Public Housing Development, which provided design information on the cut slopes and gabion walls (HD, 1986a; 1986b; 1987). The GCO checked these reports and had no adverse comments.

As-built records of removal or in-situ stabilisation works could not be found in the GEO file records. However, previous boulder stabilisation measures were observed during site inspections and mapping after the landslide. These observations are discussed in further details in Section 6.

3.3.5 LPMit Stage 2 Study

In 2011, the GEO included the private portion (sub-division No. 1) of slope No. 11SE-A/C782 in the Landslip Prevention and Mitigation (LPMit) Programme for a safety screening study (known as Stage 2 Study). GEO's consultants, Fugro, undertook the study. The objective of the Stage 2 Study is to establish if there is prima facie evidence that warrants the issue of a Dangerous Hillside Order under the Buildings Ordinance to require the implementation of a detailed investigation and the necessary slope upgrading works, or the issue of an Advisory Letter to require the implementation of slope repair or maintenance works.

Fugro reviewed the relevant files maintained by the GEO and HD and found that the GCO had checked the design of sub-division No. 1 of the slope as part of the site formation submissions for the development of Shau Kei Wan East in 1988. Fugro also found that sub-division No. 1 of the slope was constructed to its current configuration between 1989 and 1994 as part of the site formation works for this development.

In March 2011, Fugro carried out a visual inspection of the slope and found it to be in fair condition, with no signs of distress, seepage or evidence of instability observed during the inspection. It was concluded that issuing an Advisory Letter to the lot owner of Lot No. SIL 831 (i.e. owners of sub-division 1 of the slope) was warranted (Fugro, 2011).

On 9 January 2012, the GEO issued the Advisory Letter to the respective owners of sub-division No. 1 of the slope.

Slope No. 11SE-A/C782
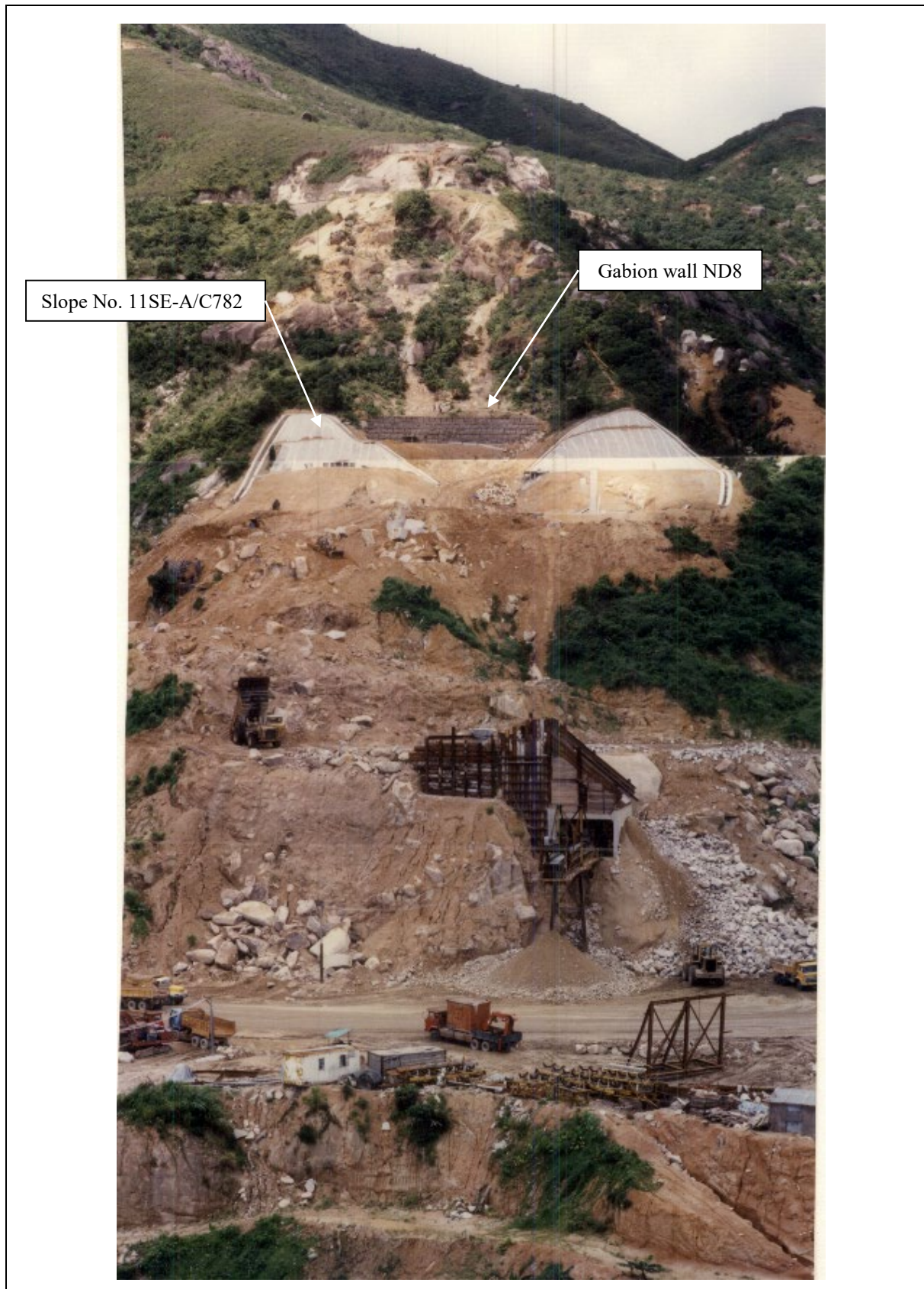
Gabion wall ND8

Figure 3.6   General View of Gabion Wall ND8 during Site Formation Works

a) Overview of Gabion Wall ND9 Across the Rocky Stream Course

Gabion wall ND10

Three 675 mm-diameter drainage outlet pipes beneath gabion wall ND9 under construction
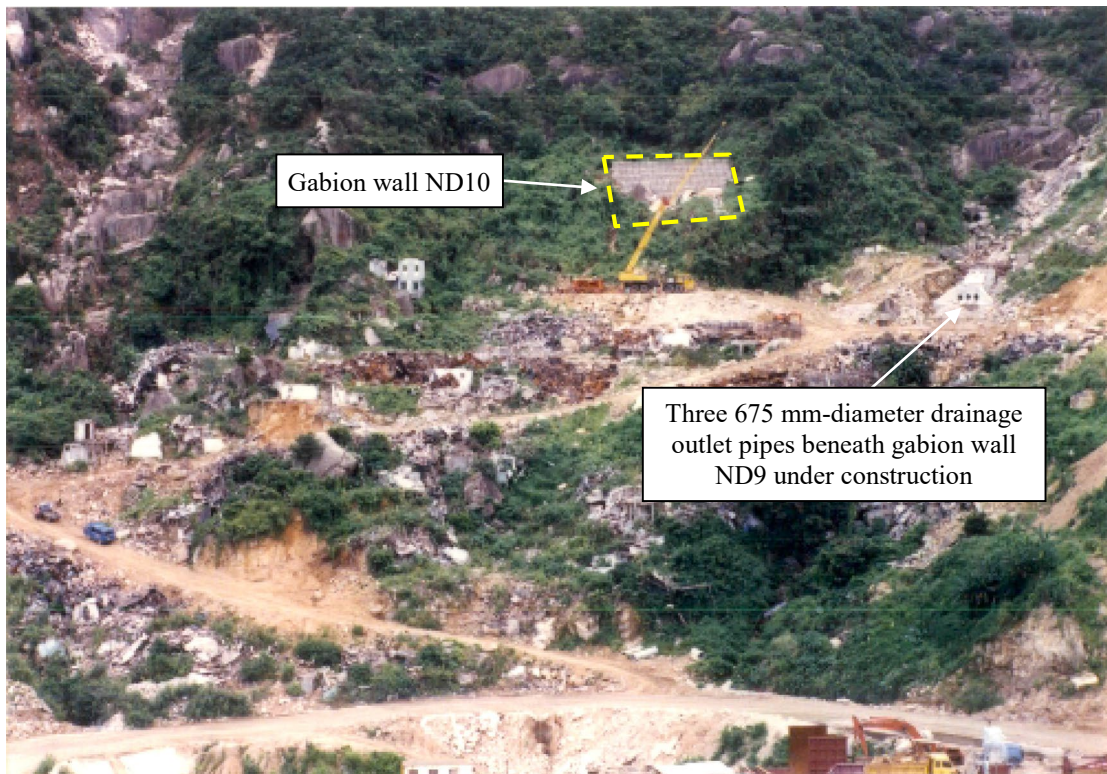
b) Overview of Gabion Wall ND10

Figure 3.7 General View of Gabion Walls ND9 and ND10 during Site Formation Works

3.3.6 LPMit Stage 3 Study

In 2009, the GEO included the government portion (sub-division No. 2) of slope No. 11SE-A/C782 in the LPMit Programme for a detailed study (known as Stage 3 Study). The Stage 3 Study was undertaken by the GEO's consultants, Fugro. The study involved a site-specific ground investigation, laboratory testing, detailed topographic survey, stability assessment, and design of necessary upgrading works (Fugro, 2013a).

Fugro collected geological and discontinuity data from the rock joint mapping of the exposed rock cut face and surface stripping of the existing hard surface cover during the site-specific ground investigation. Fugro observed several localised rock joints with potential sliding and toppling instability at the lower slope batter. These observations were consistent with the potential failure modes identified in kinematic stability analyses, such as minor sliding and toppling failures.

Given that the soil and rock slope portions did not meet the required geotechnical safety standards, upgrading works were proposed, including scaling, construction of concrete buttresses, installing rock dowels, and provision of wire mesh for the in-situ rock slope stabilisation at the lower rock slope batter. For the soil cut portions in the upper slope batter, the proposed stabilisation measures involved installing soil nails along with prescriptive raking drains.

The LPMit works commenced in October 2011 and were completed in June 2013 (Fugro, 2013b). In-situ rock slope stabilisation works had been provided for potentially unstable rock blocks identified on site. Soil nails and raking drains were installed in the upper slope batter, and wire mesh protection was provided on the exposed rock face at the lower slope batter.

3.3.7 Maintenance Inspections

The HyD conducted Engineer Inspections (EIs) on slope No. 11SE-A/CR781 in March 2021 and slope No. 11SE-A/C782 in November 2018. The EI records indicated the hard surface cover was in fair condition, with partially blocked drainage channels. While no signs of distress were found on the cut slopes, seepage was noted on slope No. 11SE-A/CR781 during the inspections. The Routine Maintenance Inspections (RMIs) were conducted on slope No. 11SE-A/CR781 in February 2023 and slope No. 11SE-A/C782 in May 2023. These inspections identified the need for maintenance, including clearing drainage channels, unblocking weepholes and outlet pipes, and removing surface debris and vegetation. All recommended maintenance works were subsequently completed.

The HD conducted EIs on gabion walls ND8 and ND9 in January 2021, and gabion wall ND10 in January 2022 (Figure 3.8). During these inspections, no signs of distress, seepage, or blockage of three 675 mm-diameter drainage outlet pipes underneath gabion wall ND9 were noted. The RMIs for gabion walls ND8 and ND9 were conducted in January 2022 (Figures 3.9 and 3.10), while gabion wall ND10 was inspected in January 2021. The maintenance recommendations included repairing hard surface cover and removing surface debris and vegetation, all of which were completed.

Figure 3.8   General View of Gabion Wall ND10 before the Incident (Photograph taken on 10 January 2022)

Figure 3.9   General View of Gabion Wall ND8 before the Incident (Photograph taken on 10 January 2022)

Figure 3.10 General View of Gabion Wall ND9 before the Incident (Photograph taken on 10 January 2022)

There is no evidence showing the blockage of these drainage outlet pipes before the 8 September 2023 incident.

3.4 Previous Ground Investigation

Between 1984 and 2010, several contractors conducted ground investigations in the area surrounding the landslide site on behalf of the HD, CEDD, and Drainage Services Department (Figure 3.11). These investigations aimed to assess geological and groundwater conditions and gather soil samples for laboratory testing. Table 3.1 summarises the previous ground investigations conducted within the study area and the cut slopes.

Intrafor Hong Kong Limited (Intrafor) conducted the site-specific ground investigation for slope No. 11SW-A/C782 under the LPMit Programme from November 2009 to January 2010 (Intrafor, 2010).

Drillhole No. C782-DH1, located at the crest of slope No. 11SW-A/C782, encountered a thin layer of fill up to 0.5 m thick. This layer consists of yellowish-brown spotted dark greenish-grey and white, clayey, silty fine to coarse SAND with some angular to subangular fine grave-sized quartz fragments and some fine to medium gravel-sized fragments. Beneath the fill layer, there was an 8.1 m-thick layer of completely decomposed medium- to fine-grained granite (CDG) overlying the bedrock of moderately decomposed to slightly decomposed medium- to fine-grained granite (M/SDG). CDG consists of extremely weak, yellowish-brown spotted dark greenish-grey and white, silty fine to coarse SAND with some fine gravel.
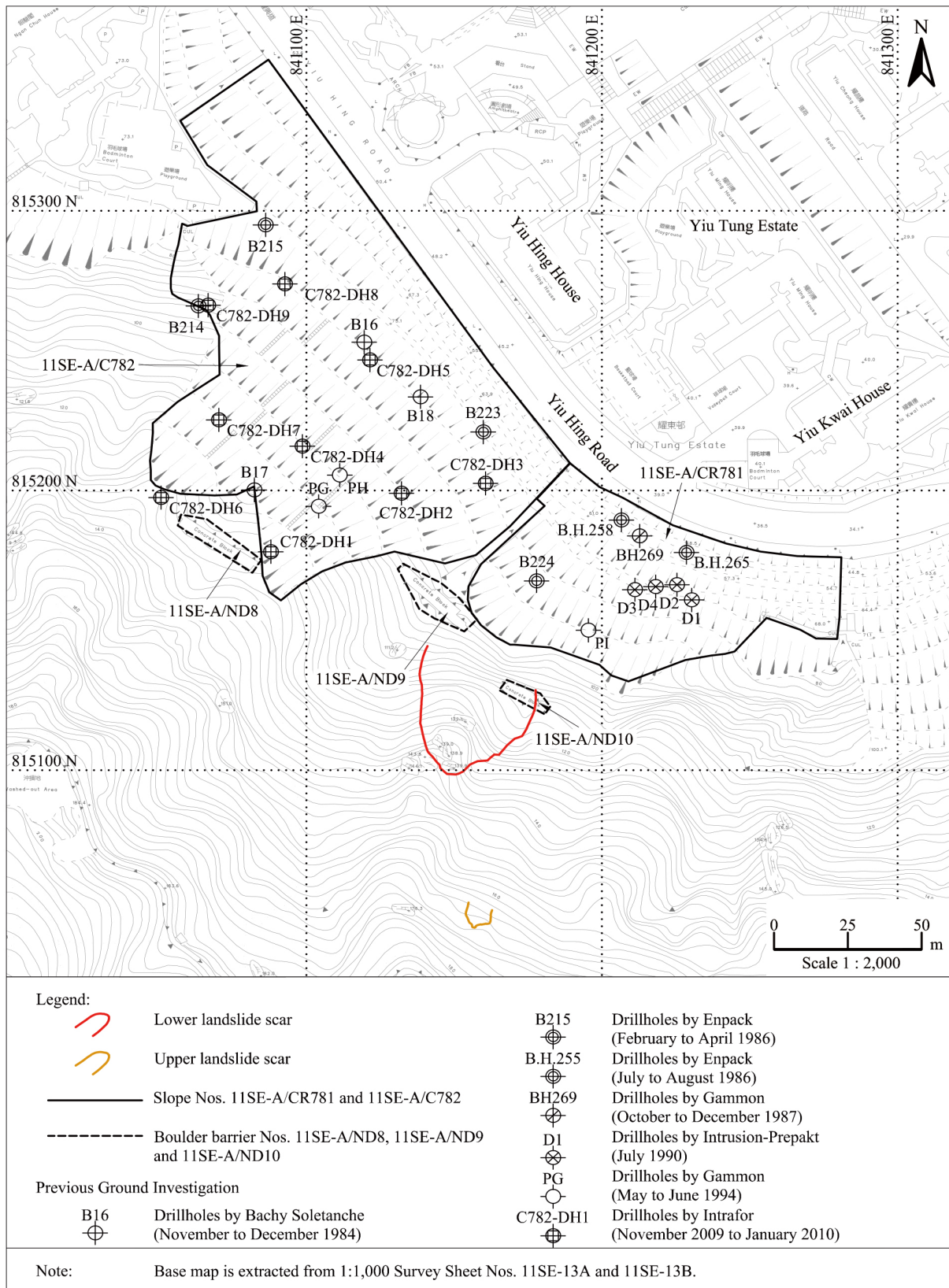
Figure 3.11 Locations of Previous Ground Investigation Stations

Table 3.1   Previous Ground Investigations within the Study Area and the Cut Slopes

Year	Contractor	Stations	Reference
1984	Bachy Soletanche Group	3 vertical drillholes	Bachy (1985)
1986	Enpack (HK) Limited	4 vertical drillholes	Enpack (1986a)
1986	Enpack (HK) Limited	2 vertical drillholes	Enpack (1986b)
1987	Gammon Construction Limited	1 vertical drillhole	Gammon (1989)
1990	Intrusion-Prepakt (Far East) Limited	4 vertical drillholes	Intrusion (1990)
1994	Gammon Construction Limited	3 vertical drillholes	Gammon (1994)
2009 - 2010	Intrafor Hong Kong Limited	9 vertical drillholes	Intrafor (2010)

Drillhole Nos. C782-DH2 and C782-DH3 at slope No. 11SW-A/C782 revealed a 4 m- to 5 m-thick layer of interbedding corestones, highly decomposed medium-grained granite (HDG), and CDG. The HDG layer comprises weak to moderately weak, yellowish-brown spotted dark greenish-grey, white and pink, silty fine to coarse SAND with some fine gravel.

The ground investigation revealed no notable adverse geological features and generally confirmed the regional geology discussed in Section 4.1.

3.5   Groundwater Conditions

Standpipes and piezometers were installed in several drillholes near the landslide site (Table 3.2). Generally, a main groundwater was found within the bedrock, occasionally reaching the corestone-rich layer of granite, HDG, and CDG. Perched groundwater tables were sometimes observed at the C/HDG layer.

Table 3.2   Summary of Groundwater Monitoring Results near the Landslide Site

Monitoring Station [1]	Monitoring Period	Ground Level (mPD)	Tip Level (mPD)	Response Zone (mPD)	Materials in Response Zone	Highest Measured Groundwater Level (mPD)
B224(P)	March to April 1986	+89.09	+78.59	+79.39 to +78.09	C/HDG	+79.94 (C/HDG)
PI(P1)	June 1994	+89.75	+82.45	+83.25 to +81.95	Corestone-rich layer of granite & CDG	+83.54 (Corestone)
PI(P2)	June 1994	+89.75	+77.85	+78.65 to +77.35	SDG	+86.95 (Fill)
C782-DH1(S)	December 2009	+123.32	+104.34	+113.42 to +104.34	M/SDG	+112.36 (Bedrock)
C782-DH1(P)	December 2009	+123.32	+114.92	+115.72 to +114.42	CDG	Dry
C782-DH2(S)	December 2009	+96.40	+88.19	+95.40 to +88.19	Corestone-rich layer of granite & CDG	+92.70 (Corestone)
C782-DH3(P)	December 2009	+80.72	+76.72	+77.52 to +76.22	Corestone-rich layer of granite, HDG, & CDG	Dry

Note: (1) (S) denotes standpipe and (P) denotes piezometer.

4 Geology and Geomorphology

4.1 Regional Geology

The Hong Kong Geological Survey 1:20,000 scale Solid and Superficial Geology Map Sheet No. 11 Edition II (GEO, 2012) indicates that the solid geology of the landslide site consists of medium-grained biotite granite of the Kowloon Granite (klk_gm) and fine-grained granite of the Mount Butler Granite (klb_gf) (Figure 4.1). The intrusive boundary between these two granites coincides with the crest of the lower landslide scar at about +138 mPD.

Within this context, the lower landslide is situated in the Kowloon Granite, while the upper landslide is located within the Mount Butler Granite. The map also shows northeast-southwest oriented photolineaments to the northwest of the landslide site. Additionally, patches of Quaternary colluvium (Qd) are shown within drainage lines and topographic depressions above the catchwater, as well as in former depressions below the landslide site prior to the development of Yiu Tung Estate.

Notably, no major geological structures have been recorded at the landslide site or nearby areas.

4.2 Hydrogeological Setting

The catchment of the study area includes both ephemeral and perennial drainage lines that converge into the rocky stream course along the western flank (Figure 4.2). According to Strahler (1964), it is classified as a low (2nd) order drainage basin, which probably experiences low to moderate water discharge during intense rainfall events.

In the upper part of the study area, the drainage lines are not well-defined or associated with obvious gully incisions. However, below an elevation of approximately +220 mPD, the drainage lines become more incised and flow in well-defined gullies. The catchwater intercepts the drainage lines at approximately +180 mPD and redirects surface runoff collected from the uphill catchments eastward under normal flow conditions. To manage excessive surface water, overflow weirs W4 and W5 serve as outlets. When the catchwater reaches its capacity, the excessive surface water drains into the rocky stream course adjacent to the lower landslide scar, together with the surface runoff from the catchment below the catchwater. This runoff is then intercepted by three 675-mm diameter drainage outlet pipes underneath gabion wall ND9. The runoff eventually drains to the stormwater drainage system beneath Yiu Tung Estate through the cascade between the cut slopes.

The rocky stream course is predominantly northeast-flowing, a pattern influenced by the geological structures and photogeological lineaments of a similar trend. Rock outcrops are presented along the stream course, both above and below the overflow weirs, extending towards gabion wall ND9. The terrain along rocky stream course is characterised by relatively wide sections with variably undulating and stepped features, largely controlled by the dominant discontinuities in different areas. Field observations on the rocky stream course will be discussed in Section 6.7.

Legend :

⌒ (red) Lower landslide scar   ⌒ (orange) Upper landslide scar

Superficial deposits   Solid geology

Qd   Silt, sand, gravel with boulders (colluvium)   Klb_gf   Fine grained granite

                                                      Klk_gm   Medium-grained biotite granite

Geological lines

—— — —— Contact (Approximate)   —— · —— · — Photogeological lineament

Note: Geological map is extracted from the 1:20,000 scale Hong Kong Geological Map Series HGM 20 (edition II), Sheet No. 11 (GEO, 2012a).

Figure 4.1   Regional Geology
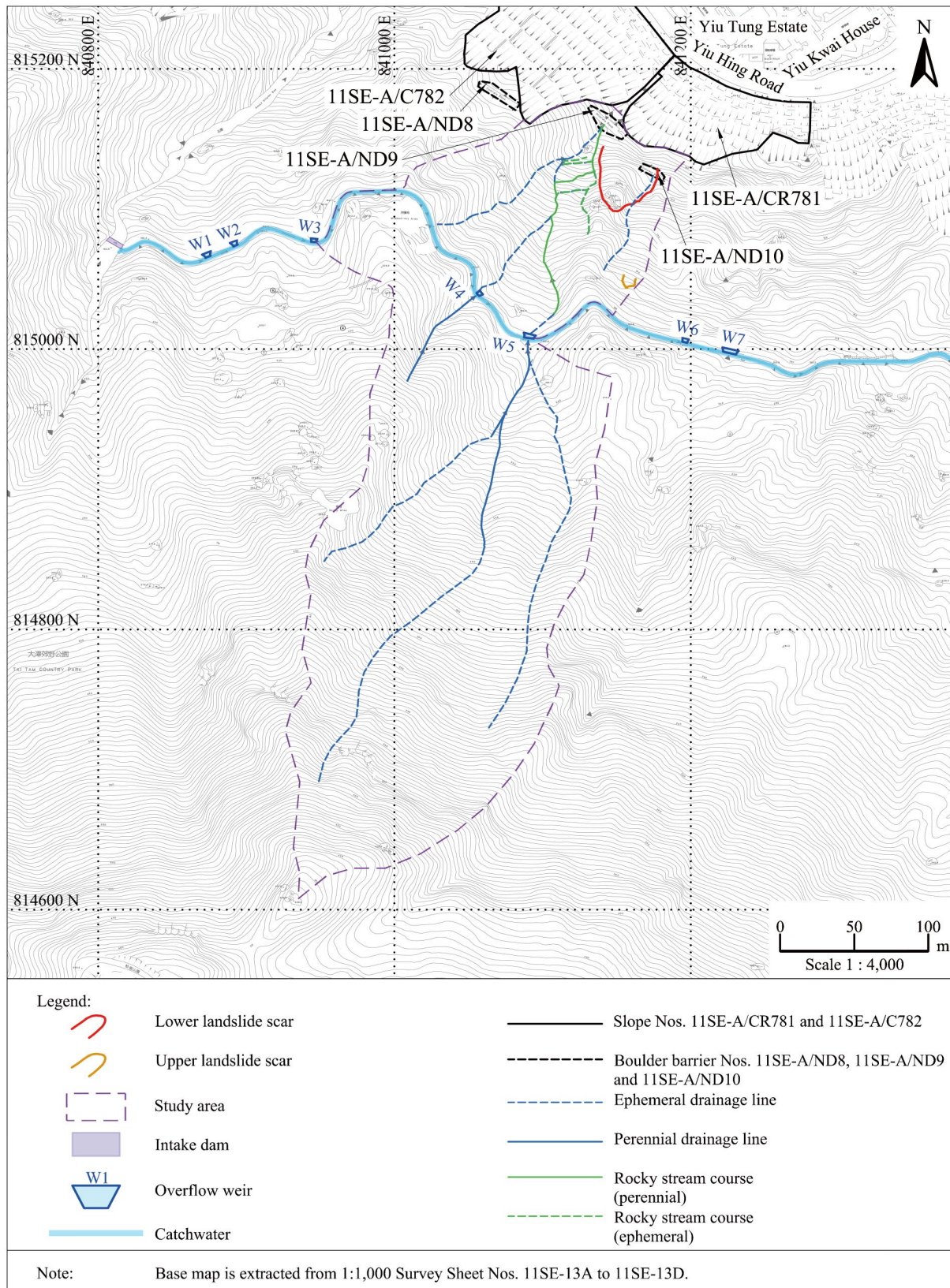
Figure 4.2   Site Hydrogeological Setting

4.3   Geomorphological Setting

The aerial photographs, particularly those taken in 1963, reveal a rocky landscape near the landslide site. The hillside is steep and characterised by a number of sub-vertical, linear rock cliffs with persistent joints striking northeast-southwest, east-northeast-west-southwest, and north-northwest-south-southeast. There are a number of discontinuous depressions flanked by rugged rock outcrops and exhumed corestones. The drainage lines and gullies are not well-defined. Human activities such as quarrying and mining in the area indicate that the hillside may have been altered.

The study area, including the landslide site, spans approximately +456 mPD and consists of a narrow, shallow valley that drains in a north-northeast direction. Numerous rock outcrops and steep cliffs characterise the upper part of the study area. Below these outcrops, the valley is draped with bouldery colluvial deposits, whilst the valley sides and spurlines expose residual soils, saprolitic soils, tors, and exhumed corestones. The drainage lines in the upper part of the study area are not well-developed, but they become more incised within gullies in the middle and lower parts. Further down, the main valley narrows and two main tributaries merge to form the rocky steam course, which flows north-northeast along the western flank.

Below the catchwater, the hillside of the lower catchment becomes much steeper with less deposition of colluvial deposits. Most relict landslides are located on the valley hillside above the catchwater and near the drainage lines. Only two relict landslides are evident on the hillsides below the catchwater and above the lower landslide scar (Figure 4.3). These landslides are probably a typical shallow failure in 1 m to 2 m of colluvium and saprolite. The source area of the upper landslide coincides with a local topographic depression, which is situated below a convex change-in-slope and near a relict landslide.

In contrast, the lower landslide does not appear to be a retrogressive failure of the relict landslide scar, as the failure mechanism (structurally controlled translational rockslide) appears different from that of the relict landslides. The source area of the lower landslide is located on a convex spurline with an incised rocky stream course to the west and a topographic depression to the east. Numerous exhumed corestones and tors are presented along the spurline before the 8 September 2023 incident. The API findings reveal that the topographic depression (i.e. anthropogenic break-in-slope) appears to have been modified and extended upslope by local excavations, possibly related to quarrying and artisanal mining (Section 3.1).

5   Description of the Incident

5.1   General

The following description of the incident has been collated from field observations, records from the Police and GEO, witness accounts, and the post-landslide inspections made by the GEO, AECOM, and Fugro.
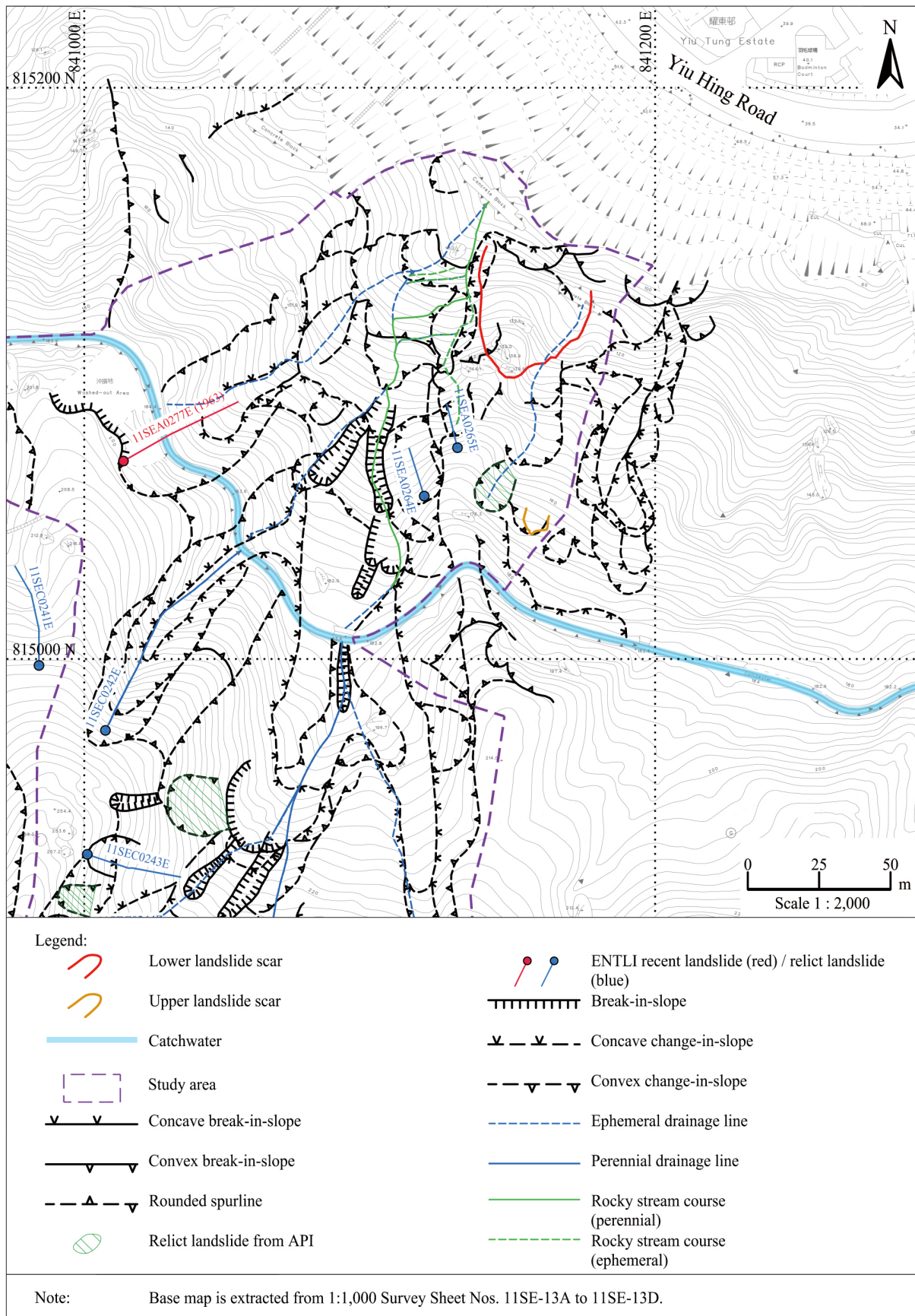
Figure 4.3   Site Geomorphological Setting

5.2 Records from Police and GEO

On 8 September 2023, at around 2:43 a.m., the Police received a report of a landslide between Yiu Hing House and Yiu Kwai House in Yiu Tung Estate on Yiu Hing Road, Shau Kei Wan. The HyD reported the incident to the GEO Emergency Control Centre at 4:00 a.m. GEO staff arrived at the scene around 5:25 a.m. Upon the arrival, no further landslides were observed.

5.3 Witness Accounts and Sequence of Incident

During interviews with residents nearby, those living in Yiu Tung Estate noted the landslide in the early morning on 8 September 2023, coinciding with a heavy rainstorm (Figure 5.1). This information was confirmed by reviewing CCTV footage from Yiu Tung Estate, which provided crucial details about the timing of the landslide.

Two sets of CCTV footage captured the moment of the landslide debris falling onto Yiu Hing Road from different angles, with timestamps confirming the occurrence at around 2:36 a.m. One of the CCTV cameras, installed at the pedestrian-covered walkway near Yiu Kwai House, recorded a car passing by the landslide location about two and a half minutes before the incident, indicating a near-miss situation. Key observations made from the footage are summarised below:

(a) At 02:34:00, a car was seen driving along Yiu Hing Road (Figure 5.2 (a)).

(b) At 02:36:46, a heavy 'splash' of clear water was observed, which may indicate a potential blockage or pooling of water immediately prior to the failure (Figure 5.2(b)).

(c) At 02:36:50, clastic debris began to be deposited on Yiu Hing Road, resulting in the destruction of a lamp post (Figures 5.2(c) and (d)).

(d) Four seconds later, at 02:36:54, a 'wave' of debris surged towards Yiu Kwai House, with several large rock blocks hitting and dispersing debris on the road (Figure 5.2(e)).

(e) No further landslides were observed after 02:36:56.

Another CCTV camera installed at the refuse collection point near Yiu Kwai House captured a 'wave' of debris surging towards Yiu Kwai House at around 2:36 a.m. The extracted CCTV footage has been thoroughly examined and is enclosed in Appendix B.

Based on the interpretation of the CCTV footage and records collected from the Police and GEO, it is believed that the incident occurred at around 2:36 a.m. on 8 September 2023. This incident took place during a heavy rainstorm that began on the night of 7 September 2023.

Figure 5.1 General View of the Landslide Site in the Early Morning on 8 September 2023 (Photograph taken by the nearby resident at about 4:00 a.m. on 8 September 2023)

a) At 02:34:00, a car driven along Yiu Hing Road, passing the lamp post before the incident.
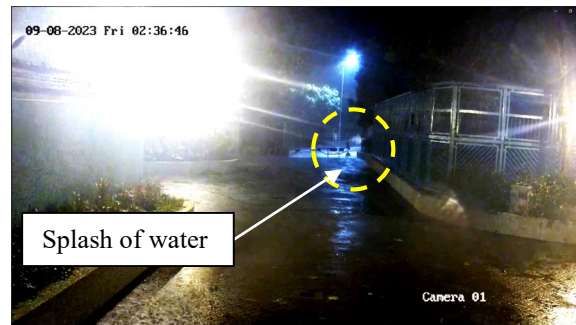
b) At 02:36:46, a heavy 'splash' of water hit the lamp post immediately before falling debris.

c) At 02:36:47, clastic debris fell onto and across Yiu Hing Road.

d) At 02:36:50, the lamp post was knocked down by debris.

e) From 02:36:54 to 02:36:56, a 'wave' of debris surged towards Yiu Kwai House, comprising large rock blocks hitting on the road.

Figure 5.2   Snapshots Extracted from CCTV Footage (Video taken on 8 September 2023)

6 Post-landslide Observations

6.1 General Observations

Key post-landslide observations are summarised below based primarily on inspections and field mapping undertaken by the GEO, Fugro, and AECOM (the counterpart landslide investigation consultants) between September 2023 and May 2024. The CAS assisted in the inspections and field mapping. As part of the inspections, the Survey Division of the CEDD used unmanned aerial vehicles (UAVs) to conduct topographic surveys of the landslide site. Figure 6.1 provides a general view of the landslide site, while Figure 6.2 summarises the post-landslide observations. Figure 6.3 displays the locations and directions of photographs taken during the post-landslide inspections.

On the early morning of 8 September 2023, two landslides (upper and lower) occurred on the natural hillside above Yiu Hing Road. The upper landslide was situated at the site of a pre-existing topographic depression on the hillside, and the lower landslide occurred on a spurline between the rocky stream course and the topographic depression.

Prior to the incident, the hillside was characterised by dense vegetation, consisting of tall shrubs and mature trees. The hillside had a steep incline of about 40° to 45° and featured exhumed corestones and tors on the spurline, along distinct, persistent northeast-southwest joint patterns in the rock outcrops within the rocky stream course (Figure 6.1).

The dimensions of the landslides varied significantly. Analysis of post-landslide photogrammetric data in comparison to the 2020 Light Detection and Ranging (LiDAR) data indicated that the source area of the upper landslide was about 8 m wide, 10 m long, and up to 1.3 m deep (measured perpendicular to the pre-landslide slope profile), with an estimated failure volume of about 100 m^3 (Figure 6.4). The landslide debris travelled approximately 30 m downslope and was deposited on the natural hillside. Some debris outwash travelled further downslope to the lower landslide scar.

The lower landslide was markedly larger, measuring about 40 m wide, 60 m long, and up to 6 m deep (also measured perpendicular to the pre-landslide slope profile), with an estimated failure volume of about 3,900 m^3 (Figure 6.5). The landslide debris, excluding the outwash, travelled about 150 m on plan, with a debris travel angle of about 30°. The impact of the lower landslide was extensive and damaging. The landslide debris completely damaged gabion wall ND10 (Figure 6.6) and partially damaged gabion wall ND9 (Figure 6.7). These walls were built in the early 1990s as boulder barriers as part of the Shau Kei Wan East Public Housing Development (Section 3.3.4). The landslide debris also entirely blocked one of the drainage outlet pipes underneath gabion wall ND9 on the left and partially blocked the inlets of the other two drainage outlet pipes (Figure 6.8).

Despite the partial blockage, the post-landslide inspections revealed that channel runoff was still able to flow through two of the drainage pipes. There were no indications of this runoff spreading around the partially damaged gabion wall ND9. The water continued to flow along the cascade below the gabion wall until it reached the blocked area, where it overflowed onto the cut slopes (Figure 6.9). Similar observations were made during a rainstorm on 4 May 2024 (Figure 6.10). No significant water was discharged from the weepholes in the retaining wall of slope No. 11SE-A/CR781.
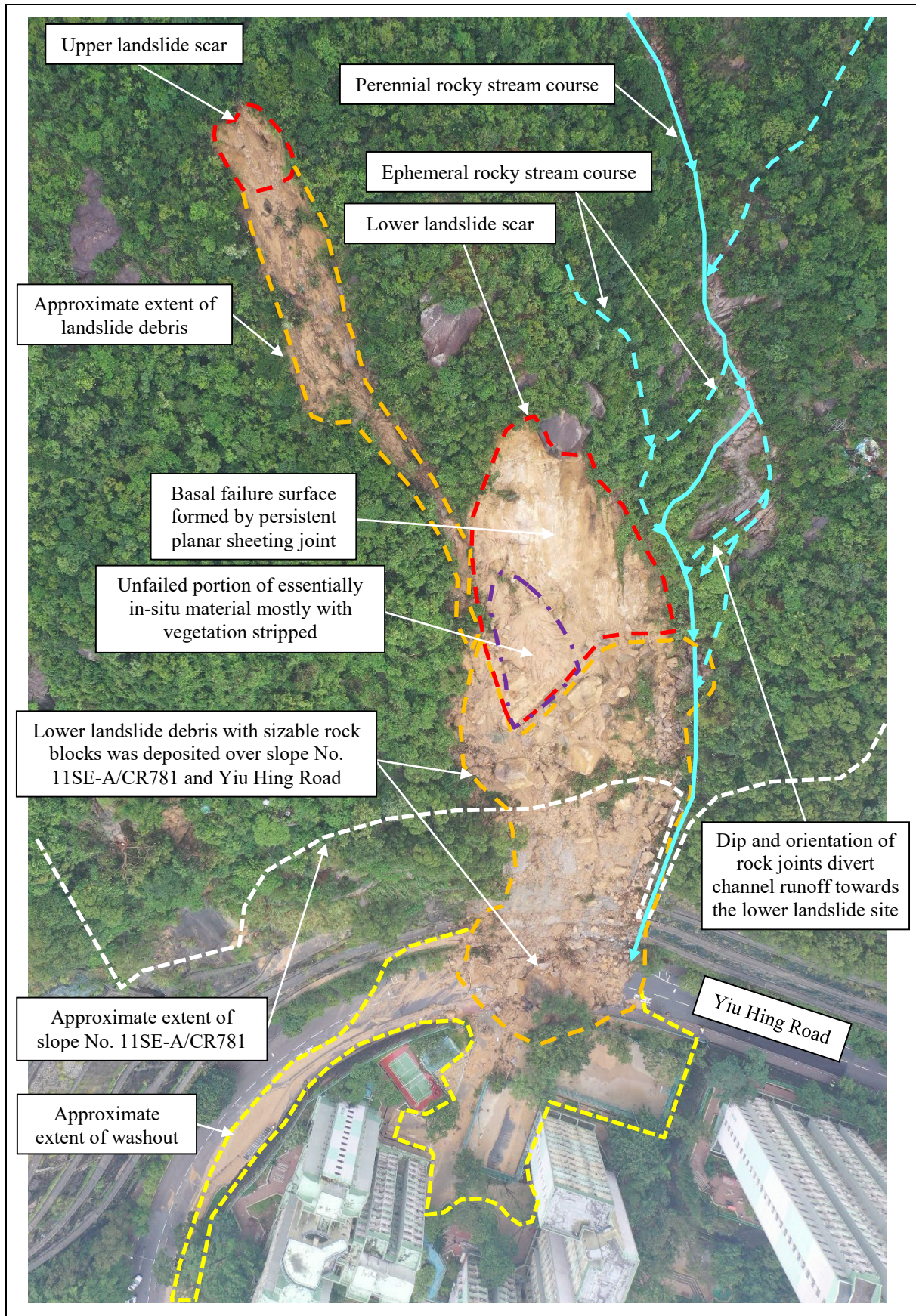
Figure 6.1   Overview of the Landslide Site (Photograph taken on 9 September 2023)
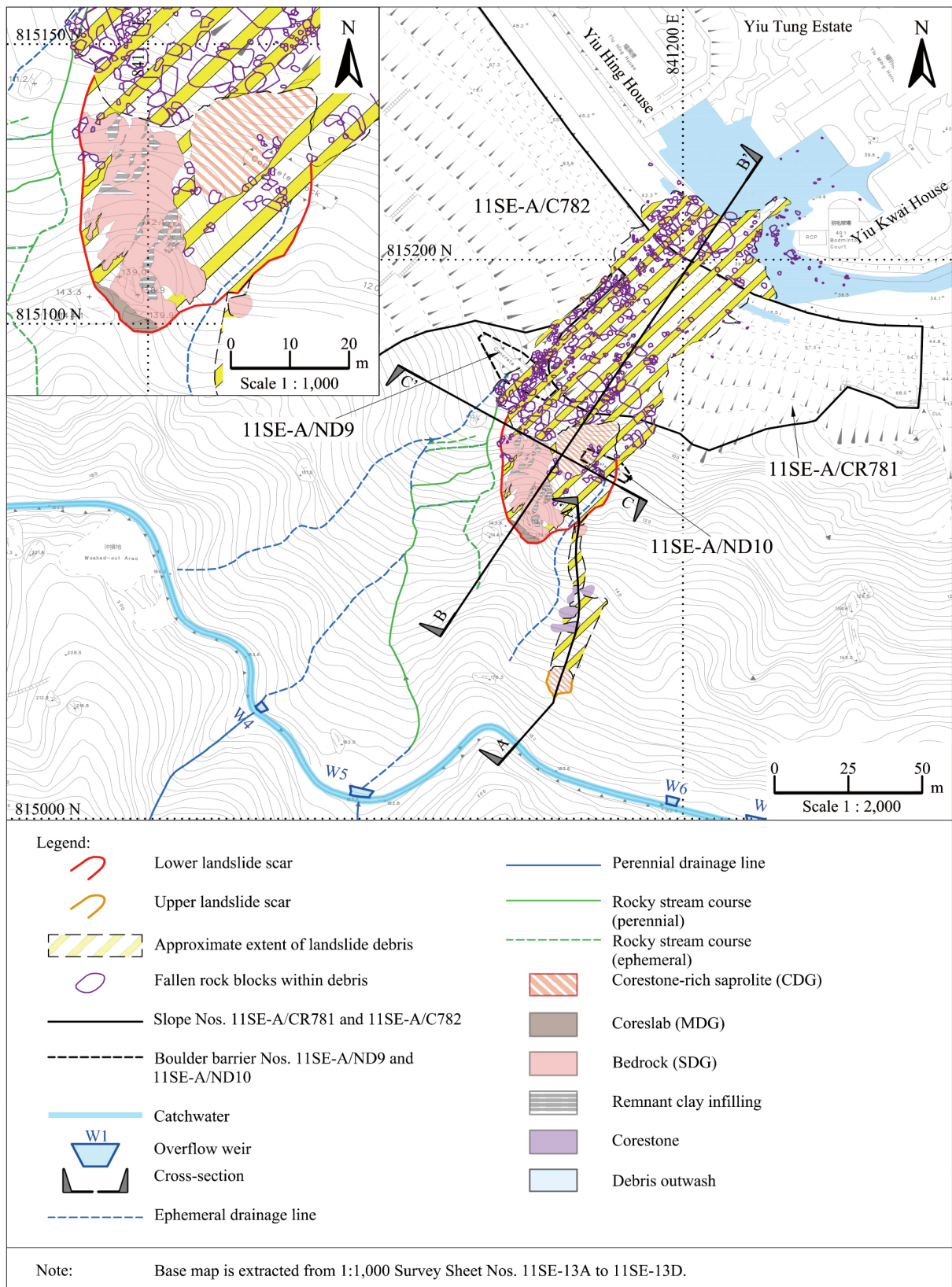
Figure 6.2   Post-landslide Observations
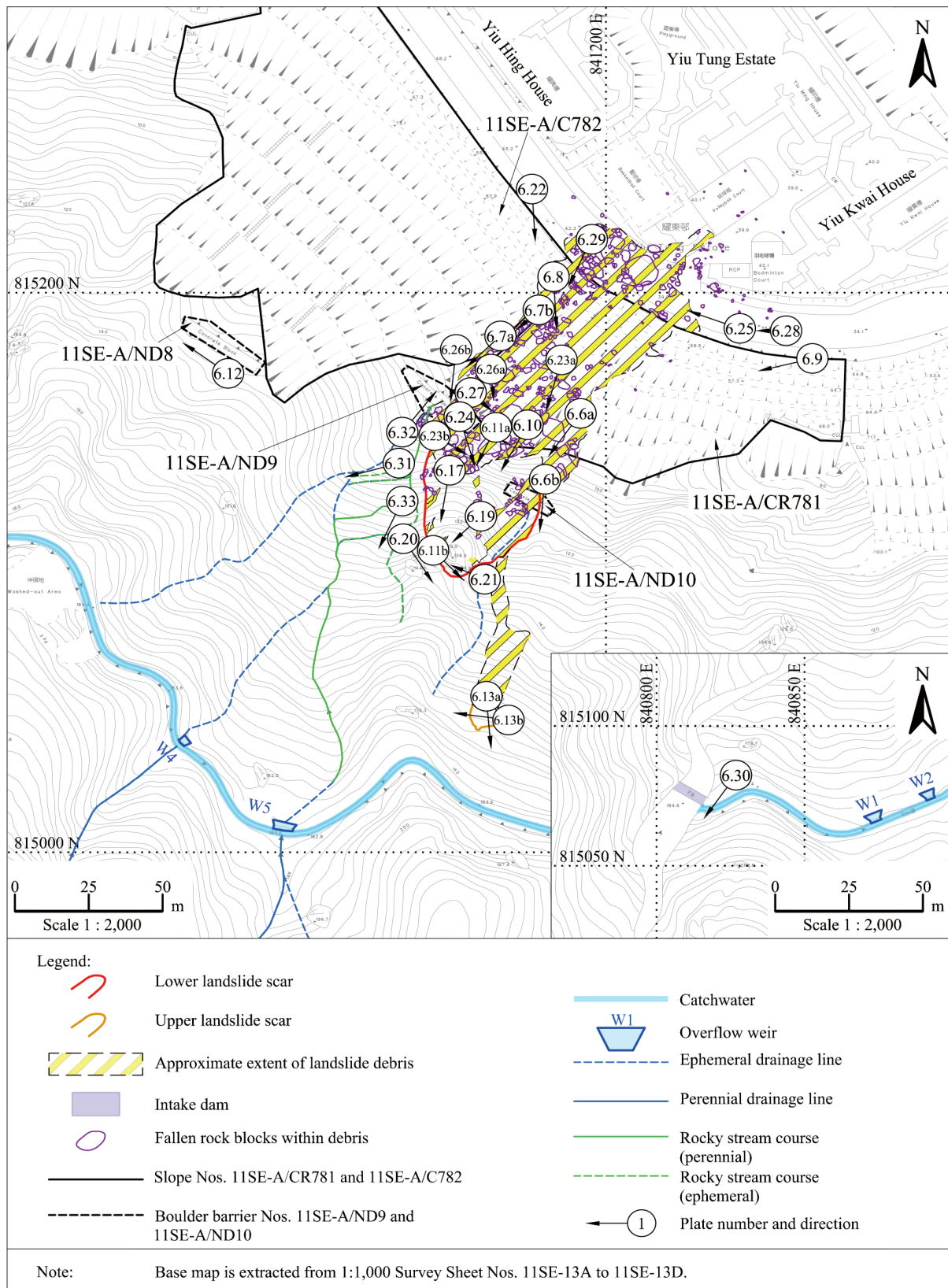
Figure 6.3   Locations and Directions of Photographs
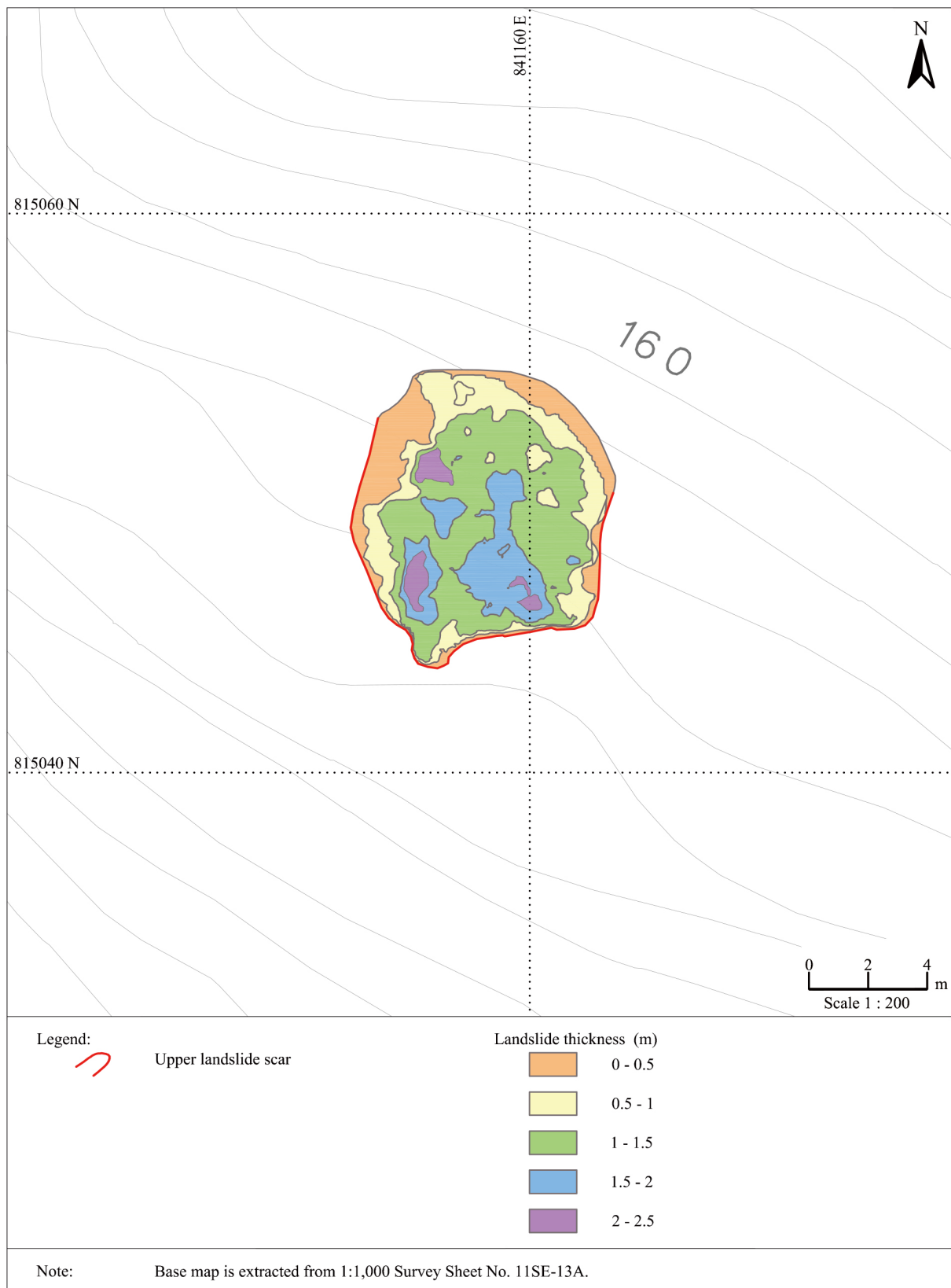
Figure 6.4   Source Volume Estimate of Upper Landslide Scar from LiDAR and Photogrammetry
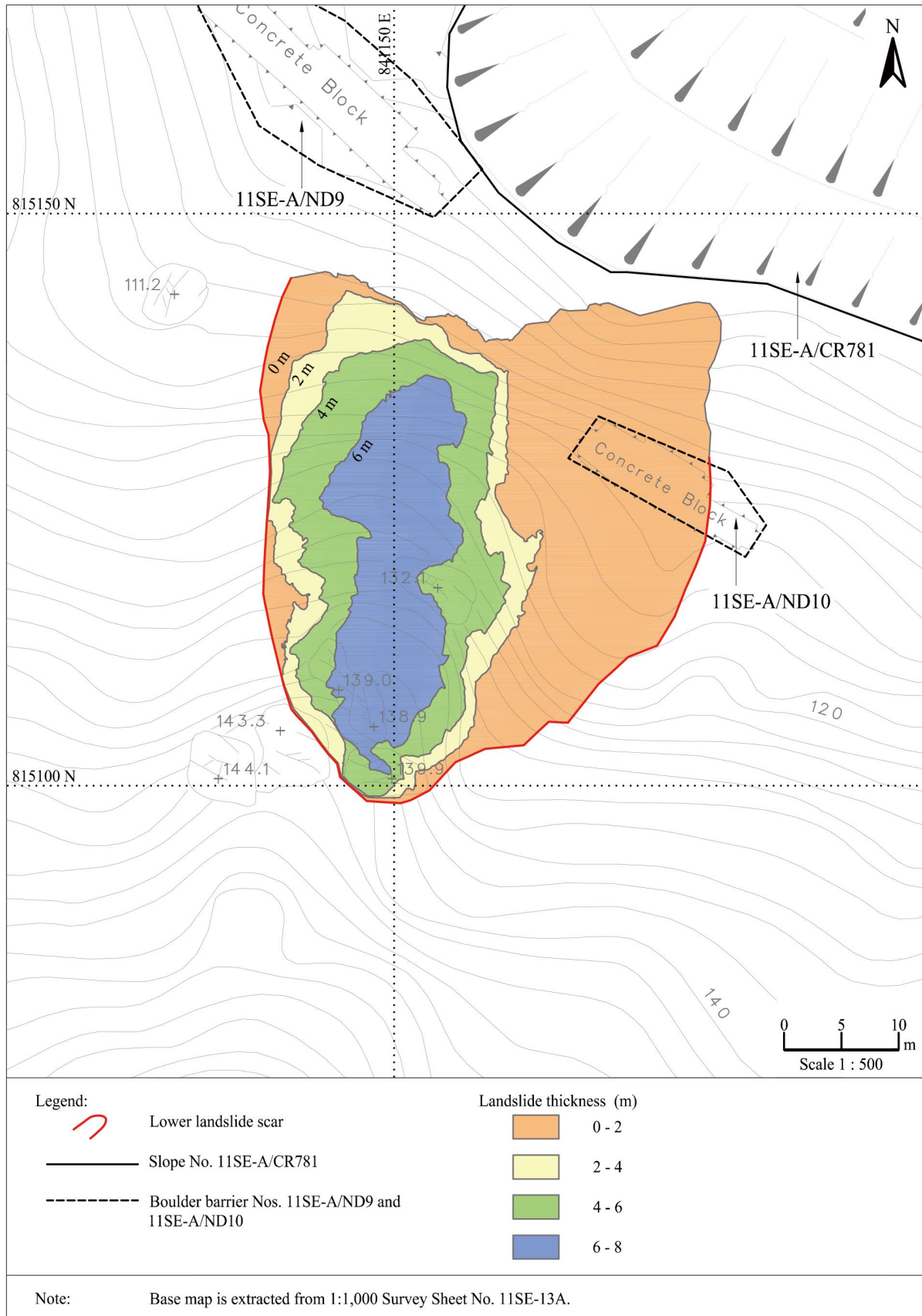
Figure 6.5   Source Volume Estimate of Lower Landslide Scar from LiDAR and Photogrammetry
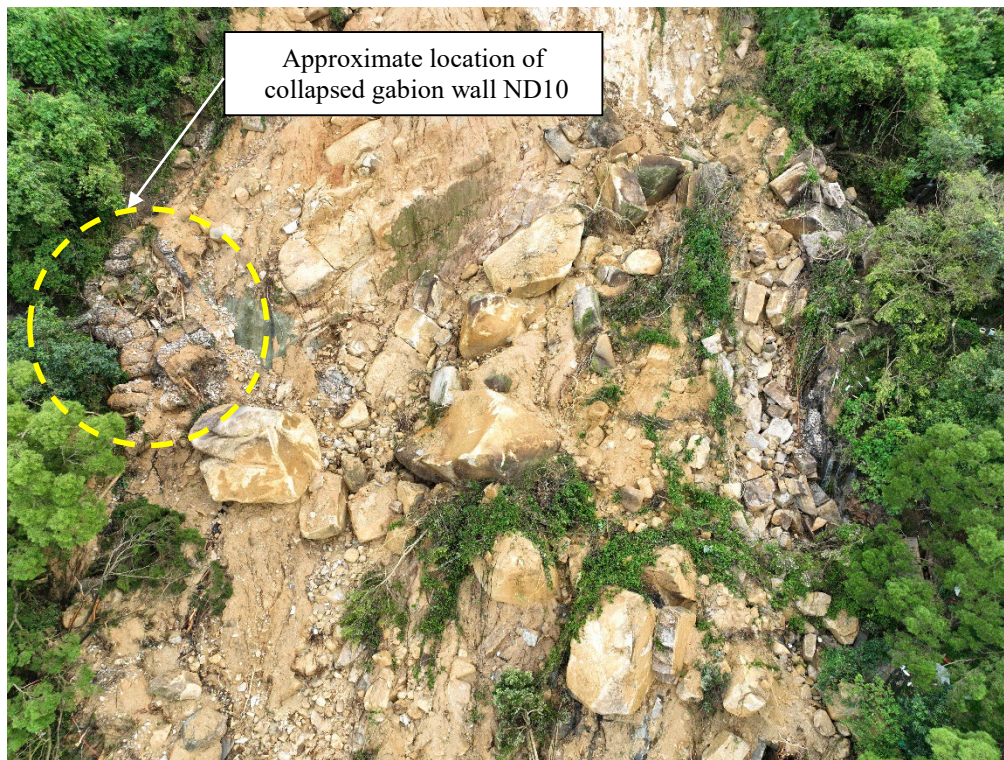
a) Collapsed Gabion Wall ND10

b) Remnant of Gabion Wall ND10

Figure 6.6   Close-up View of Gabion Wall ND10 after the Incident (Photographs taken on 15 September 2023 and 15 April 2024)

a) Partially Damaged Gabion Wall ND9

Eastern portion of gabion wall ND9 destroyed by debris

Western portion of gabion wall ND9 remained intact

2 m-wide cascade
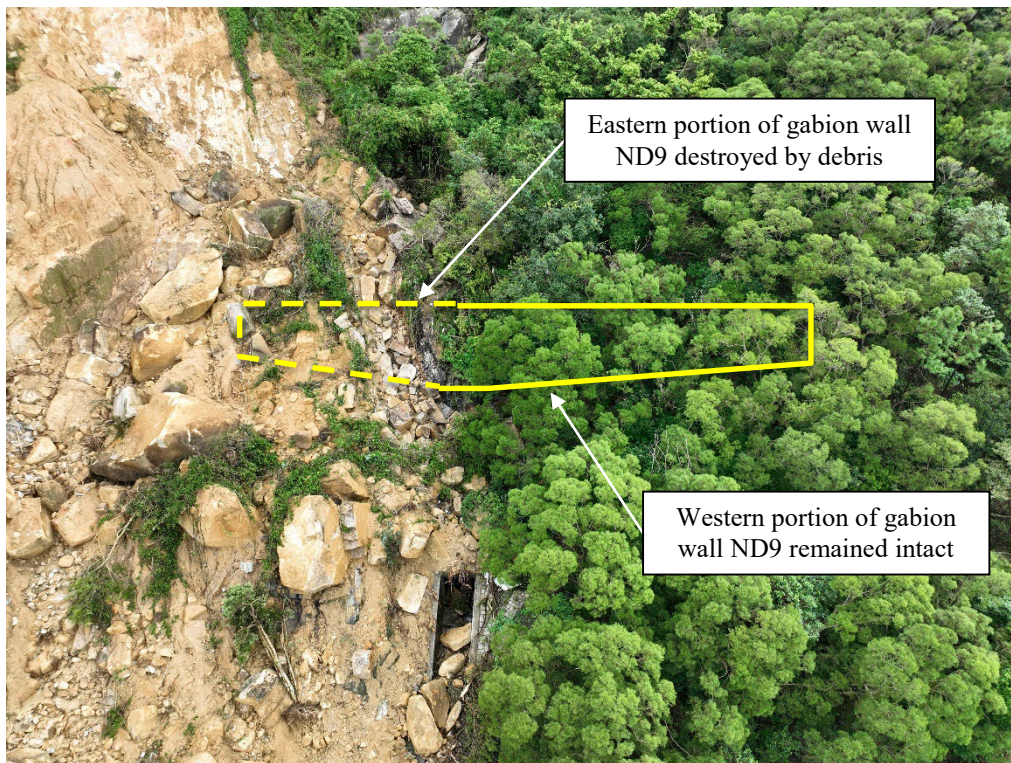
Cascade partially blocked by debris with rock blocks
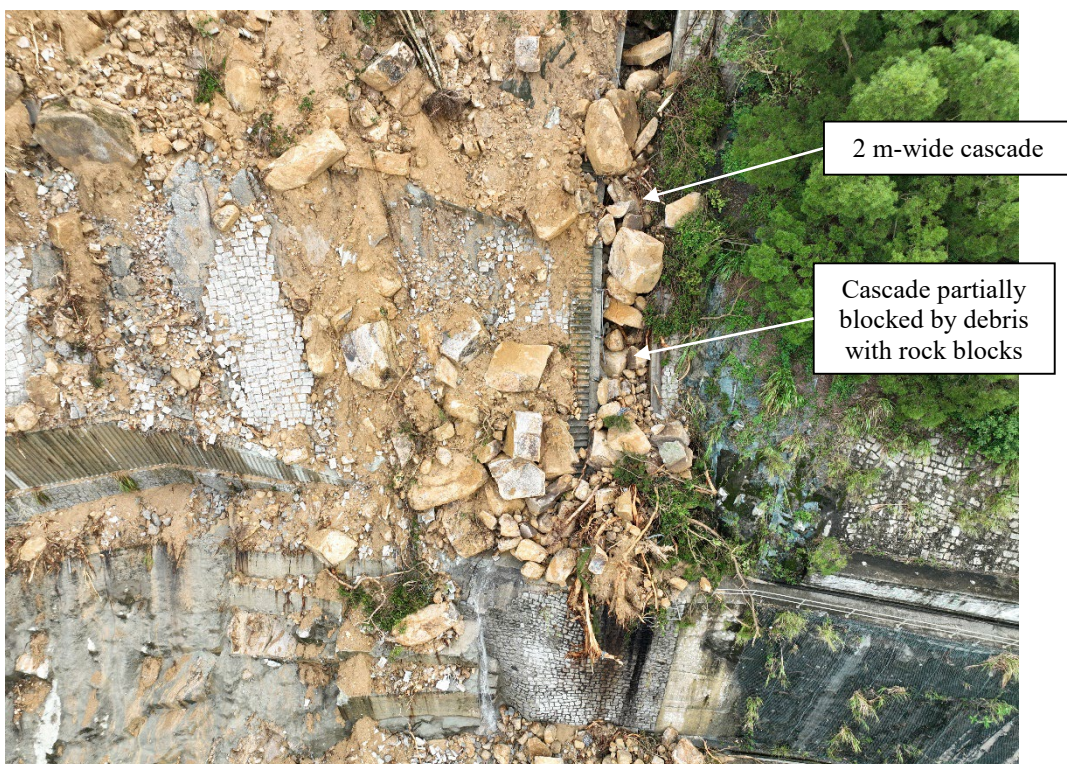
b) Cascade Partially Blocked by Landslide Debris

Figure 6.7   Close-up View of Gabion Wall ND9 after the Incident (Photographs taken on 15 September 2023)

a)   Drainage Outlet Pipes

b)   Partially Blocked Inlets of the Other Two Drainage Outlet Pipes

Figure 6.8   Conditions of Drainage Outlet Pipes underneath Gabion Wall ND9 after the Incident (Photographs taken on 12 December 2023)
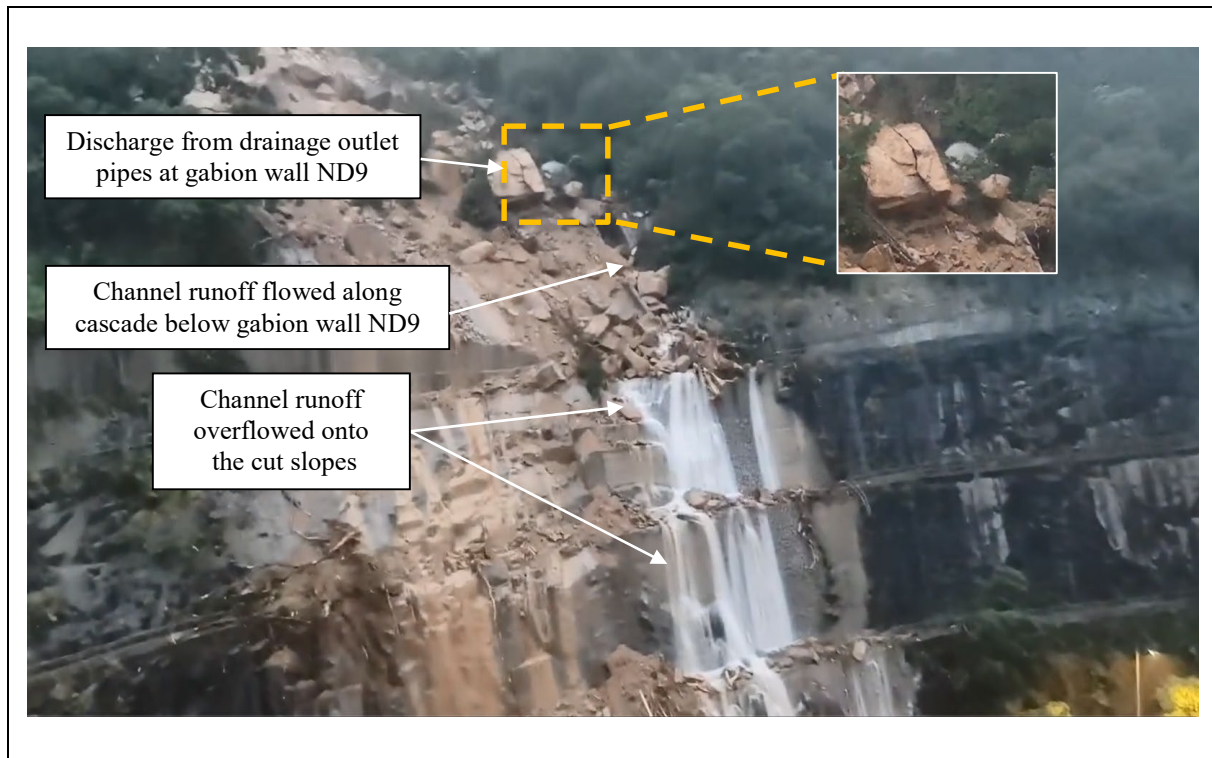
Figure 6.9   Channel Runoff along Cascade below Gabion Wall ND9 (Photograph taken on 8 September 2023)

Figure 6.10   Channel Runoff along Cascade below Gabion Wall ND9 (Photograph taken on 4 May 2024)

The landslide debris consisted of numerous rock blocks of varying sizes, ranging from 1 m to 11 m. This caused significant damage as the debris spread over the natural hillside above slope No. 11SE-A/CR781, cascade below gabion wall ND9, the cut slopes, and onto Yiu Hing Road. The debris completely blocked a section of Yiu Hing Road, leading to its closure for several months. It also caused varying degrees of damage to the nearby facilities, including subsurface drainage pipes, a lamp post, a bus stop, several parked vehicles, sports courts, and the windows of the nearby Yiu Kwai House. Notably, there were no significant damage to the cut slopes, aside from some drains that became dislodged and were left hanging from the slope surface.

Emergency repair works included the removal of the large rock blocks on the road and the cut slopes, and the provision of rock dowels and hard surface cover across the entire lower landslide site (Figure 6.11). Details of the emergency repair works are given in Leung et al (2024).

During the post-landslide inspections, a 1-m diameter boulder was found resting on the back side of gabion wall ND8 (Figure 6.12), leaving a dent in a gabion block. The gabion wall itself did not appear to be deformed or damaged. A runout path with flattened vegetation and exposed bare soil was observed on the natural hillside above the boulder's resting place.

Aerial inspections using UAVs revealed no other landslides in the vicinity.

6.2   Source Area of the Upper Landslide

The upper landslide was a small-scale, translational debris avalanche that initiated from an open hillslope (Figure 6.13). It is situated within an elevation range of +162 mPD to +168 mPD. Figure 6.14 depicts the geological profile of the upper landslide site along a longitudinal section A-A'.

The main scarp exposed a layer of topsoil and colluvium up to 0.5 m thick. The topsoil and colluvium layer consists of loose, yellowish-brown, silty SAND with occasional cobbles and boulders. Below this layer, there was a 1 m-thick layer of CDG with partially exhumed corestones of HDG. The CDG consists of very weak, yellowish-brown, silty medium to coarse SAND with gravel.

The rupture surface consisted of partially weathered rock with corestones, indicating that the failure occurred at the interface between colluvium and corestone-rich CDG. Some partially exhumed corestones were observed along the debris trail.

Post-landslide inspections revealed no seepage or soil pipes in the landslide scar area.

a) Emergency Repair Works at the Crest of the Lower Landslide Scar

b) Drillholes for Installation of Dowel Bars at Tor and Coreslab

Figure 6.11   Emergency Repair Works at the Lower Landslide Site (Photographs taken on 21 February 2024)
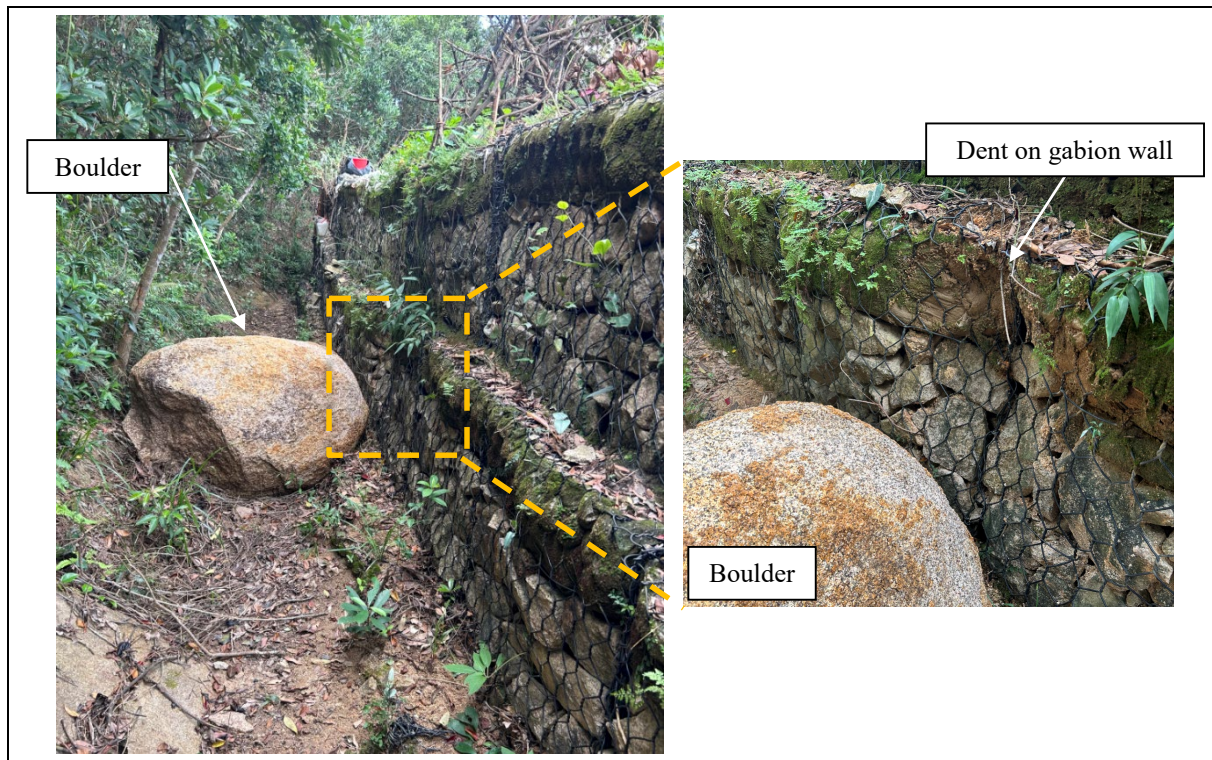
Figure 6.12   Boulder Arrested by Gabion Wall ND8 (Photograph taken on 26 September 2023)

6.3   Source Area of the Lower Landslide

The lower landslide was a massive-scale, structurally controlled, translational rockslide along a persistent, locally stepped, undulating to planar sheeting joint which formed the basal failure plane. The source area of this landslide is situated between +105 mPD and +138 mPD.

Figure 6.15 shows the geological profile of the lower landslide site along a longitudinal section B-B', and Figure 6.16 shows the geological profile of the lower landslide site along a transverse section C-C'. The locations of sections B-B' and C-C' are shown in Figure 6.2.

The sheeting joint is persistent and exhibits an inclination of approximately 30° to 35°, with a northeasterly dip direction at approximately 040°, which is the same as the natural slope orientation (Figure 6.17). The basal failure plane exposed SDG that daylighted out of the face of the natural hillside. Some pockets of pre-existing soil and mineral infill were observed along the sheeting joint, varying in consistency from hard, white silty clay seams measuring 10 mm to 20 mm thick, to softer, orangish-brown sandy clayey silt measuring up to 50 mm thick.

Asperities and undulations along the sheeting joint probably facilitated the formation of locally enhanced apertures and voids, where sediments could accumulate over time following subsurface soil erosion, transportation and deposition processes. Slickensided surfaces, which may have indicated pre-failure movements, were not observed on the basal failure plane. The formation of the sheeting joint is believed to be related to stress relief, with discontinuities developing parallel to the slope surface.
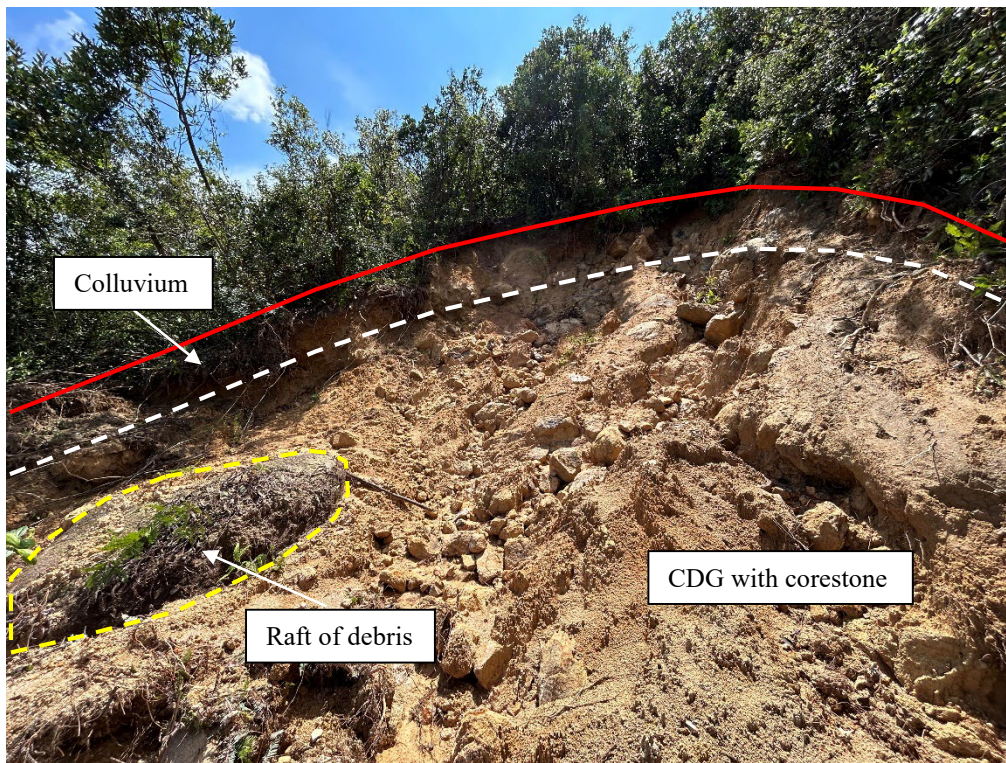
a) View of the Crest of the Upper Landslide Scar
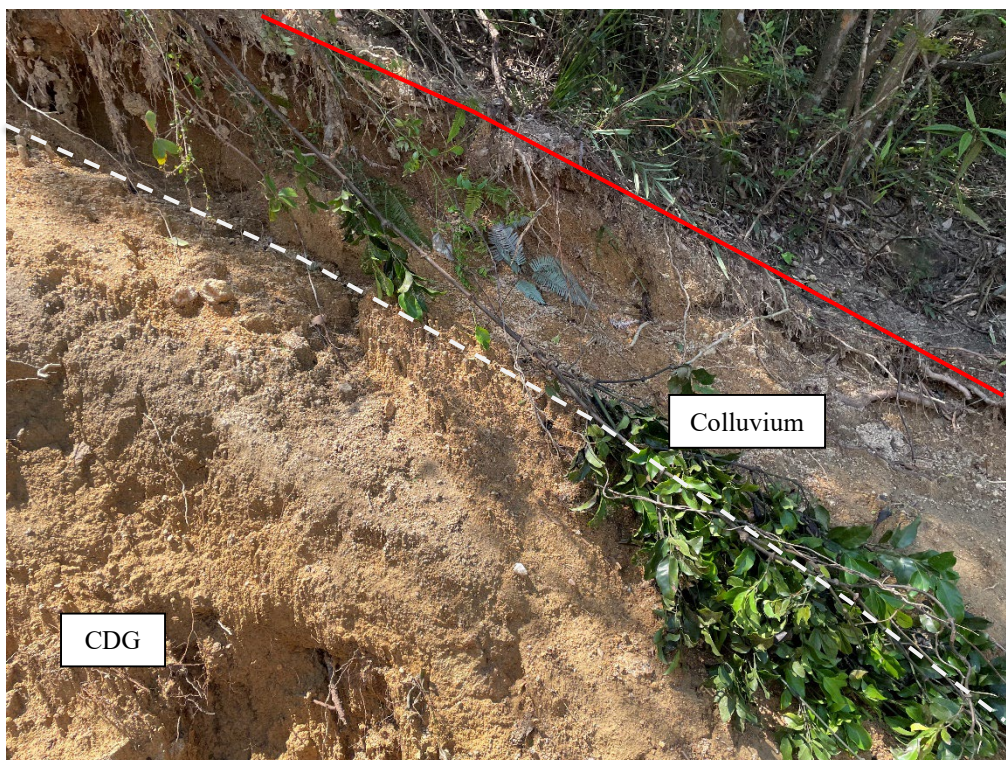
b) View of the Western Flank of the Upper Landslide Scar

Figure 6.13   Close-up View of the Upper Landslide Scar (Photographs taken on 19 September 2023)
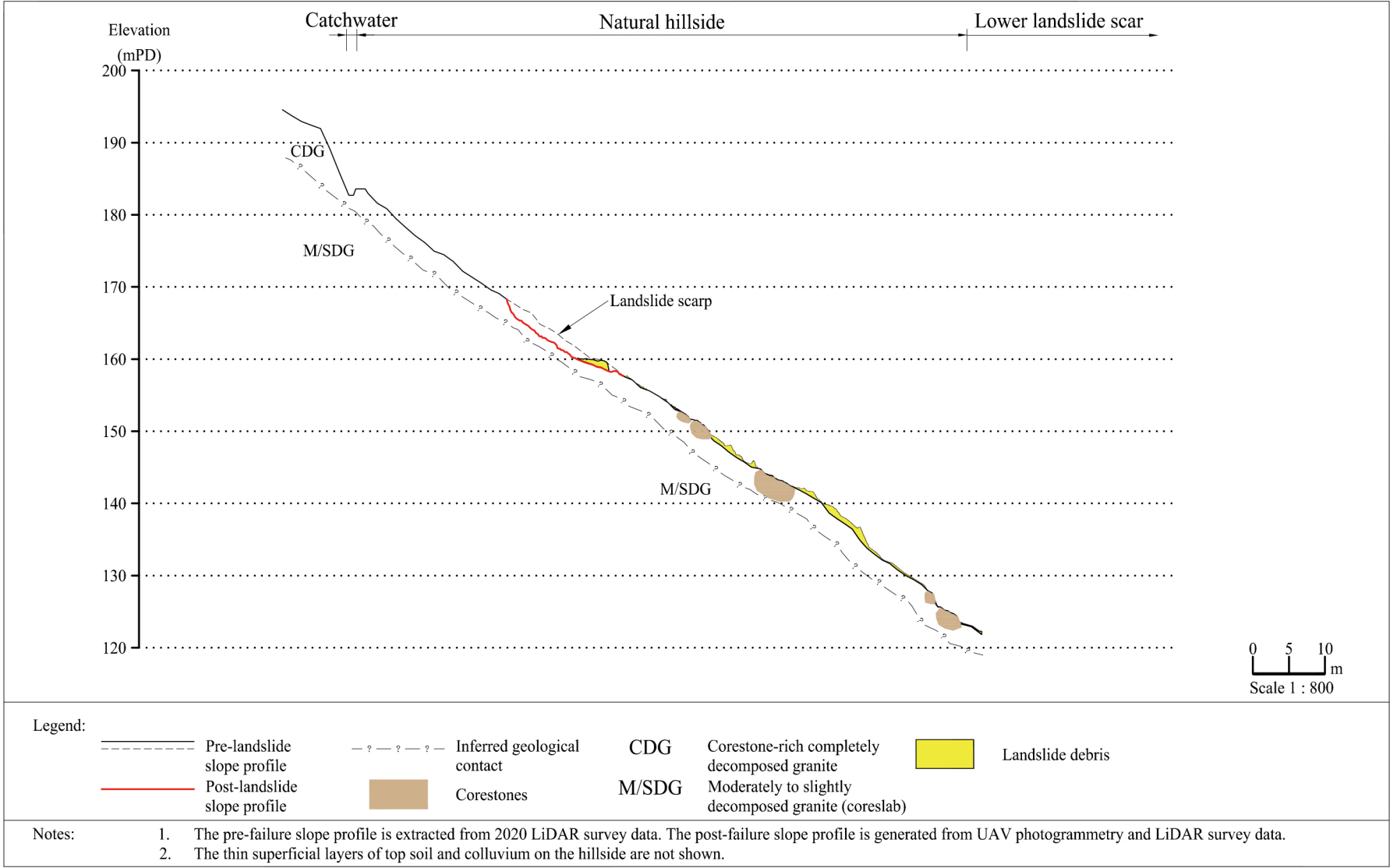
Figure 6.14   Geological Profile of the Upper Landslide Site (Longitudinal Section A-A')
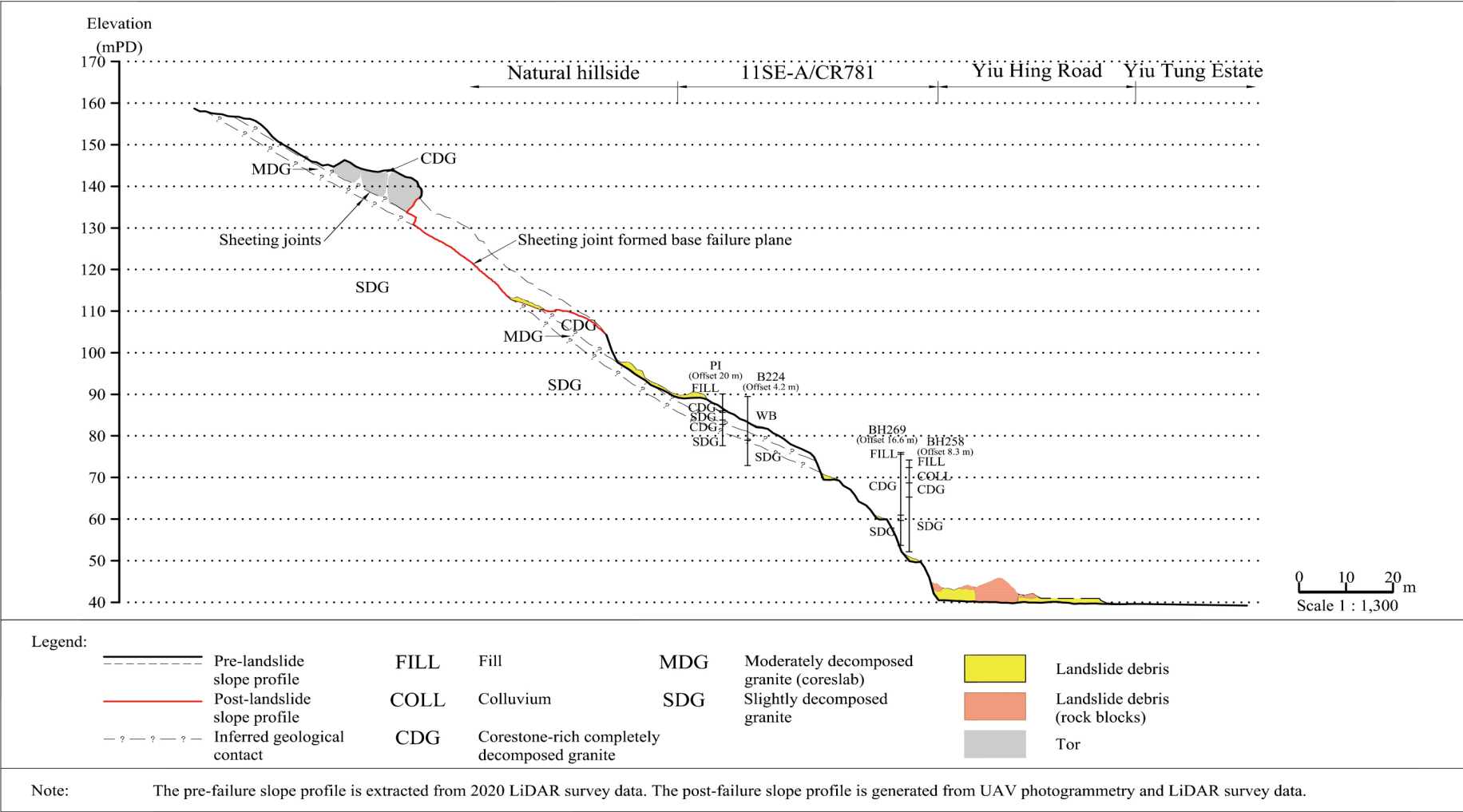
Figure 6.15   Geological Profile of the Lower Landslide Site (Longitudinal Section B-B')

Figure 6.16   Geological Profile of the Lower Landslide Site (Transverse Section C-C')

Labels on figure:
- Coreslab
- Stiff, white silty clay seam
- Soft to firm, yellowish brown, clayey sandy silt infill
- Surface of rupture
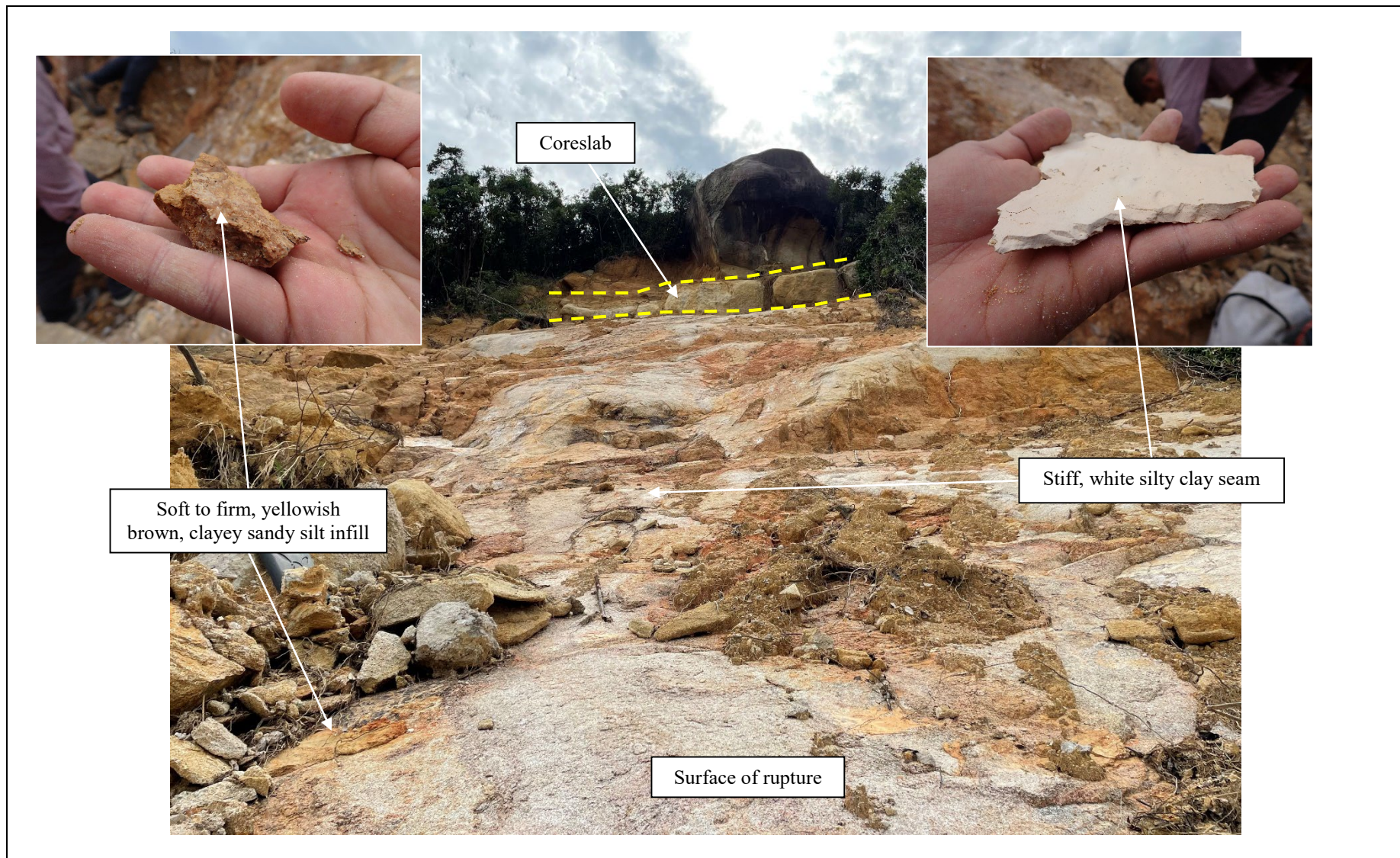
Figure 6.17 Close-up View of the Basal Failure Plane and Infill Materials (Photographs taken on 26 October 2023)

To assess the roughness of the basal failure plane, a 100-mm Barton Comb Profilometer was employed, conducting eight measurements across the lower portion of the basal failure plane. Additionally, 60 nos. of Schmidt hammer field tests were performed at and surrounding the lower landslide scar to determine the strength of the rock mass. Further details of the sheeting joint characteristics will be discussed in Section 8.4.

As discussed in Section 3.1, quarry and mining activities extended to the toe of the landslide source area. Field observations suggest part of the abandoned quarry face may have formed the toe of the west side of the landslide source area. However, the pre-landslide condition of this abandoned quarry face remains uncertain, as it was covered with dense vegetation. Given the presence of the persistent sheeting joint along the basal failure plane, it is possible that the sheeting joint daylighted in the abandoned quarry face.

At the crest, partially exhumed corestones and tors along the spurline were exposed by the landslide. They were mapped (CT-01 to CT-23) based on the 1963 aerial photographs, the post-landslide UAV photographs and the field mapping (Figure 6.18). One tor, CT-08, was exposed at the crown of the lower landslide scar and rested on a large tabular coreslab of MDG (Figure 6.19). The lower contact of this coreslab was bounded by a locally stepped and undulating, persistent planar sheeting joint. Soil infill was observed at the toe of the tor but did not extend further, indicating that CT-08 was partly in direct contact with the coreslab. The dip and dip direction of the coreslab was measured at 28°/025° and 33°/041°. Local dilation between the tor and the infill was observed around CT-08, and a 20 mm wide dilation was measured (Figure 6.20). Apparent soil pipes were observed between the basal failure plane and the coreslab. The postulated ground model for the crest scarp is shown in Figure 6.21.

Furthermore, based on the findings from the API and field mapping, as well as the interpretation of the post-landslide UAV photographs, it was determined that a tor, CT-11, was the largest rock block that fell onto Yiu Hing Road following the failure (Figure 6.22).

An unfailed, intact portion at the lower part of the lower landslide scar exposed saprolite and the coreslab, with vegetation stripped from the surface (Figure 6.23). This intact portion comprises CDG overlying partially exhumed coreslab. CDG consists of very weak, yellowish-brown, silty medium to coarse SAND with gravel.

As part of the emergency repair works, rock dowels were installed to stabilise tor CT-08 and the coreslab. A number of drillholes up to 6 m deep were completed and the available drill cores were examined (Figure 6.11(b)). The rock cores were generally described as moderately strong to strong, light yellowish grey, speckled pink and black medium to coarse-grained GRANITE with widely spaced, rough, planar joints.

Signs of seepage were observed on the mid-western flank, with seepage becoming more prominent following intense rainfall (Figure 6.24). Minor seepage was observed at the basal failure plane for a few months following the failure.
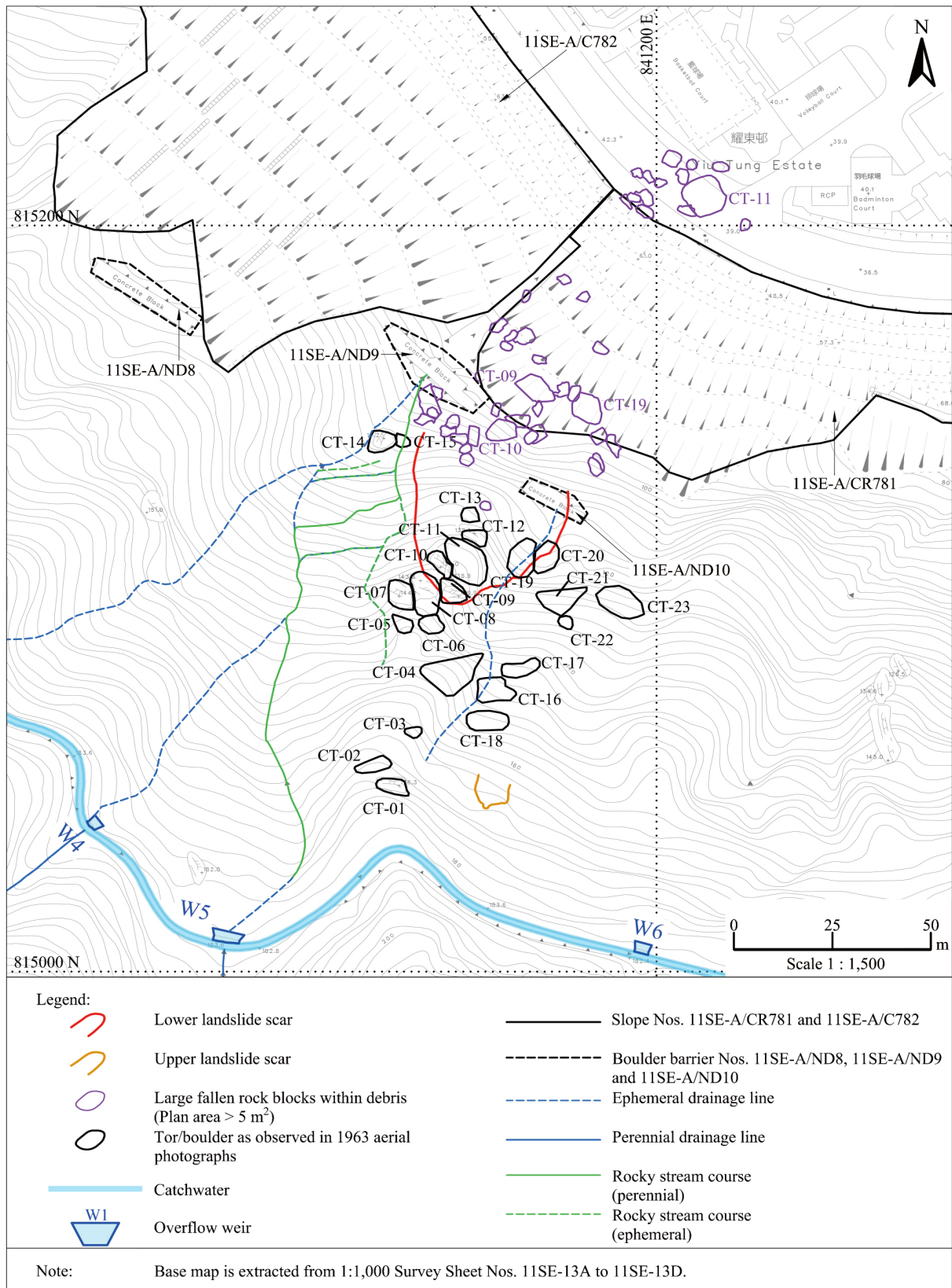
Figure 6.18   Distribution Map of Tors and Partially Exhumed Corestones

Displaced tor (CT-09)

Tor (CT-08)

Displaced tor (CT-10)

Exposed 'coreslab' of MDG (about 2 m thick)

Displaced tor (CT-11)

Approximate original locations of several large tors displaced by the landslide
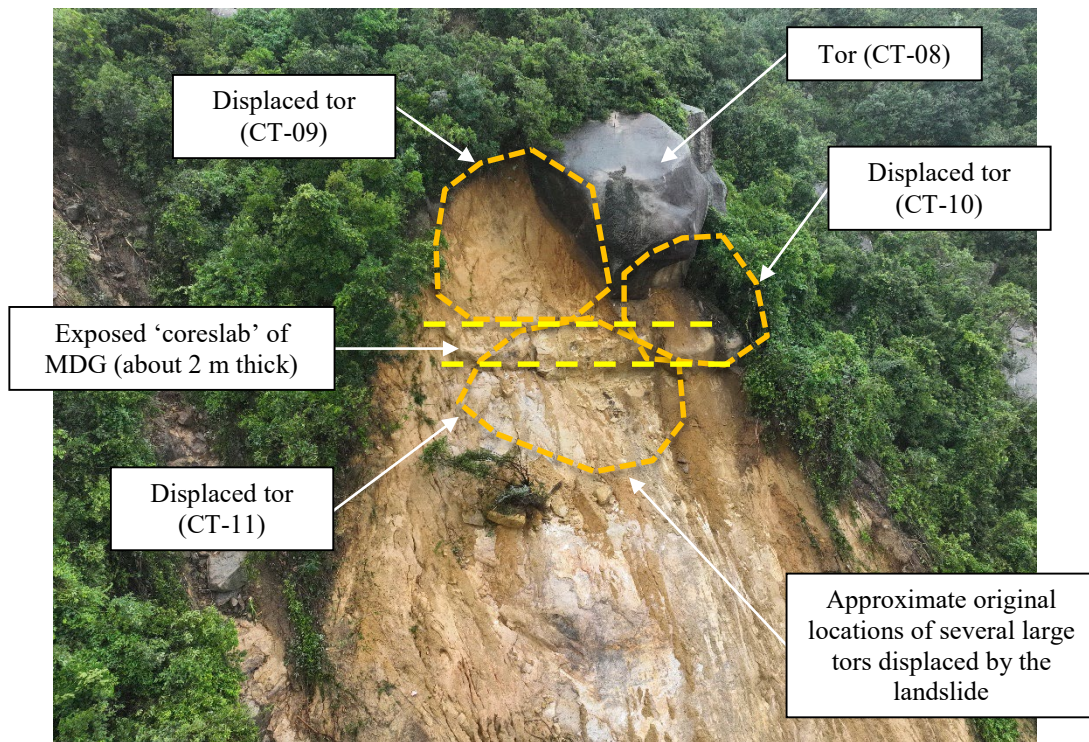
a) Tors at the Crest of the Lower Landslide Scar

Pre-existing soil infill

b) Close-up Vew of the Toe of Tor CT-08

Figure 6.19   Close-up View of the Lower Landslide Scar (Photographs taken on 9 and 14 September 2023)
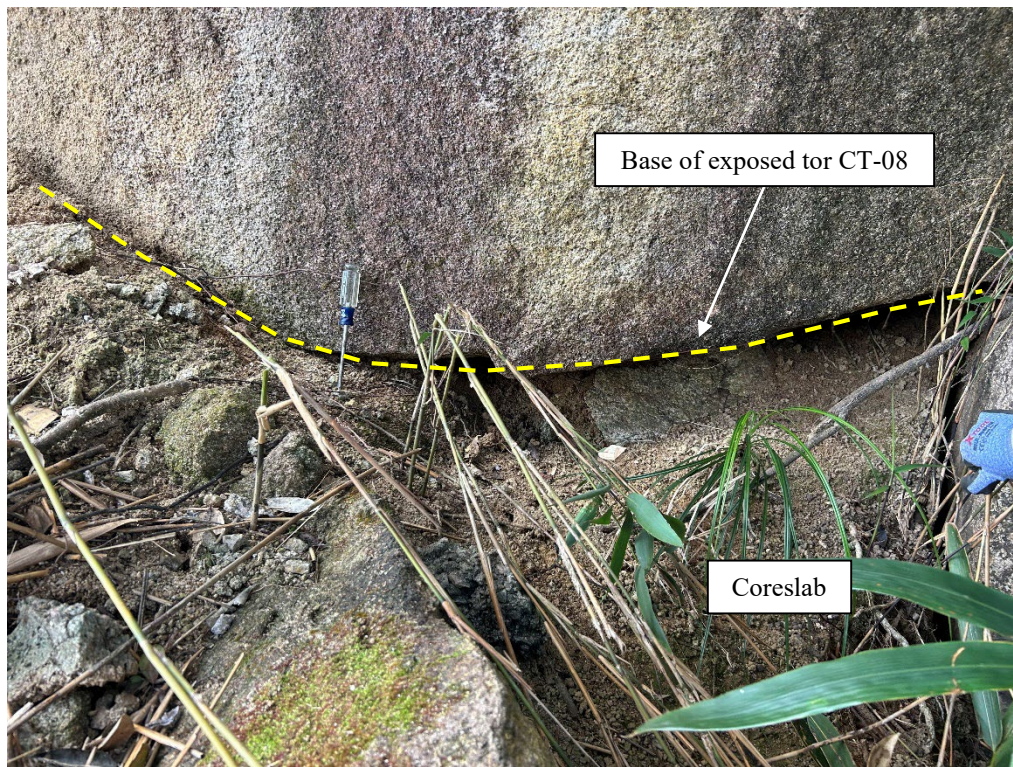
a) Contact between Tor and Coreslab

b) 20 mm Dilation at the Back of Tor

Figure 6.20   Close-up View of Tor CT-08 at the Crest of the Lower Landslide Scar (Photographs taken on 26 September 2023)
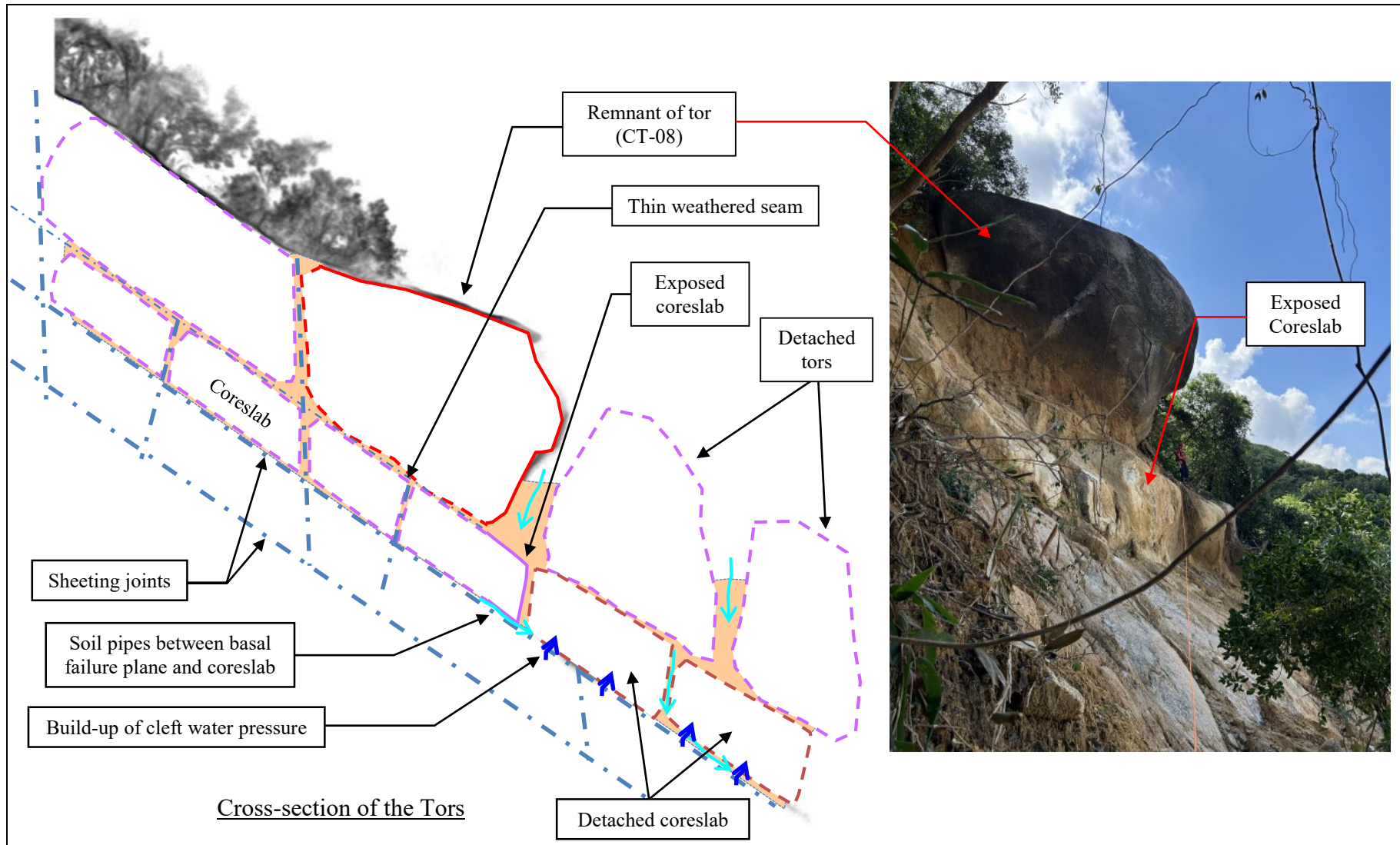
Figure 6.21   Ground Model for the Crest of the Lower Landslide Scar
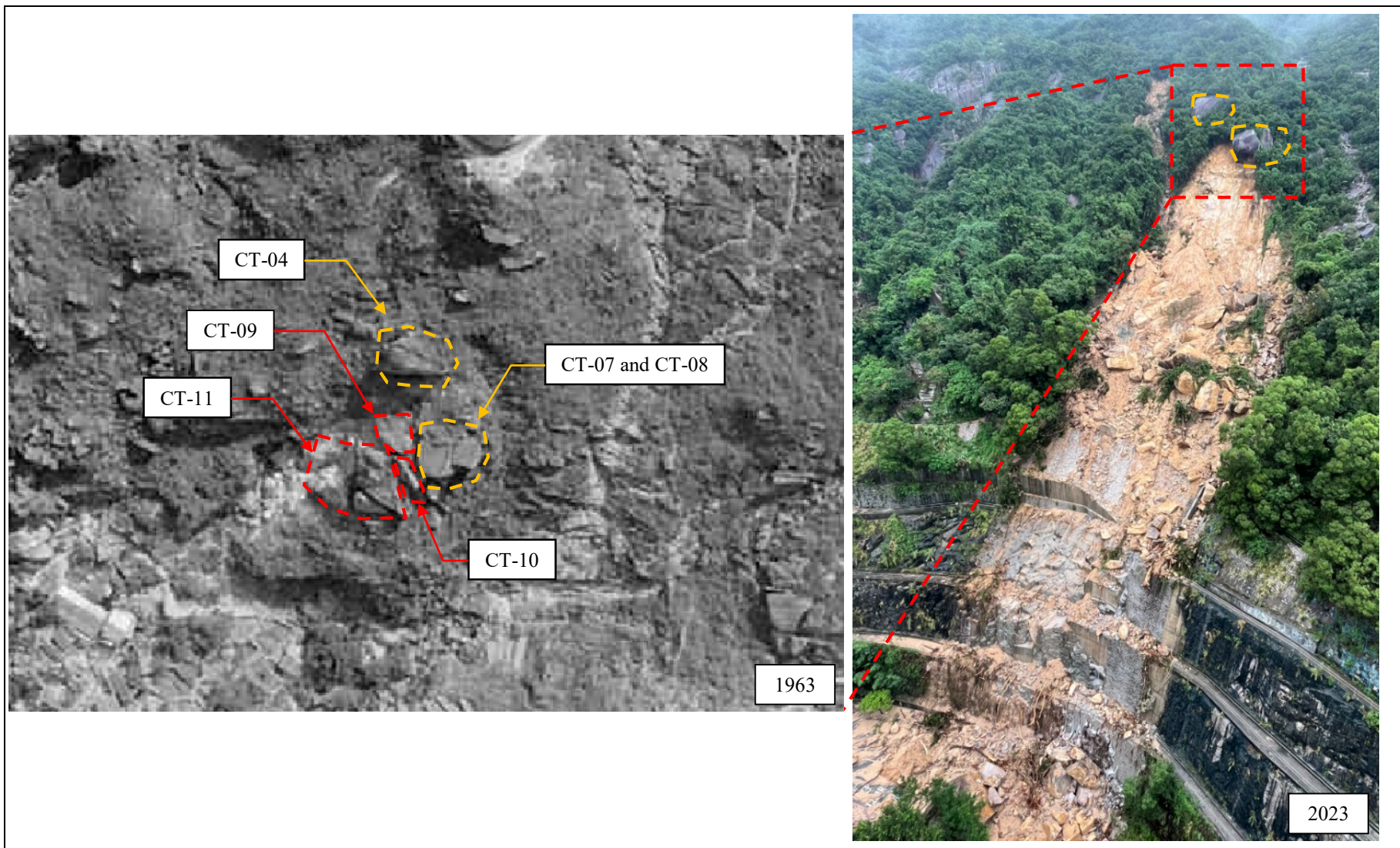
Figure 6.22   Tors in 1963 Aerial Photographs

a) Unfailed Portion at the Lower Part of the Lower Landslide Scar

b) Side Vew of the Unfailed Portion
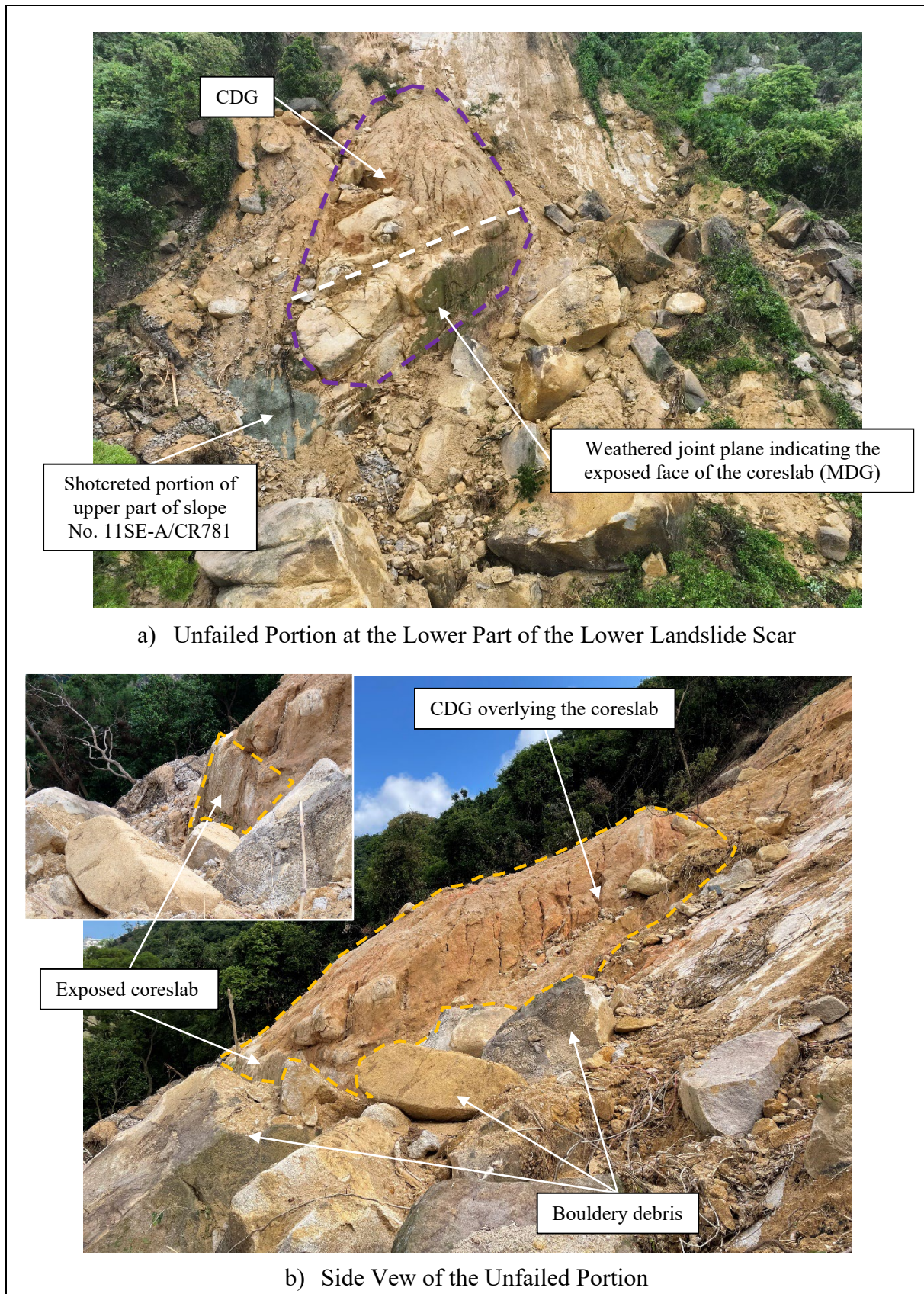
Figure 6.23 Unfailed and Intact Portion at the Lower Landslide Scar (Photographs taken on 9 September 2023 and 26 October 2023)
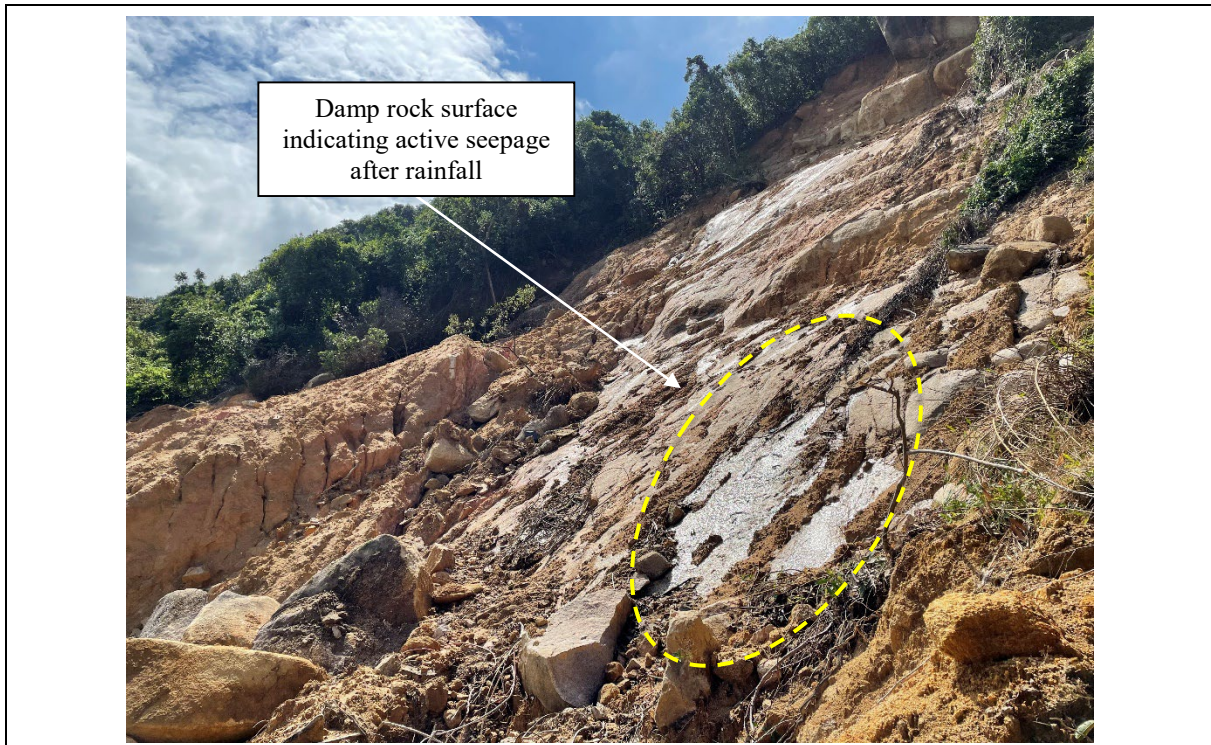
Figure 6.24   Evidence of Seepage on the Basal Failure Plane (Photograph taken on 11 October 2023)

6.4   Site Specific Geology

The geology of the landslide site was established based on the findings from the API (Section 3.1), previous ground investigation information (Section 3.4), published geological information (Section 4.1), and post-landslide observations (Section 6). The subsurface geology is described below:

(a) Topsoil and colluvium (up to 0.5 m thick) – loose, yellowish-brown, silty SAND with occasional cobbles and boulders.

(b) Corestone-rich saprolite (2 m thick) – very weak, yellowish-brown, CDG (silty medium to coarse SAND with gravel). Corestones and tors of MDG are included in this unit.

(c) Coreslab (2 m thick) – moderately weak, light yellowish-brownish grey, medium- and coarse-grained MDG. Coreslabs are bounded by sub-parallel persistent, planar sheeting joint. Thin patches of soil infill and white clay deposit of 10 mm to 50 mm thick were observed in the sheeting joint (typically 35°/032°) which formed the basal failure plane.

(d) Bedrock – strong to very strong, light grey, pink mottled and speckled black, SDG.

6.5 Landslide Debris

The lower landslide involved a massive-scale rockslide, with most of the landslide debris consisting of boulder-sized jointed rock blocks and cobble- and gravel-sized clasts. This type of material accounted for approximately 75% of the total failure volume. The rock blocks originated from the coreslab, corestones, and tors, while the soil debris primarily included sand and silt from topsoil and the CDG.

The largest fallen rock block, situated at Yiu Hing Road, measured approximately 11.5 m × 11 m × 5 m and weighted about 1,700 tonnes (Figure 6.25). In addition, there were several large rock blocks, ranging from 6 m to 10 m in length and scattering over the cut slopes, along with numerous smaller rock blocks measuring between 3 m and 5 m. Many of these rock blocks showed signs of weathering and staining, indicating that they had cropped out before the landslide occurred.

On the cut slopes and near the toe of the lower landslide scar, large rock blocks displayed clear signs of splitting along joints, indicating the forces at play during the landslide (Figure 6.26). Additionally, large tabular coreslabs were observed within the landslide debris, showing the complexity of the material involved. Remnants of concrete dentitions were observed within the landslide debris (Figure 6.27). They were probably part of the in-situ stabilisation works during the Shau Kei Wan East Public Housing Development in the early 1990s (Section 3.3.4).

The lower landslide also stripped away most of the original vegetation, with tree trunks and foliage scattered across the debris field (Figure 6.28). Isolated rafts of vegetation were observed at the lower landslide scar. Minor damages also observed on the cut slopes (Figure 6.29).

Figure 6.25 General View of the Largest Fallen Rock Block Situated at Yiu Hing Road (Photograph taken on 14 September 2023)
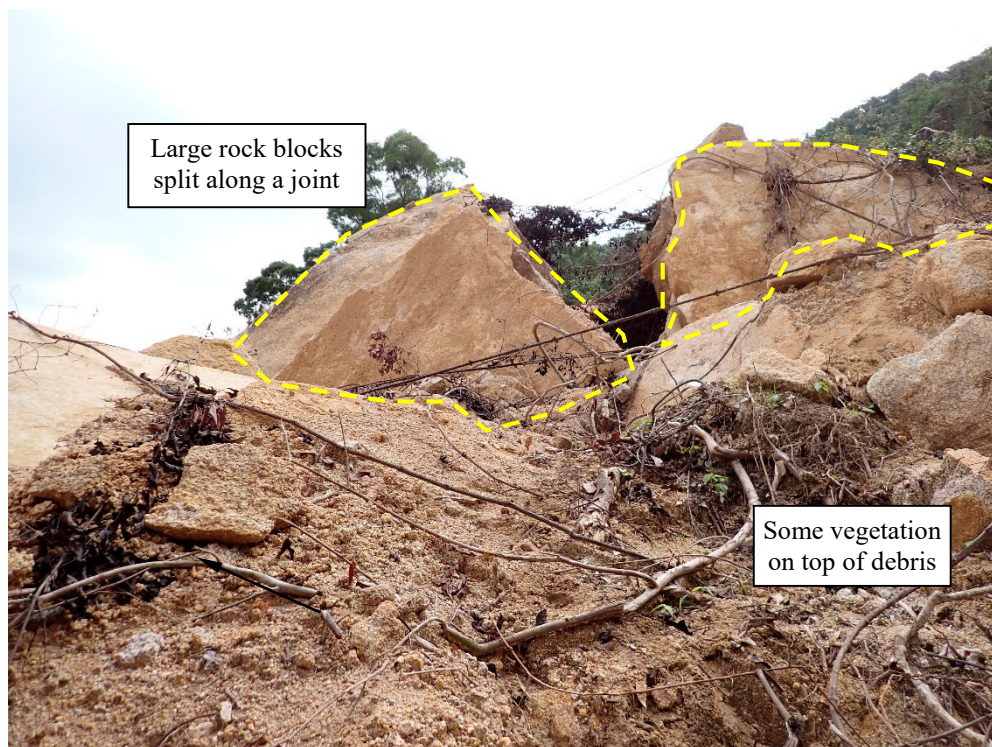
a) Split Rock Blocks

b) Tabular Rock Blocks Probably Slid Down along Basal Failure Plane into the Cascade

Figure 6.26   General View of the Debris deposited at the Toe of the Lower Landslide Scar (Photographs taken on 19 September 2023)

Figure 6.27   Remnants of Concrete Dentition at the Lower Landslide Scar (Photograph taken on 26 September 2023)
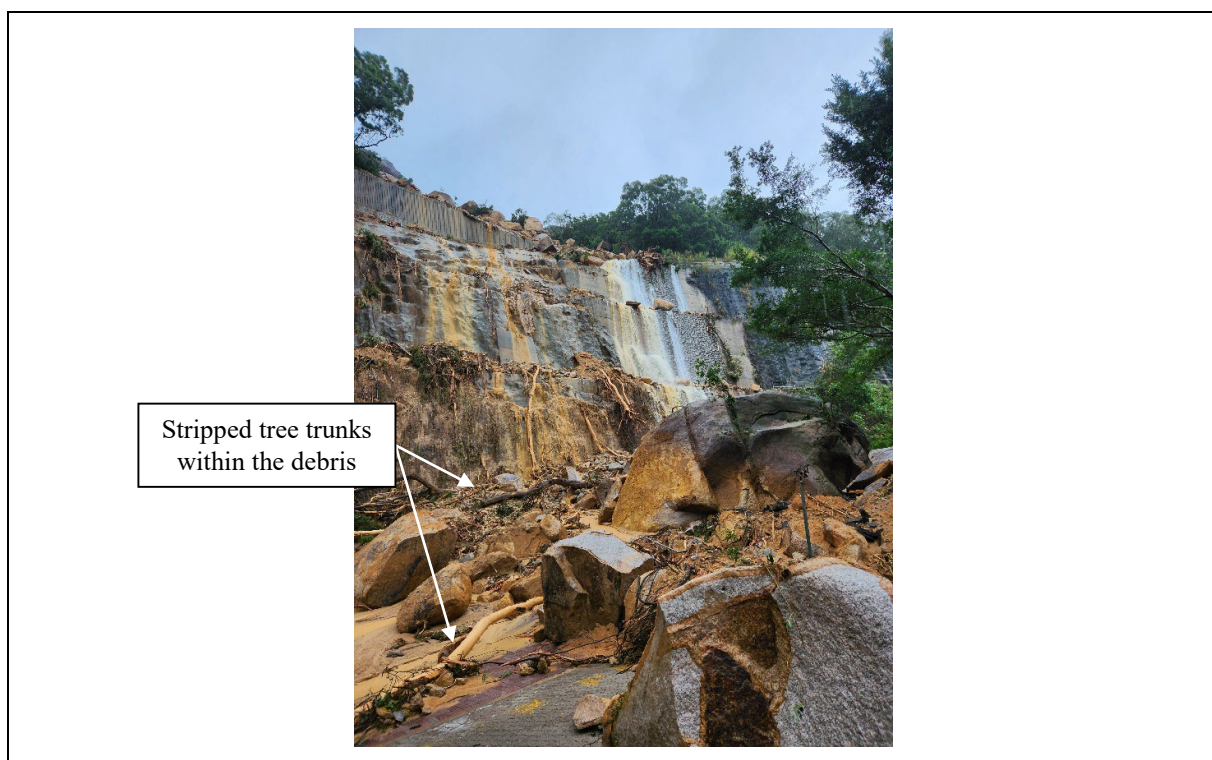
Figure 6.28   General View of Landslide Debris at the Toe of the Landslide Site (Photograph taken on 8 September 2023)

Figure 6.29   General View of Landslide Debris on the Cut Slope (Photograph taken on 9 September 2023)

6.6   Mount Parker Lower Catchwater

Following the landslide incident, inspections of the catchwater channel were conducted. The inspections revealed no signs of overflow, indicating that the channel functioned as intended during the event. Aside from a boulder found resting on the top of the catchwater channel near the intake dam (Figure 6.30), no blockages were observed.

Importantly, this boulder did not impede the flow of water from the intake dam into the catchwater channel or cause the water to back up. There were no signs of uncontrolled overtopping of the catchwater channel.

6.7   Rocky Stream Course

The hydrogeological conditions at the site were assessed by mapping the rocky stream course along the western flank. Exposed bedrock features in this area were inspected and their prominent joint sets were measured with typical orientations of 65°/005°, 80°/262°, 75°/354° and 35°/032° (Figure 6.31). In addition, steeply inclined open sub-vertical east-west striking rock joints at the rocky stream course were observed adjacent to the lower landslide scar (Figure 6.32).
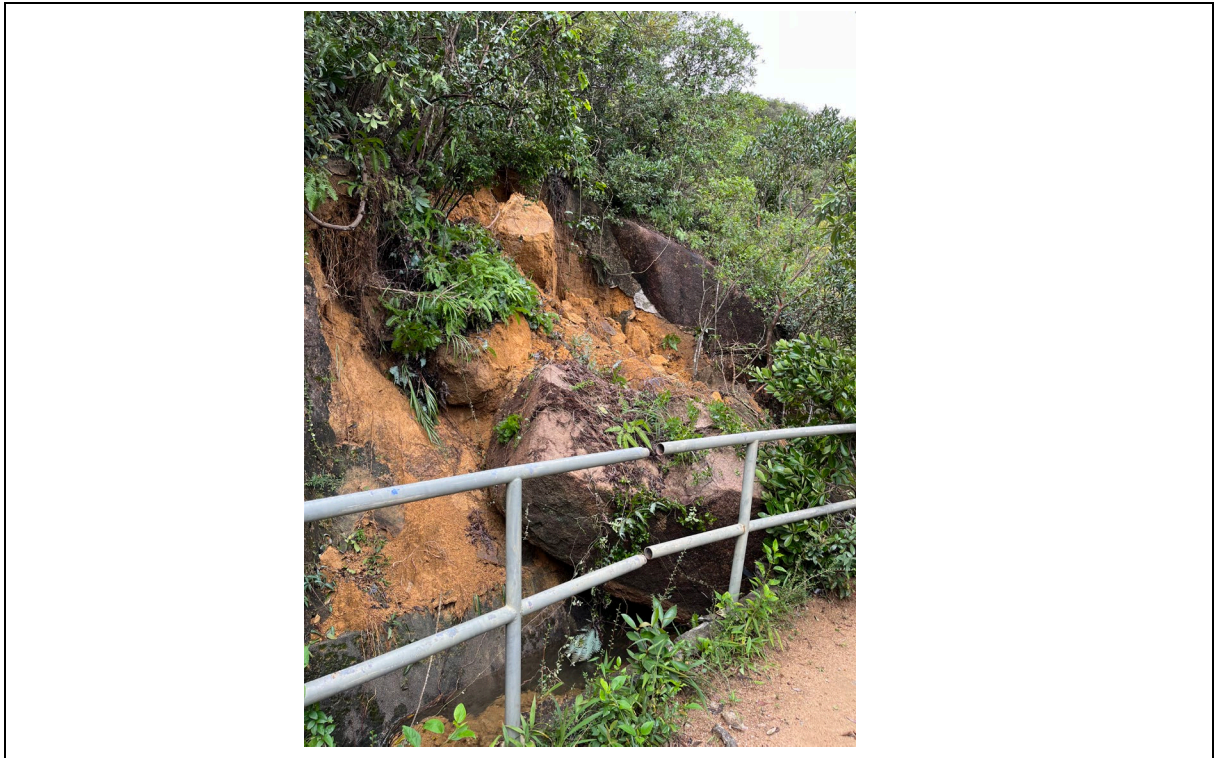
Figure 6.30   Boulder Deposited on Top of the Catchwater Channel near Intake Dam (Photograph taken on 13 September 2023)

Figure 6.31   Persistent Planar Joints Exposed along the Rocky Stream Course (Photograph taken on 26 September 2023)
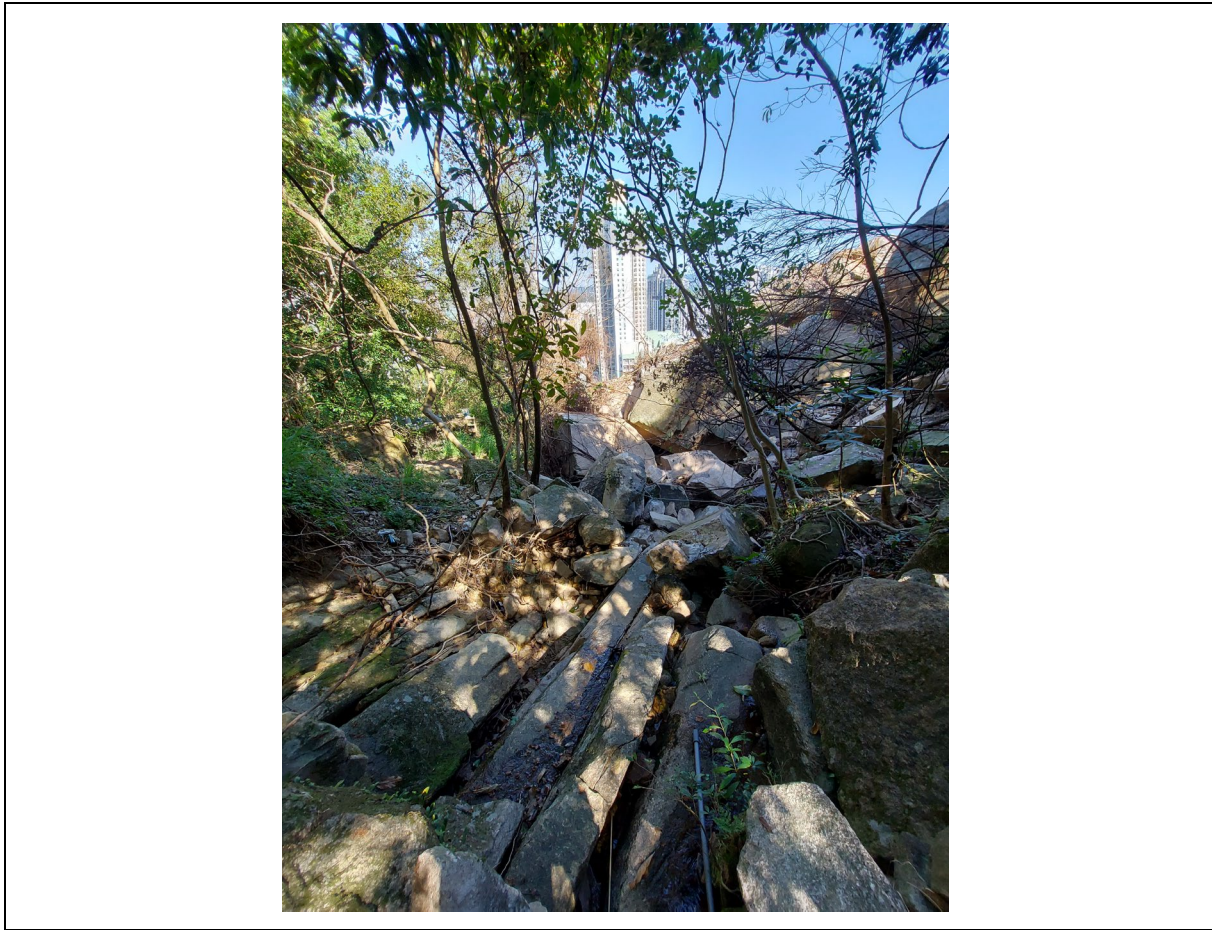
Figure 6.32   Persistent Open Rock Joints along the Rocky Stream Course Adjacent to the Lower Landslide Scar (Photograph taken on 1 November 2023)

Apart from the main perennial rocky stream course, a minor ephemeral rocky stream flows in a depression on the western flank. During the post-landslide inspections, channel runoff was observed flowing from the main perennial rocky stream course along these open rock joints into the ephemeral stream (Figure 6.33). Notably, active channel runoff flow was observed even during dry weather, indicating a level of perennial flow.

Channel runoff in the non-confined rocky stream course spreads laterally and is significantly influenced by undulating rock outcrops. These joints appear as a cascade of vertical steps and drops, which is consistent with previous observations noted in the Geotechnical Area Study (Section 3.3.3). The persistent, open sub-vertical east-west striking joints, which have been exacerbated and widened by prolonged weathering and erosion, provide a preferential pathway for runoff flowing eastward from the rocky stream course and seeping into the lower landslide scar during heavy rainstorms.

Figure 6.33   Minor Ephemeral Rocky Stream Course at the Western Flank of the Lower Landslide Scar (Photograph taken on 15 April 2024)

7   Analysis of Rainfall Records

Rainfall data was obtained from the nearest GEO Raingauge No. H19, which is located at about 500 m northeast of the landslide site (Figure 1.1). This raingauge records rainfall data at 5-minute intervals. Figure 7.1 shows the daily rainfall recorded by the raingauge between 9 August 2023 and 10 September 2023, and the hourly rainfall recorded between 8:00 a.m. on 7 September 2023 and 8:00 p.m. on 8 September 2023.

Table 7.1 and Figure 7.2 present the maximum rolling rainfall for various durations and the comparison of the 7 to 8 September 2023 rainstorm with previous major rainstorms recorded at GEO Raingauge No. H19. It can be seen that the 4- to 24-hour rolling rainfall preceding the landslide on 8 September 2023 hit record highs, with the estimated return periods falling between 49 years and over 500 years.

The Gumbel parameters of the raingauge were derived based on the frequency analysis of extreme rainfall using 40 years of rainfall data (Chan & Chu, 2024). The large extrapolation of these available data inevitably resulted in considerable uncertainties in determining the return periods of the record-breaking rainstorm events (Wong & Ho, 1996). Nevertheless, the analysis results indicate that the intensities of 4- to 24-hour rolling rainfall of the 7 to 8 September 2023 rainstorm were the severest ever recorded by GEO Raingauge No. H19 since it came into operation in 1984.
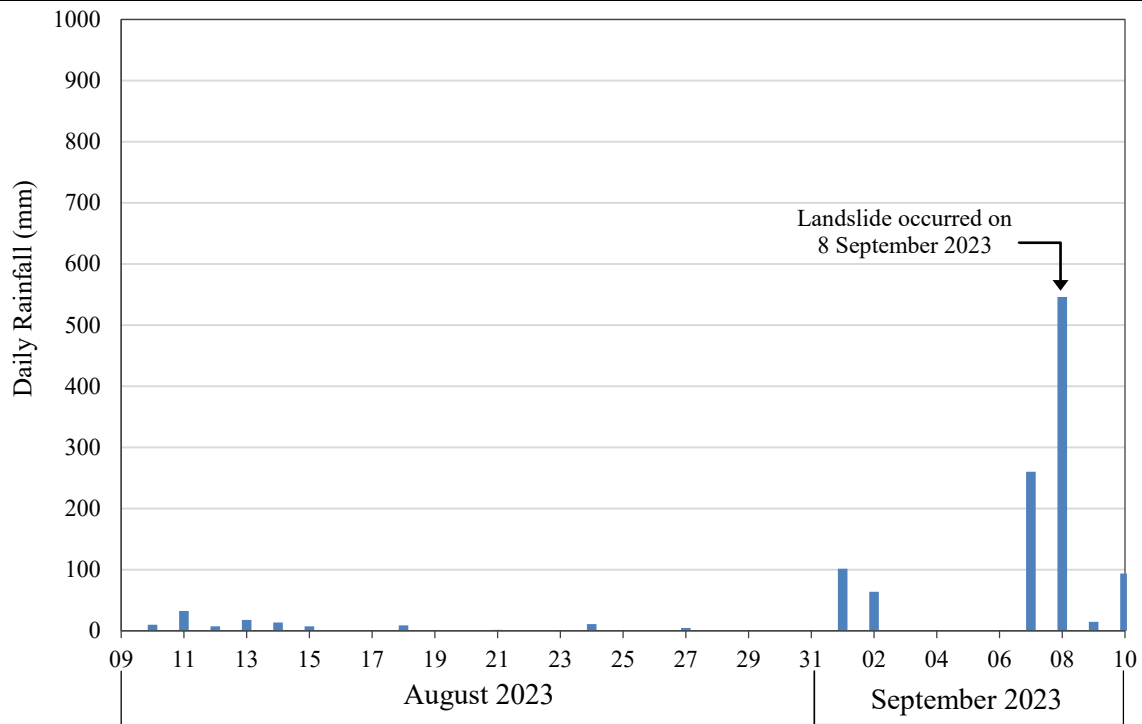
(a) Daily rainfall recorded between 9 August 2023 and 10 September 2023
based on clock-hour rainfall data
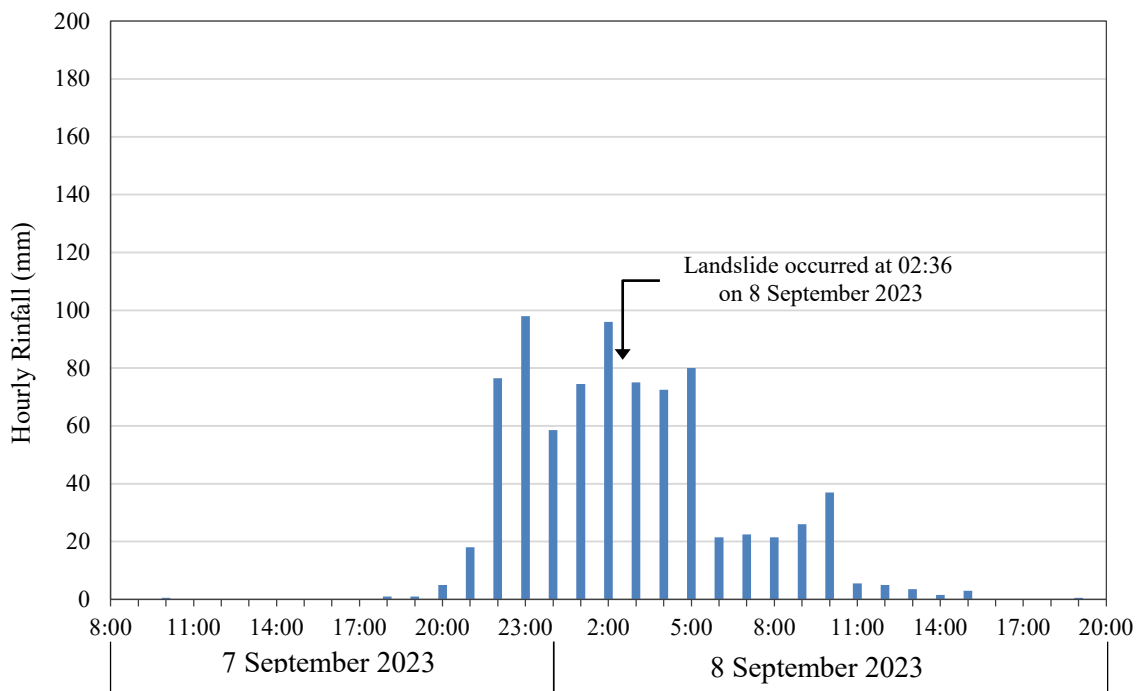
(b) Hourly rainfall recorded between 8:00 a.m. on 7 September 2023 and
8:00 p.m. on 8 September 2023 based on clock-hour rainfall data

**Figure 7.1   Daily and Hourly Rainfall Recorded at GEO Raingauge No. H19 for the
Landslide on 8 September 2023**

Table 7.1   Maximum Rolling Rainfall at GEO Raingauge No. H19 for Selected Durations Preceding the 8 September 2023 Incident and the Estimated Return Periods

Duration	Maximum Rolling Rainfall (mm) [1][2]	End of Period [3]	Estimated Return Period (years) [4]
5 Minutes	17.5	0:00 a.m. on 8 September 2023	15
15 Minutes	45.5	0:05 a.m. on 8 September 2023	23
30 Minutes	70.5	10:20 p.m. on 7 September 2023	15
1 Hour	123.5	10:30 p.m. on 7 September 2023	39
2 Hours	197.5	1:45 a.m. on 8 September 2023	107
4 Hours	344.5	1:30 a.m. on 8 September 2023	> 500
12 Hours	462.5	2:35 a.m. on 8 September 2023	238
24 Hours	465.0	2:35 a.m. on 8 September 2023	49
48 Hours	465.0	2:35 a.m. on 8 September 2023	10
4 Days	466.0	2:35 a.m. on 8 September 2023	4
7 Days	632.0	2:35 a.m. on 8 September 2023	8
15 Days	646.0	2:35 a.m. on 8 September 2023	4
31 Days	750.0	2:35 a.m. on 8 September 2023	2

Notes: (1) Maximum rolling rainfall was calculated from 5-minute rainfall data.
(2) GEO raingauge No. H19 located at Salesian English School, 16 Chai Wan Road, Shau Kei Wan, about 500 m northeast of the landslide site.
(3) The landslide occurred at 2:36 a.m. on 8 September 2023.
(4) The return periods were estimated based on the method described by Chan & Chu (2024).
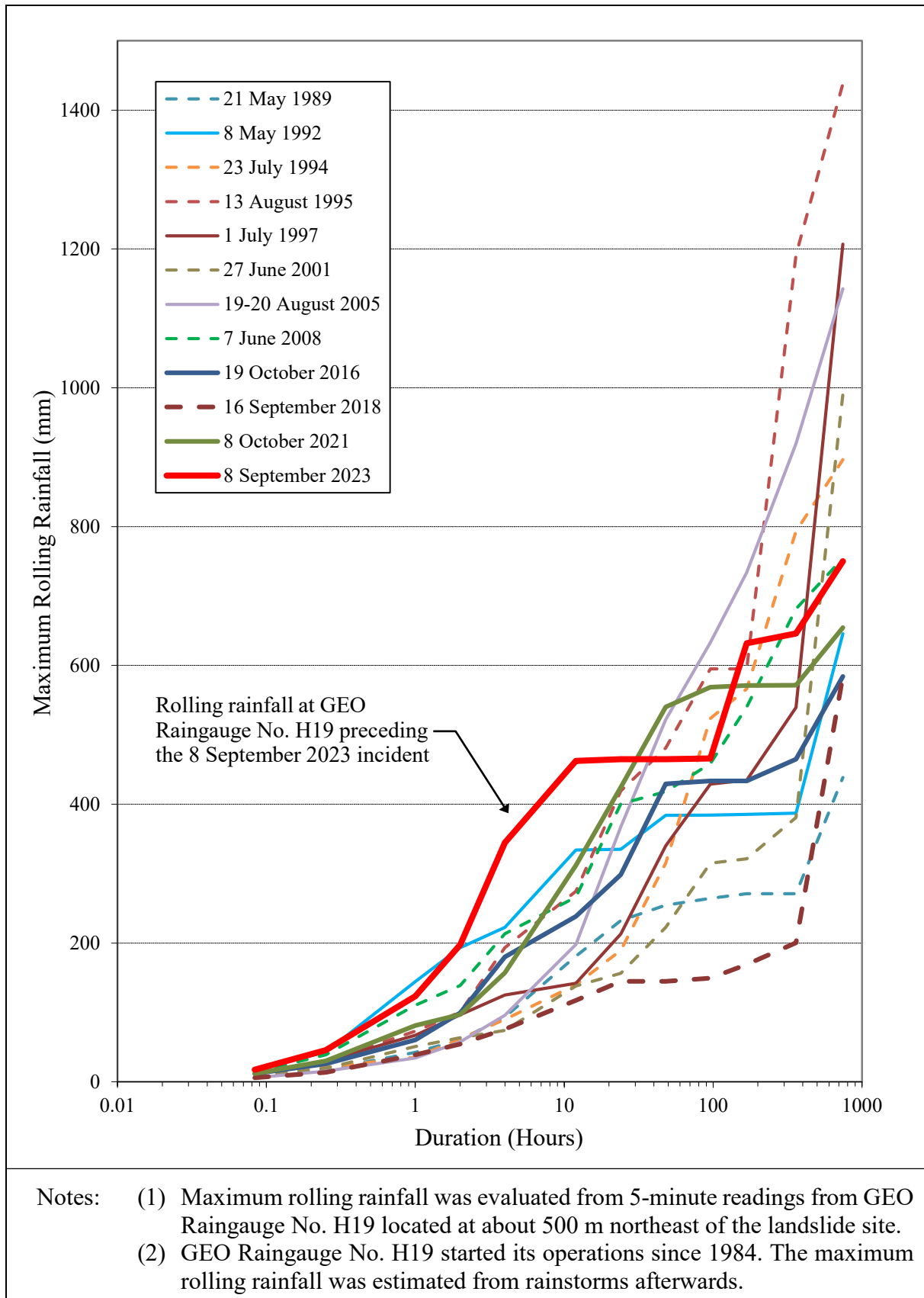
Figure 7.2 Maximum Rolling Rainfall Preceding the Landslides and Previous Major Rainstorms at GEO Raingauge No. H19

8 Engineering Analyses

8.1 General

Direct infiltration of rainwater into the natural hillside and seepage of channel runoff through the relatively permeable open rock joints could lead to a build-up of transient cleft water pressure in the sheeting joint that formed the basal failure plane of the lower landslide. To understand the hydrological condition at the time of failure, the channel runoff in the rocky stream course adjacent to the location of the lower landslide and the capacity of the drainage outlet pipes underneath gabion wall ND9 were first estimated. The characteristics of the sheeting joint were assessed using field measurements and empirical correlations. Numerical seepage and slope stability analyses were performed to assist in the diagnosis of the cause and mechanism of the failure. Then, three-dimensional debris mobility analyses were carried out to back-analyse the movement of the landslide debris and determine the probable rheological parameters of the landslide debris.

8.2 Channel Runoff in Rocky Stream Course

8.2.1 Estimation of Channel Runoff

Excessive surface water from overflow weirs W4 and W5, together with surface runoff collected from the catchment below the catchwater, can flow into the rocky stream course adjacent to the landslide location (Figure 8.1).

The channel runoff in the rocky stream course has been estimated for the actual site condition and also two other hypothetical scenarios:

(a) Overflow weirs W1, W3 and W5 were not modified in around 1995, and

(b) The catchwater was not constructed before 1945, while all else remains the same.

In the actual site condition, the estimated channel runoff in the rocky stream course was about 100 m^3/min at the time of the landslide. The channel runoff would have been 75 m^3/min if the catchwater had not been constructed before 1945 and 90 m^3/min if the weirs had not been enlarged around 1995. These results indicate that the catchwater and the subsequent modification works led to more runoff reaching the rocky stream course adjacent to the landslide location.

Details of the assessment are given in Appendix C.
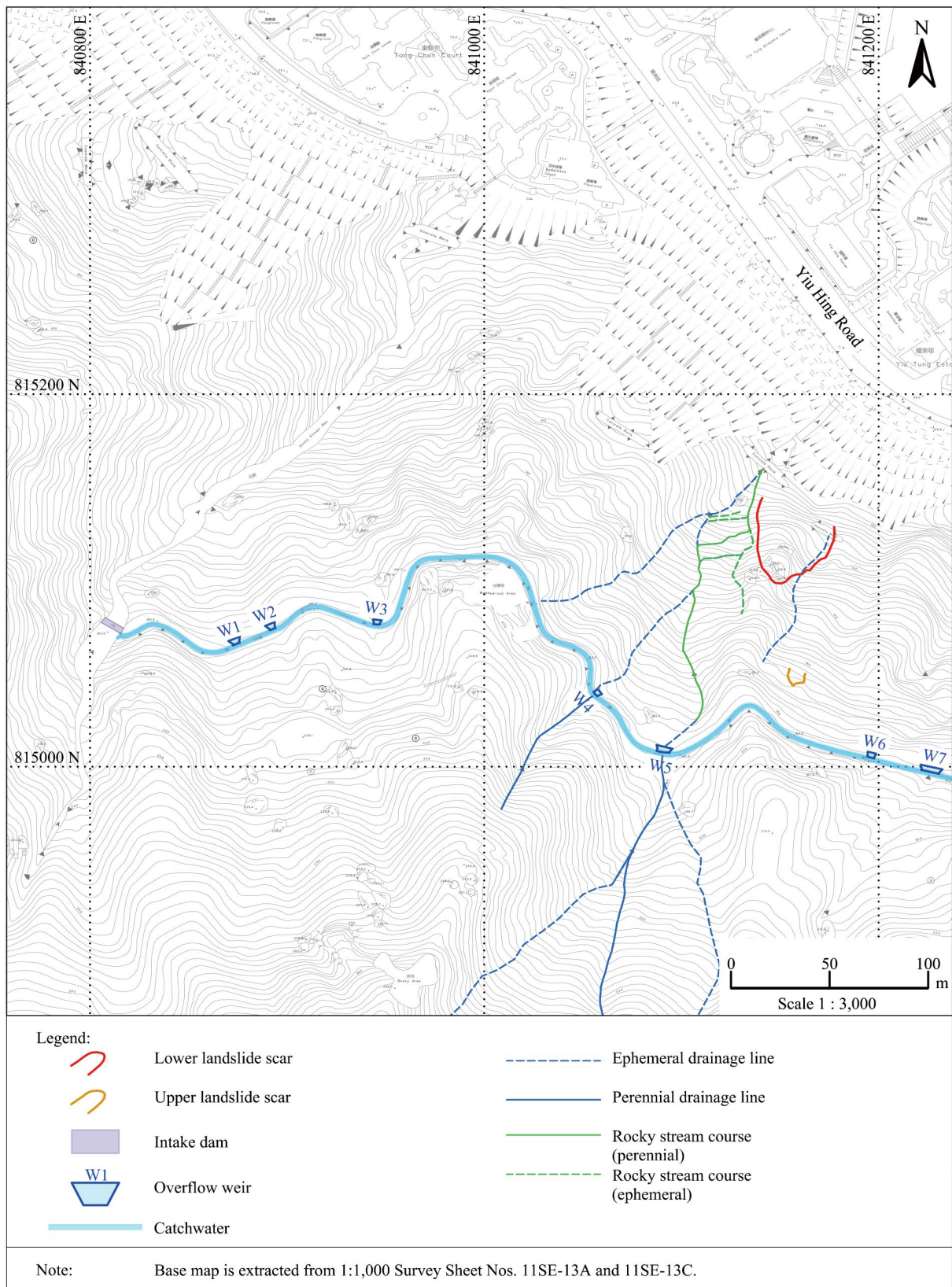
Figure 8.1   Layout Plan of the Catchwater Section

8.2.2 Drainage Capacity of Outlet Pipes underneath Gabion Wall ND9

Three 675 mm-diameter drainage outlet pipes underneath gabion wall ND9 are constructed to intercept the channel runoff in the rocky stream course and drain the runoff to the stormwater drainage system beneath Yiu Tung Estate through a 2 m-wide cascade between the cut slopes (Section 2). Table 8.1 provides the theoretical capacity of the drainage outlet pipes underneath gabion wall ND9.

Table 8.1   Flow Capacity of the Drainage Outlet Pipe

Diameter (mm)	Gradient (m/m)	Flow velocity (m/s)	Flow capacity (m^3/min)
675	0.466	18	386

Note: Based on Colebrook-White equation, the theoretical discharge capacity of three drainage outlet pipes is about 1,158 m^3/min.

The theoretical capacity of these three outlet pipes is about 1,158 m^3/min, which appears adequate to convey the estimated runoff from the rocky stream course (100 m^3/min) during the severe rainstorm on 7 to 8 September 2023. However, the landslide debris wholly blocked one of the drainage pipes on the left and partially blocked the inlets of the other two (Section 6) so the actual drainage capacity would have decreased considerably after the landslide.

Despite the partial blockage of the pipes after the incident, the post-landslide inspections revealed that water was still flowing from two 675 mm-diameter drainage outlet pipes. Additionally, there were no signs of channel runoff spreading around the partially damaged gabion wall ND9. Water was observed flowing continuously along the cascade below the gabion wall until it reached the blocked location, where it overflowed onto the cut slopes (Section 6). These observations suggest no significant spillage issues around gabion wall ND9 during the severe rainstorm.

Given the lack of evidence for significant spillage and erosion around the gabion wall, it is unlikely that soil erosion due to spillage from gabion wall ND9 contributed to the lower landslide.

8.3   Groundwater Response

8.3.1   Direct Infiltration and Water Ingress from Rocky Stream Course

The post-landslide inspections identified two possible sources for the development of transient cleft water pressure in the sheeting joint that formed the basal failure plane at the lower landslide:

(a) Direct infiltration of rainwater into the natural hillside above (i.e. extending to the catchwater at 70 m upslope of the lower landslide scar) and within the lower source area, and

(b) Water ingress from the rocky stream course along the western flank through the relatively permeable open rock joints.

Numerical analyses using the computer program SEEP/W were carried out to evaluate the possible range of cleft water pressure developed in the sheeting point at the time of failure under these conditions.

8.3.2 Two-dimensional Seepage Analyses

Two sets of two-dimensional numerical seepage analyses were carried out to simulate the effects of direct infiltration of rainwater from the ground surface (Figure 8.2(a)) and water ingress from the rocky stream course into the sheeting joint (Figure 8.3(a)). The hydraulic material properties used in the analyses are summarised in Table 8.2 below.

Table 8.2   Hydraulic Material Properties

Material	Saturated Coefficient of Permeability (k_s)	Soil Type	Permeability Model	Considered in Analysis
Corestone-rich CDG	1×10^{-5} m/s	Silty sand	Saturated/ unsaturated	Direct infiltration of rainwater
Coreslab	1×10^{-7} m/s	Rock		
Bedrock	1×10^{-8} m/s	-	Saturated only	
Seepage zone (open rock joints)	1×10^{-5} m/s	-		Water ingress from rocky stream course
Sheeting joint	1×10^{-6} m/s	-		

Note: The default soil types in SEEP/W were used to evaluate the soil water characteristic curves. The permeability function based on Fredlund & Xing (1994) was used.
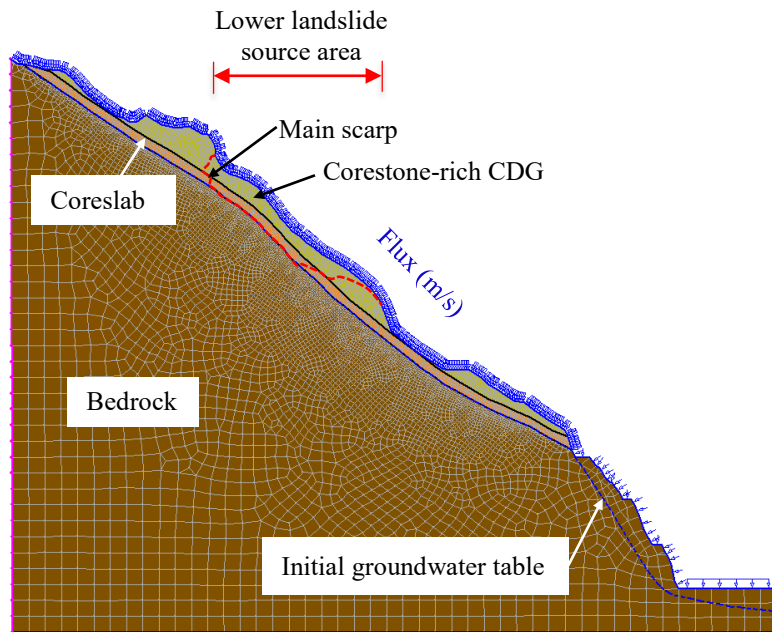
(a) Model Setup
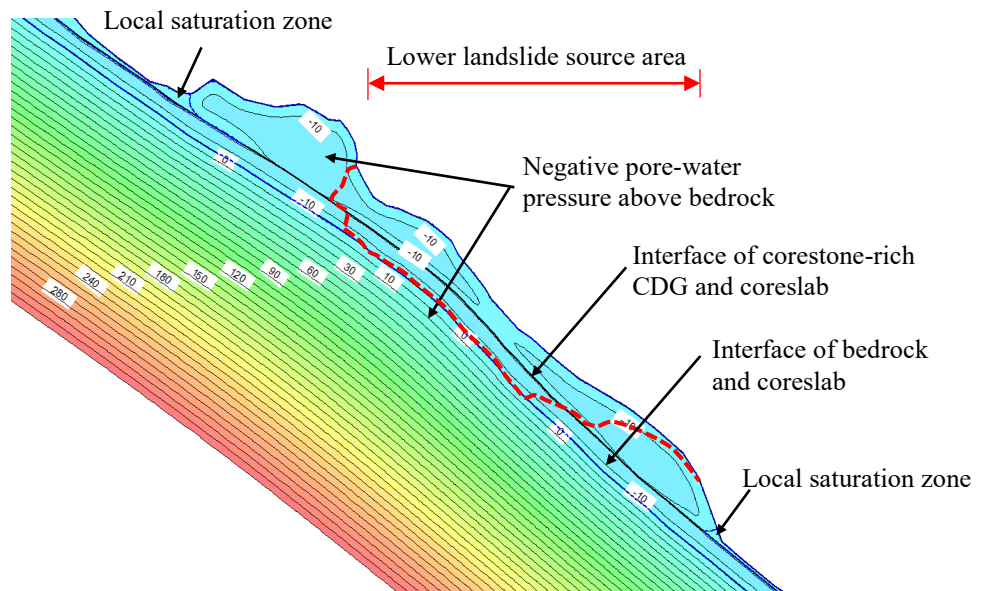
(b) Pore-water Pressure Distribution at the Time of Failure

Figure 8.2   Seepage Analysis of Direct Infiltration of Rainwater

(a) Model Setup

Specified water head

Impermeable boundary

Drainage boundary

Higher cleft water pressure in the central and lower portion of the exposed sheeting joint

Lower cleft water pressure in the sheeting joint below the unfailed in-situ material

● 0 kPa   ● < 2.5 kPa   ● 2.5 - 5 kPa   ● 5 - 7.5 kPa
● 7.5 - 10 kPa   ● 10 - 15 kPa   ● 15 - 20 kPa   ● 20 - 25 kPa

(b) Cleft Water Pressure Distribution in the Sheeting Joint
(1-m water head in secondary stream)

Notes: (1) Only the seepage zone and the landslide source area are considered in this set of seepage analyses.

(2) An assumed water head is specified along the secondary stream to simulate seepage into the sheeting joint through the open rock joints (seepage zone). Free drainage is assumed at the drainage boundary.

Legend:

―――― Perennial drainage line   – – – Ephemeral drainage line

―――― Perennial rocky stream course   – – – Ephemeral rocky stream course (secondary stream)

Seepage zone (open rock joint)

Sheeting joint

Sheeting joint below unfailed in-situ material

Figure 8.3   Seepage Analysis of Water Ingress from Secondary Stream

Given the time-dependent nature of the case, a transient two-dimensional seepage analysis was carried out to assess the possible build-up of cleft water pressure in the sheeting joint due to direct infiltration of rainwater. In addition to the severe rainstorm on 7 to 8 September 2023, the seepage analysis also took into account the heavy rainstorm brought by Typhoon Saola on 1 to 2 September 2023. At the start of the analysis, the groundwater table was assumed to lie at the bedrock surface, and an initial matric suction of 20 kPa was assigned to the materials above bedrock. Figure 8.2b shows the cleft water pressure distribution in the slope at the time of the landslide. The result indicates that only limited cleft water pressure had developed in the sheeting joint by direct infiltration. This means that infiltration alone was not the main source of water contributing to the build-up of cleft water pressure.

Another set of steady two-dimensional seepage analyses were carried out to evaluate the contribution of water ingress from the rocky stream course to the development of cleft water pressure in the sheeting joint. In the numerical model, runoff flowing in the ephemeral rocky stream course (secondary stream) adjacent to the landslide location is modelled to seep into the sheeting joint through the open rock joints (a seepage zone). The water head in the secondary stream is assumed to be 0.5 m, 1 m and 1.5 m. In the numerical model, the sheeting joint is assumed to extend below the unfailed in-situ material by projection using the dip angle and dip direction of the exposed portion. Figure 8.3b shows the cleft water pressure in the sheeting joint for a 1.0 m water head in the ephemeral rocky stream course at the time of the failure. The result shows that cleft water pressure could build up in the sheeting joint in this condition, with the highest values (up to 30 kPa) concentrated in the central and lower portion of the exposed sheeting joint after the landslide. This cleft water pressure distribution was subsequently used to back-analyse the stability of the hillside (Section 8.5).

Overall, the results of the two-dimensional seepage analyses, together with the post-landslide observations, indicate that the infiltration of rainwater and water ingress from the rocky stream course were the probable sources of the transient cleft water pressure in the sheeting joint.

8.3.3 Three-dimensional Seepage Analyses

Given the combined effect of direct infiltration and contribution of water ingress from the rocky stream course to the development of cleft water pressure in the sheeting joint, a set of transient three-dimensional seepage analyses using the three-dimensional numerical program PLAXIS 3D were conducted to assess the possible build-up of cleft water pressure in the sheeting joint at the time of failure. The analyses considered both the direct infiltration of rainwater and the water ingress from the rocky stream course.

In the numerical analyses, the boundary conditions and hydraulic material properties were the same as those in the two-dimensional analyses, except that the water head in the secondary stream varied from 0.1 m to 1 m, correlating to the rainfall intensities of rainstorms on 1 to 2 September 2023 and 7 to 8 September 2023. Figure 8.4 shows the cleft water pressure in the sheeting joint for varying water heads in the ephemeral rocky stream course at the time of the failure. The results indicate a similar cleft water pressure distribution, with the highest values (up to about 34 kPa) concentrated in the central and lower portion of the exposed sheeting joint. This cleft water pressure distribution was also used for the back-analyse of the stability of the hillside (Section 8.5).
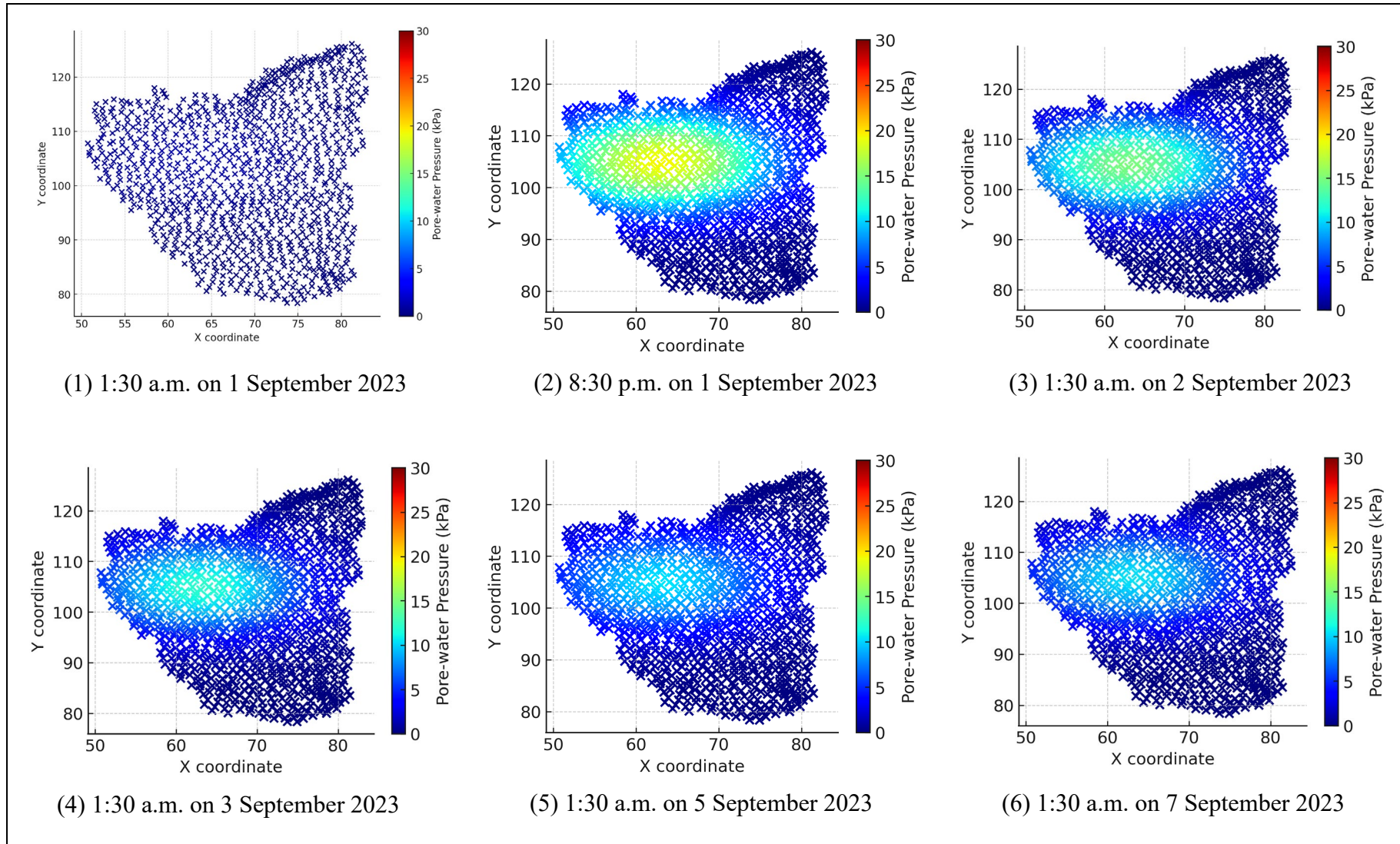
(1) 1:30 a.m. on 1 September 2023

(2) 8:30 p.m. on 1 September 2023

(3) 1:30 a.m. on 2 September 2023

(4) 1:30 a.m. on 3 September 2023

(5) 1:30 a.m. on 5 September 2023

(6) 1:30 a.m. on 7 September 2023

Figure 8.4   Development of Cleft Water Pressures in the Sheeting Joint for Varying Water Heads (Sheet 1 of 2)

(7) 9:30 p.m. on 7 September 2023

(8) 10:30 p.m. on 7 September 2023

(9) 11:30 p.m. on 7 September 2023

(10) 0:30 a.m. on 8 September 2023

(11) 1:30 a.m. on 8 September 2023

(12) 2:30 a.m. on 8 September 2023
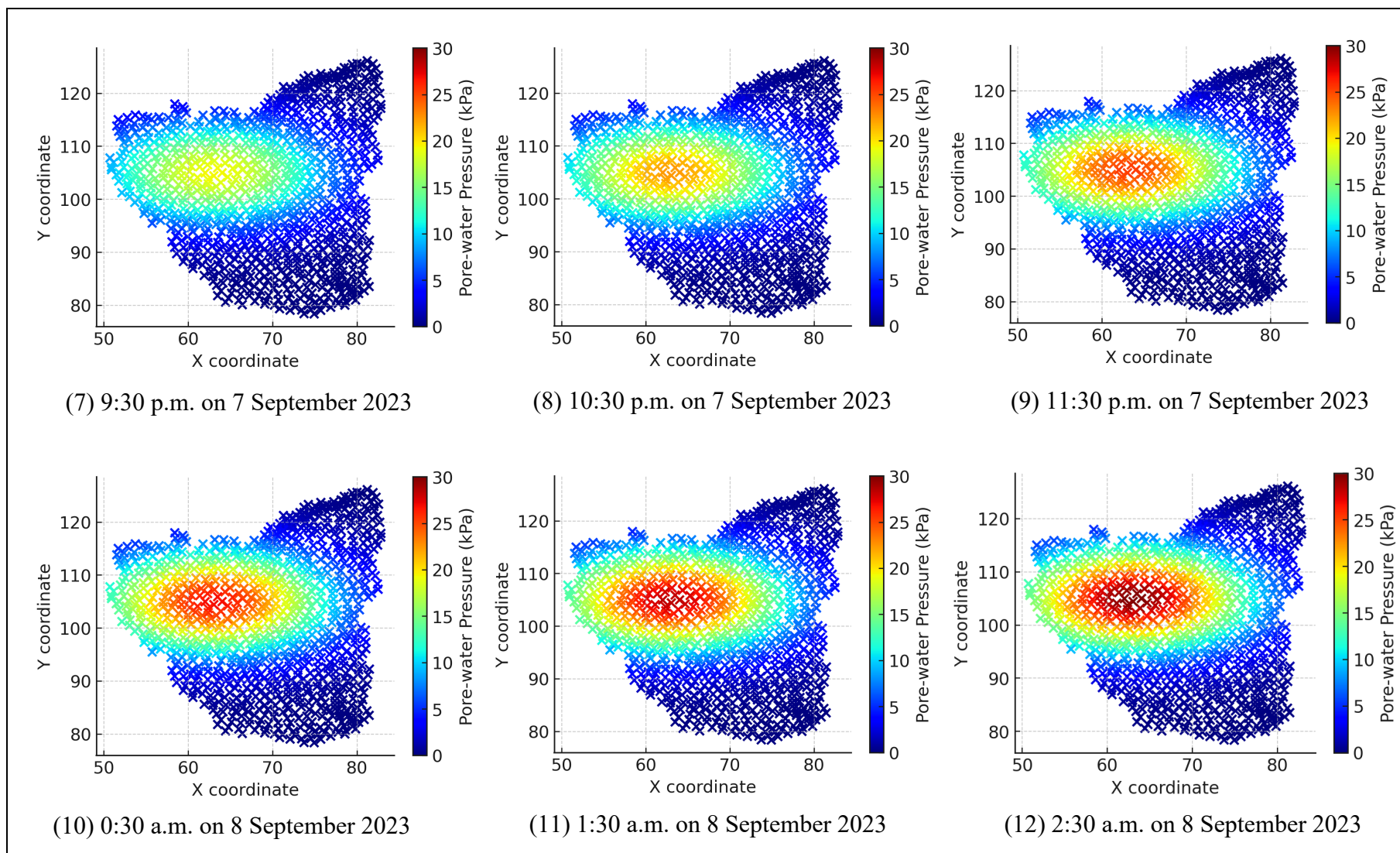
Figure 8.4   Development of Cleft Water Pressures in the Sheeting Joint for Varying Water Heads (Sheet 2 of 2)

In summary, the results of the analyses confirm that infiltration of rainwater and water ingress from the rocky stream course were the probable sources of the transient cleft water pressure in the sheeting joint.

8.4 Sheeting Joint Characteristics

The basal failure plane of the lower landslide is formed by a persistent, locally stepped, undulating to planar sheeting joint. As mentioned by Hencher (1987), sheeting joints are normally formed sub-parallel to the ground surface by tensile stresses due to unloading. This phenomenon is a common feature in the granitic terrain of Hong Kong and has been extensively studied locally and abroad. Slope stability analysis requires knowledge of the shearing resistance along potential failure planes, and in this case, the persistent sheeting joint exposed after the failure. Barton (1973) introduced the concepts of joint roughness coefficient (JRC) and joint compressive strength (JCS) to facilitate the assessment of joint roughness and shear strength in rock engineering. This was further refined through empirical means into Equation 8.1, which assumes that the joint is predominantly rock-on-rock contact with negligible infilling (Barton & Choubey, 1977; Barton et al, 2023). This equation assumes that the mobilised shear strength is purely friction, that is, no cementation or cohesion on the joint surface.

$$\frac{\tau}{\sigma'_n} \ = \ tan\varphi' \ = \ tan\left[JRC\,log_{10}\left(\frac{JCS}{\sigma'_n}\right) + \varphi_r\right] \quad\ldots\ldots\ldots\ldots\ldots\ldots\ldots\ldots\ldots\ldots(8.1)$$

where

	φ'	=	peak friction angle (°)
	τ	=	peak shear strength (kPa)
	σ'_n	=	effective normal stress (kPa)
	JRC	=	joint roughness coefficient (dimensionless)
	JCS	=	joint compressive strength (kPa)
	φ_r	=	residual friction angle (°)

Field measurements of surface roughness have been made on the accessible portion of the exposed sheeting joint in the lower landslide source area. The measurements were made using a 100-mm long profilometer (Barton comb) (Figure 8.5). The corresponding JRC was determined based on a visual comparison with typical roughness profiles given in Barton & Choubey (1977) and the results ranged from 6 to 14. Given the scale of the exposed sheeting joint, a number of 5-m and 10-m long profiles were also extracted from a digital photogrammetric model of the landslide scar for further assessment of joint roughness and JRC (Figure 8.6) with reference to Du et al (2022). The JRC determined in this way ranged from 4 to 20. Records of surface roughness measurement and JRC are enclosed in Appendix D.

Figure 8.5   Field Measurements of Surface Roughness Using a Profilometer

(a) 5-m Profile Lines	(b) 10-m Profile Lines
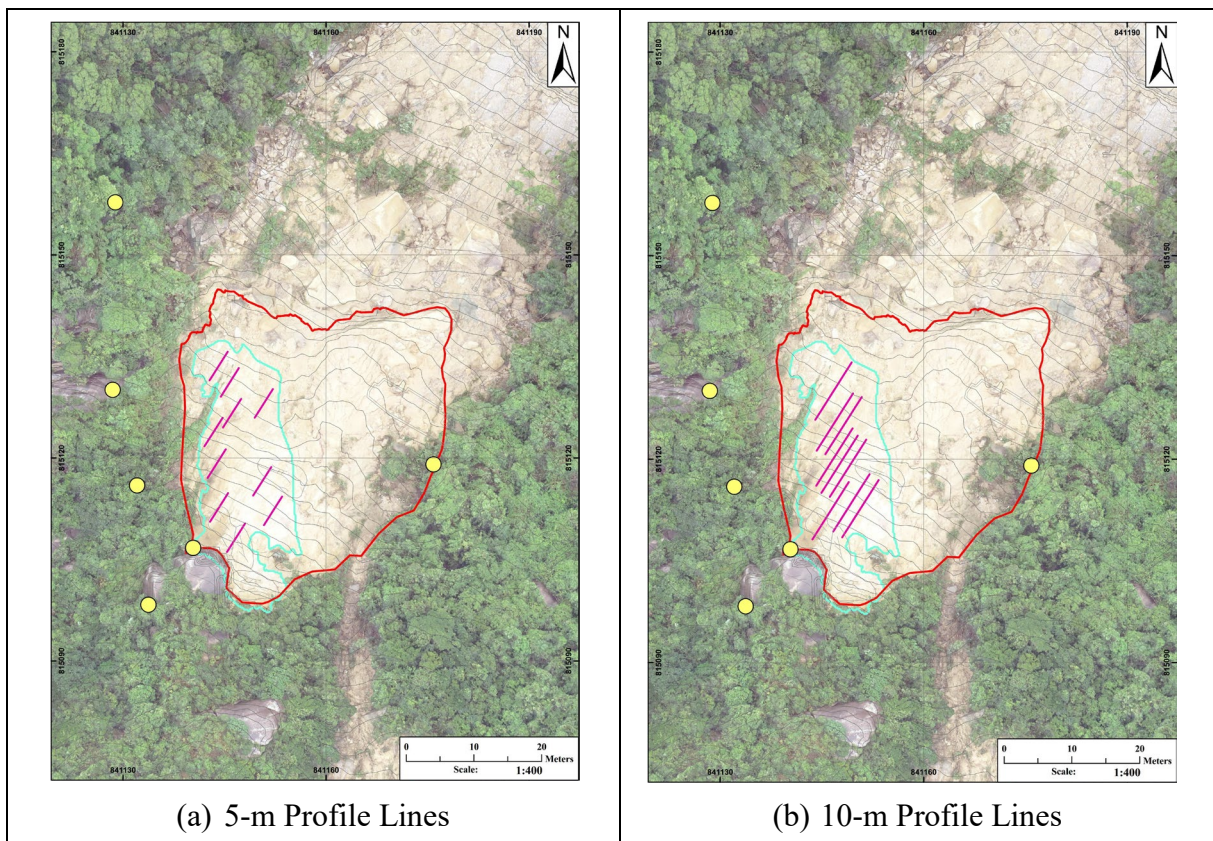
Figure 8.6   Profile Lines in Digital Photogrammetric Model

The JCS was determined by collecting Schmidt hammer readings (Type N) on rock outcrops and tors to assess the strength of the weathered rock joint, as well as on fresh drill cores to assess the strength of unweathered intact rock (Figure 8.7). The Type N hammer readings (R_N) were then converted to Type L readings (R_L) (Look, 2014) to obtain the JCS based on the graphical method proposed by Deere & Miller (1966). Table 8.3 summarises the JRC and hammer readings (measured and converted) on both weathered and unweathered rocks.

Figure 8.7   Schmidt Hammer Testing on a Tor

To use Equation 8.1, the effective normal overburden pressure (σ'_n) and the residual friction angle (φ_r) were also required. The value of σ'_n was estimated based on the thickness and unit weight of the overburden materials as well as the estimated cleft water pressures in the sheeting joint at the time of failure (Section 8.3.2). The residual friction angle (φ_r) was derived using Type N Schmidt hammer readings and a basic friction angle (φ_b) using Equation 8.2 given by Barton & Choubey (1977):

$$\varphi_r = \varphi_b - 20° + 20\frac{r}{R} \quad\dots\dots\dots\dots\dots\dots\dots\dots\dots\dots\dots(8.2)$$

where
φ_b = basic friction angle (°)
r = Schmidt hammer readings on weathered joint (= $R_{N\text{-JOINT}}$)
R = Schmidt hammer readings on unweathered rock surfaces (= $R_{N\text{-CORE}}$)

Table 8.3   Summary of Measured Joint Roughness Coefficients and Hammer Readings

Parameter	Measurement Counts	Min.	Lower Quartile	Mean	Median	Upper Quartile	Max.
JRC (100-mm profiles)	8	6	- [1]				14
JRC (5-m profiles)	10	4.2	6.1	9.7	7.6	13.2	18.5
JRC (10-m profiles)	9	5.3	5.6	10.6	7.7	12.9	20.9
$R_{N\text{-JOINT}}$ (outcrops and tors)	30	16	30	33.5	35	40	52
$R_{N\text{-CORE}}$ (drill cores)	5	51	- [1]				53
$R_{L\text{-JOINT}}$ [2]	30	11.4	20.9	23.3	24.3	27.7	35.8

Notes: (1) No statistical calculations were done due to small sample size.

            (2) $R_{L\text{-JOINT}}$ is converted from $R_{N\text{-JOINT}}$ using the correlation by Look (2014):

$$R_L = 0.605 + 0.677 \times R_N .$$

Table 8.4 summarises the parameters required for the estimation of the shearing resistance of the sheeting joint. The peak friction angle (φ') of the sheeting joint was estimated to range between 48° and 72° with a most probable value of 54°. However, as described in Section 6.3, infill materials comprising silty sand (CDG) and clay were found in patches across the basal failure plane, and some would have been washed away after the landslide during the severe rainstorm. The presence of infill was expected to reduce the shearing resistance between the coreslab and the sheeting joint. For this reason, the actual friction angle should be lower than 54°, which is only applicable to sliding between clean rock surfaces.

Table 8.4   Summary of Parameters for Estimating the Shearing Resistance of the Sheeting Joint

Parameter	Unit	Range of Values	Selected Value [1]
JRC	-	6 - 14	8
JCS	MPa	38 - 42	40
σ'_n	kPa	70 - 100	85
γ_{CDG}	kN/m³	-	20
γ_{MDG}	kN/m³	-	22
φ_b [2]	°	35 - 42	40
φ_r	°	32 - 35	33

Notes: (1)   The selected values incorporate engineering geological judgement.

(2)   The listed values were obtained from a study of North Point granites (Hencher & Richards, 1982) and a similar study on granites in Balasore, India (Ram & Basi, 2019).

8.5 Slope Stability Back-analyses

8.5.1 Objectives and Approach

Given the geological settings of the site and the occurrence of the lower landslide during the severe rainstorm, transient cleft water pressure was likely to have developed in the sheeting joint at the time of the failure. Post-landslide inspections (Section 6) and seepage analyses (Section 8.3) indicate that the infiltration of rainwater and water ingress from the rocky stream course were the probable sources of the transient cleft water pressure in the sheeting joint. This pressure would reduce the shearing resistance of the groundmass above the joint, eventually triggering the lower landslide.

The primary objectives of the stability analyses are twofold:

(a) To back-calculate the likely range of the cleft water pressure development in the sheeting joint.

(b) To determine the operative shear strength parameters of the sheeting joint at the time of failure.

To achieve these objectives, the analyses adopted the three-dimensional limit equilibrium method using the method of columns. The analyses considered both force and moment equilibrium (Morgenstern - Price approach) of each imaginary 'column' of the groundmass, with plan dimensions of 0.5 m × 0.5 m. The computer program 'Slope3D' developed by Cheng & Yip (2007) was used to perform the calculations.

8.5.2 Model Setup and Input Parameters

Figure 8.8 shows the computation models used for the analyses. They were prepared with reference to the site geometry and geological condition as discussed in Section 6. The pre- and post-landslide slope profiles were prepared using terrain profile data obtained from the 2020 LiDAR survey data, along with photogrammetric and LiDAR data collected from the post-landslide UAV surveys.

The theoretical factors of safety (FOS) of the slope were computed using the cleft water pressures generated from the seepage analyses, with variations in the depth of flowing water in the secondary stream. The actual slip surface was determined from the post-landslide surveys.

Table 8.5 summarises the input parameters for the slope stability analyses.

(a) Pre-landslide Ground Profile

(b) Post-landslide Ground Profile
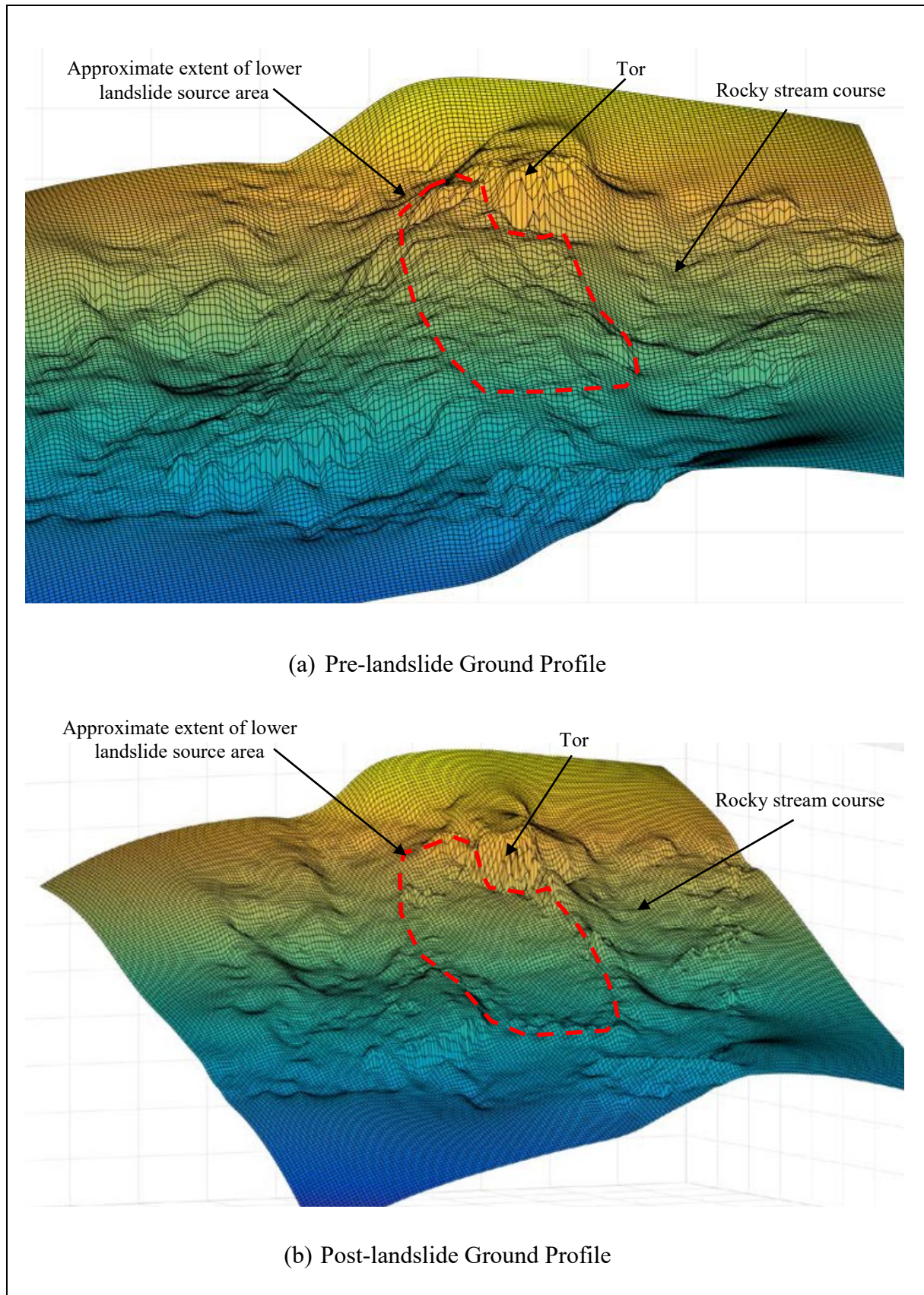
Figure 8.8   Computational Models used for Slope Stability Back-analyses

Table 8.5   Input Material Parameters for Slope Stability Back-analyses

Material Type	Bulk Unit Weight γ (kN/m³)	Cohesion c' (kPa)	Friction Angle ϕ' (°)
Corestone-rich CDG	20	10	40
Coreslab	22	15	50
Sheeting joint	22	0	Varied from 35 to 50

Note: In the absence of the site-specific data, the strength parameters of corestone-rich CDG were determined with reference to the typical values of in-situ CDG in Hong Kong (GEO, 2020).

8.5.3   Results

The results of the back-analyses are presented in Figure 8.9. The results indicate that for a 1-m depth of flowing water in the secondary stream, the combination of ϕ' = 40° to 45° and c' = 0 kPa together with a maximum cleft water pressure of about 30 kPa in the sheeting joint would have been sufficient for the failure to occur (i.e. FoS = 1). Similarly, for varying depths of flowing water in the secondary stream, the combination of ϕ' = 40° to 45° and c' = 0 kPa, along with a maximum cleft water pressure of about 34 kPa in the sheeting joint, would also have been sufficient for the failure to occur (i.e. FoS = 1). For comparison, Hencher & Richards (1982) reported that direct shear tests on sheeting joint samples of Hong Kong Granite in North Point yielded a friction angle of 40°.

Additionally, back-analyses of the landslide above Sai Wan Road revealed the operative shear strength parameters for sheeting joint (ϕ' = 40° to 45° and c' = 0 kPa) together with a maximum cleft water pressure of between 33 kPa and 43 kPa would also have been sufficient for the failure to occur (AECOM, 2018).

Derivation of the range of friction angle of sheeting joints from field measurements using the Barton and Choubey approach gave the most probable value of 54° (Section 8.4). This approach assumes that rock-to-rock contact exists over the entire failure surface and does not consider the strength and thickness of any joint infilling.

Overall, the back-calculated shear strength parameters (ϕ' = 40° to 45° and c' = 0 kPa) are considered credible and representative of the operational shear strength of the sheeting joint. These parameters are theoretically bounded between the friction angle deduced from direct shear tests (ϕ' = 40°) and the value from JRC assuming a clean interface (ϕ' = 54°).
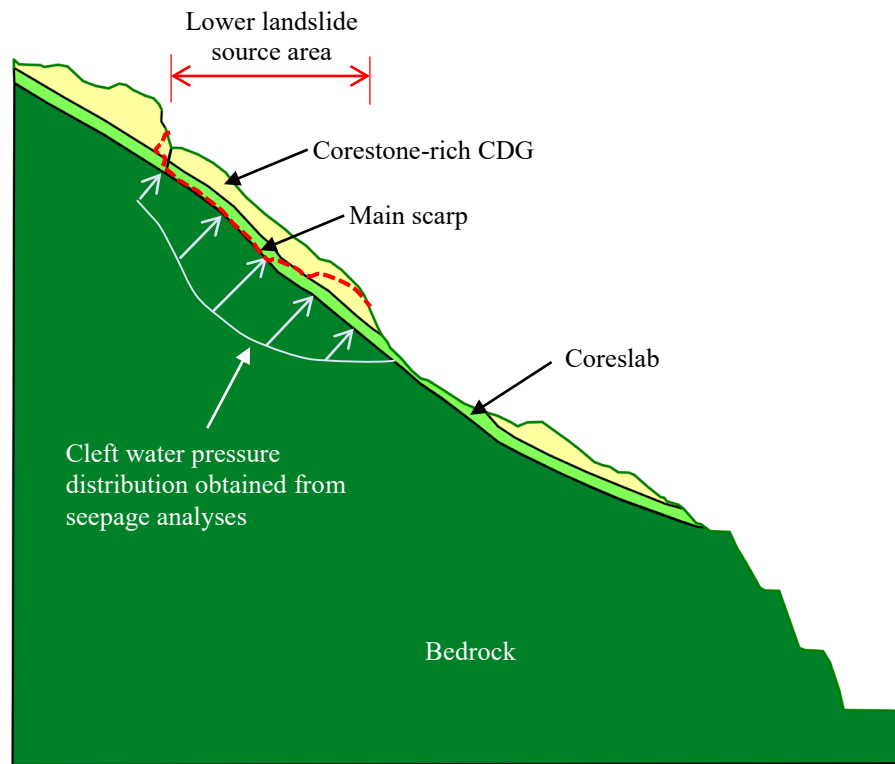
(a) Geological Model used for Stability Back-analyses
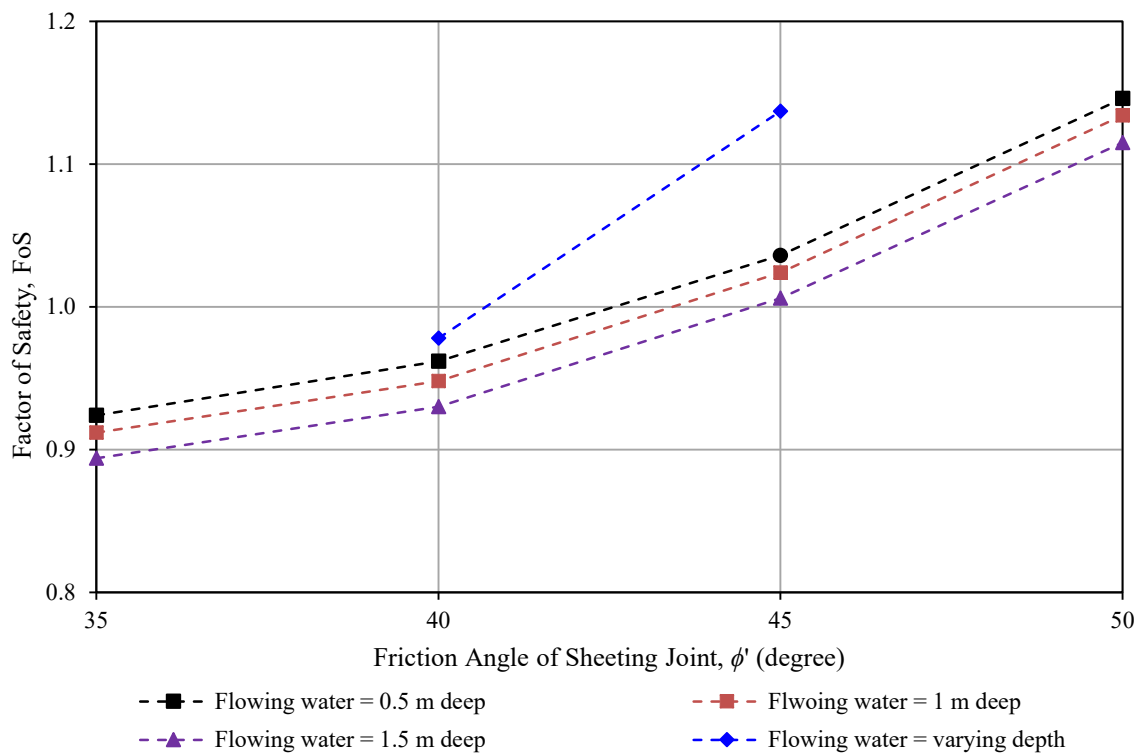
Figure 8.9   Results of Slope Stability Back-analyses

8.6 Debris Mobility Analyses

8.6.1 Debris Mobility

The lower landslide was a massive-scale structurally controlled translational rockslide on the natural hillslope. The landslide debris consisted of large numbers of rock blocks of different sizes, with the largest one measuring 11.5 m × 11 m × 5 m. The travel distance of the landslide debris, excluding the outwash, was about 150 m on plan, with about 40 m of the debris trails having an overall gradient of 15° or less. The travel angle measured from the crown of the lower landslide scar to the end of the debris trail was about 30°. The mobility of the landslide debris is less mobile comparing to other events observed in Hong Kong (Figure 8.10).

8.6.2 Objectives and Approach

The primary objectives of the comprehensive mobility analyses are to simulate the movement of the landslide debris and determine the probable apparent basal friction angle (ϕ_a) of the debris, which are essential for understanding the characteristics of this landslide event. The LPMit Consultants under Agreement No. CE 24/2018 (GE), Arup, conducted a comprehensive mobility analysis of the lower landslide for the GEO of the CEDD (Arup, 2024). They utilised the three-dimensional finite element program LS-DYNA to back-analyse the movement of the landslide debris using frictional rheology, as LS-DYNA can simulate large-scale deformation (Koo, 2017).

8.6.3 Model Setup and Input Parameters

In the LS-DYNA model, the topography was prepared using terrain profile data obtained from the 2020 LiDAR survey, along with photogrammetric and LiDAR data from the post-landslide UAV surveys. The thickness of the displaced materials within the landslide source was estimated by comparing the pre- and post-landslide topography with field measurements. Figure 8.11 shows the computational mesh model used for the analyses.

According to the post-landslide observations (Figure 8.12), about 75% (around 2,900 m³) of the total 3,900 m³ of debris material consisted of fallen rock blocks of varying sizes and shapes, originating from the coreslab as well as corestones and tors (Section 6.5). These large fallen rock blocks, deposited over the cut slopes and Yiu Hing Road, were generally cuboidal in shape, with dimensions ranging from 1 m to 11 m.

To represent the varying sizes and shapes of the fallen rock blocks in the mesh model, the following approach was adopted.

    (a) The first group consists of small rock blocks (1 m × 1 m × 1 m), representing the corestones from the CDG layer and fragments of the coreslab within the landslide source.

    (b) The second group consists of medium-sized rock blocks (2 m to 8 m), representing the larger corestones within the landslide source.
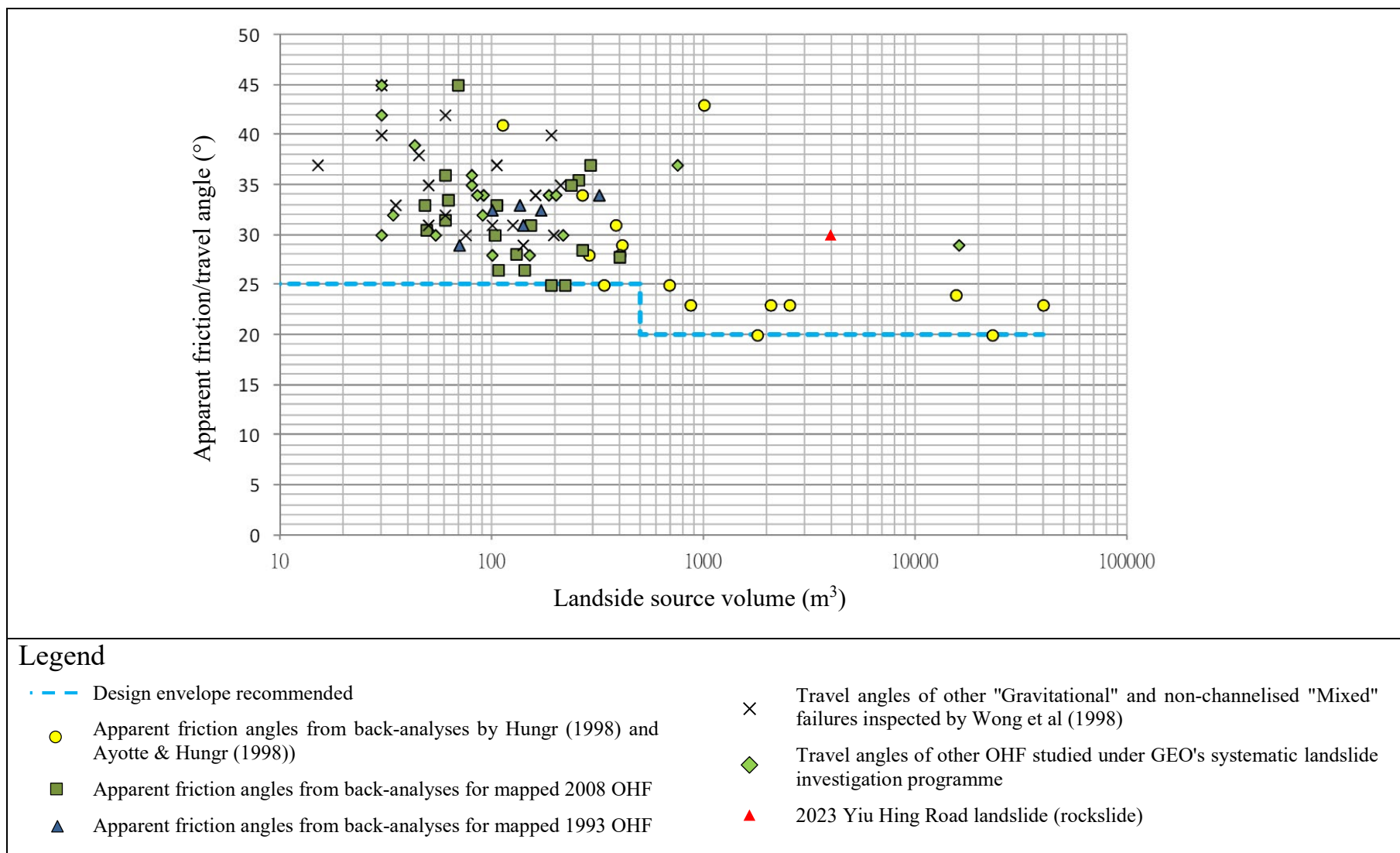
Figure 8.10   Data on Debris Mobility for Open Hillslope Failures of Different Scales (Extracted from GEO (2023))
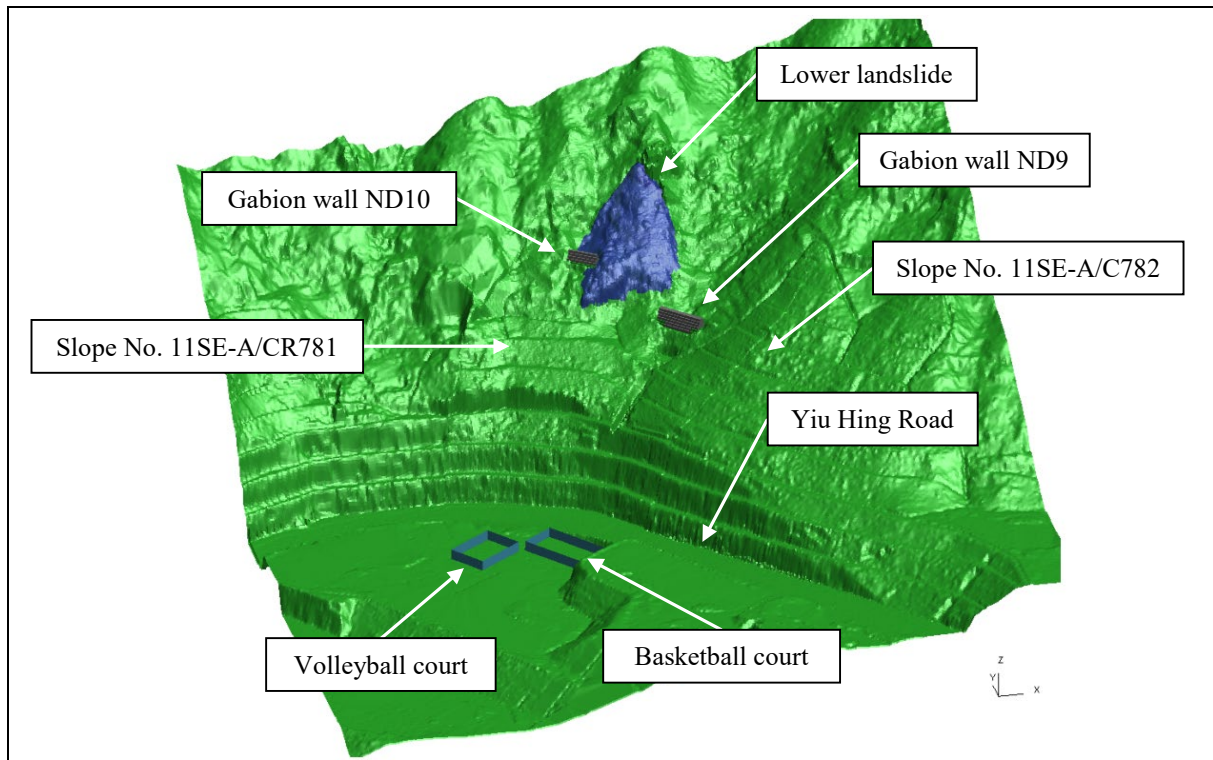
Figure 8.11   Model used for Debris Mobility Analyses
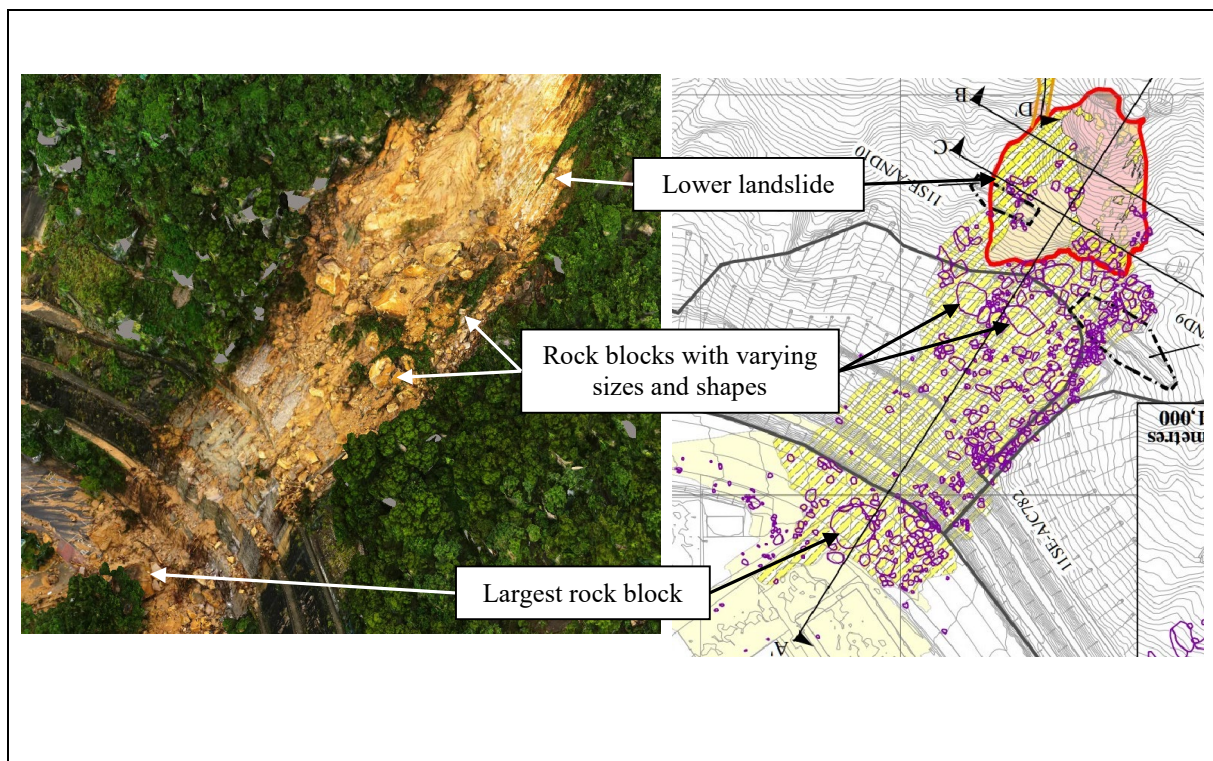
Figure 8.12   Fallen Rock Blocks of Varying Sizes and Shapes Deposited over Slope Nos. 11SE-A/CR781 and 11SE-A/C782 and Yiu Hing Road

(c) The third group is the largest rock block (11.5 m × 11 m × 5 m), representing the largest tor that fell onto Yiu Hing Road.

Figure 8.13 illustrates the initial state of the LS-DNYA simulation. The analyses employed the Arbitrary Lagrangian-Eulerian (ALE) method to model the soil debris surrounding the rock blocks. This approach effectively captured the significant deformation during the landslide process. The Drucker-Prager yield criterion was utilised to model the debris mass, and the input parameters derived following the procedure described in Koo (2017). An internal friction angle (ϕ_i) of 38° and an apparent basal friction angle (ϕ_a) of 28° were adopted for the simulation. It is worthwhile to note that the simulation results are not sensitive to the values of shear modulus, bulk modulus and Poisson's ratio (Koo, 2017).
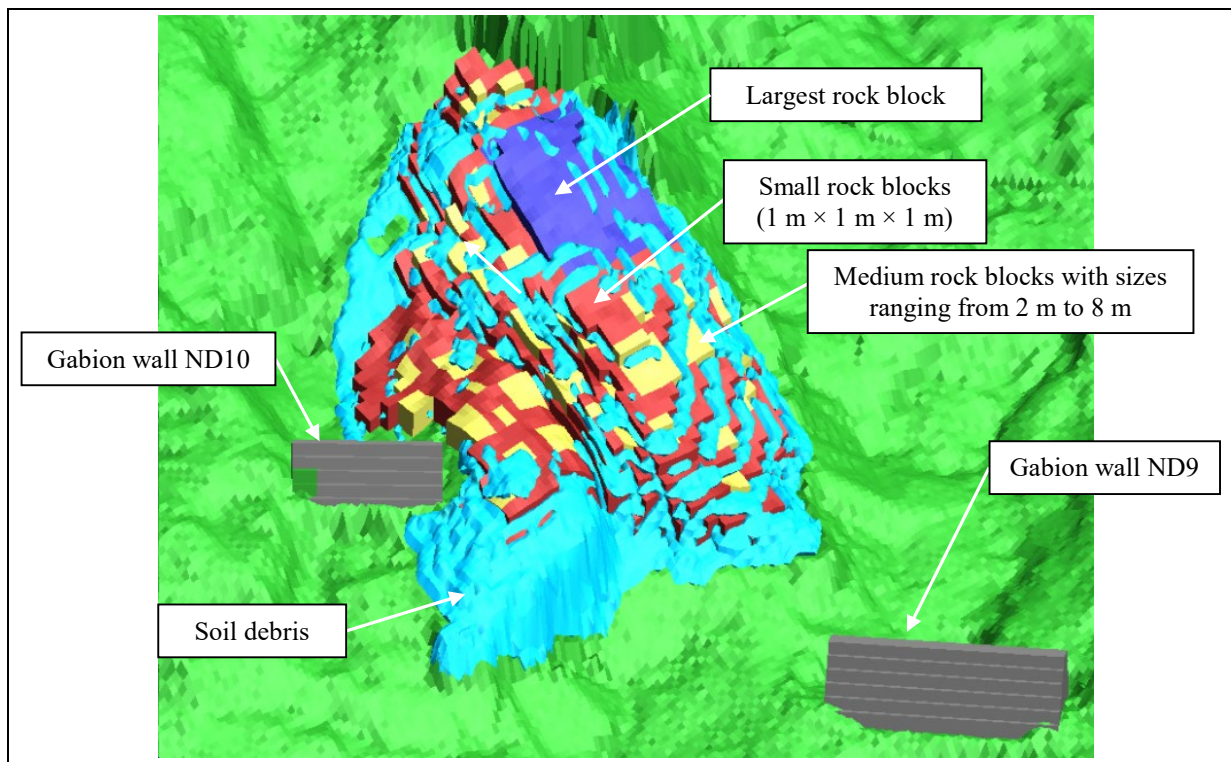
Figure 8.13   Initial State of LY-DYNA Simulation

In addition, it is important to note that the analyses only considered frictional contacts and did not consider other mechanisms during the landslide process, such as rock fracturing and cushioning effects from the ground. To account for a reasonable energy loss during the process, a global coefficient of restitution of 0.1 was set for all contacts among rock blocks, ground, and gabion walls.

Table 8.6 summarises the parameters used for the debris mobility analyses.

Table 8.6   Input Parameters for Debris Mobility Analyses

Material Property	Soil Debris	Rock Blocks	Gabion Wall	Topography
Material model	Soil and Foam	Rigid	Rigid	Rigid
Bulk density (kg/m^3)	2,100	2,650	2,250 [1]	2,100
Poisson's ratio, v	0.3	-	-	-
Shear modulus, G (GPa)	10	-	-	-
Internal friction angle, ϕ_i (^{o})	38	-	-	-
Apparent basal friction angle, ϕ_a (^{o})	28	-	-	-

Note: (1) The gabion rock fill typically consists of quarried or selected stone, with a bulk density of about 2,250 kg/m^3.

8.6.4   Simulation and Validation of Debris Mobility

Figure 8.14 depicts the simulated movement of the landslide debris over time, from the onset of the landslide ($t = 0$ s) to the final deposition state ($t = 30$ s). The figure illustrates that the majority of the landslide debris reached its final deposition state by $t = 25$ s. The LS-DYNA simulation, enclosed in Appendix E, effectively captures several key features of the landslide event (Figure 8.15), including:

(a) The final deposition of boulders and debris on the natural hillslope and cut slopes matched reasonably well with field observations.

(b) A significant amount of debris and rock blocks were deposited over the cut slopes.

(c) The cascade between the cut slopes was filled with soil debris and rock blocks.

(d) The landslide debris destroyed gabion wall ND10 and partially damaged gabion wall ND9 near the western flank.

(e) The debris deposition on Yiu Hing Road, including some reaching the basketball and volleyball courts.

(f) The largest rock block's deposition position matched its actual position on site.

$t = 0$ s

$t = 2$ s

$t = 5$ s

$t = 10$ s
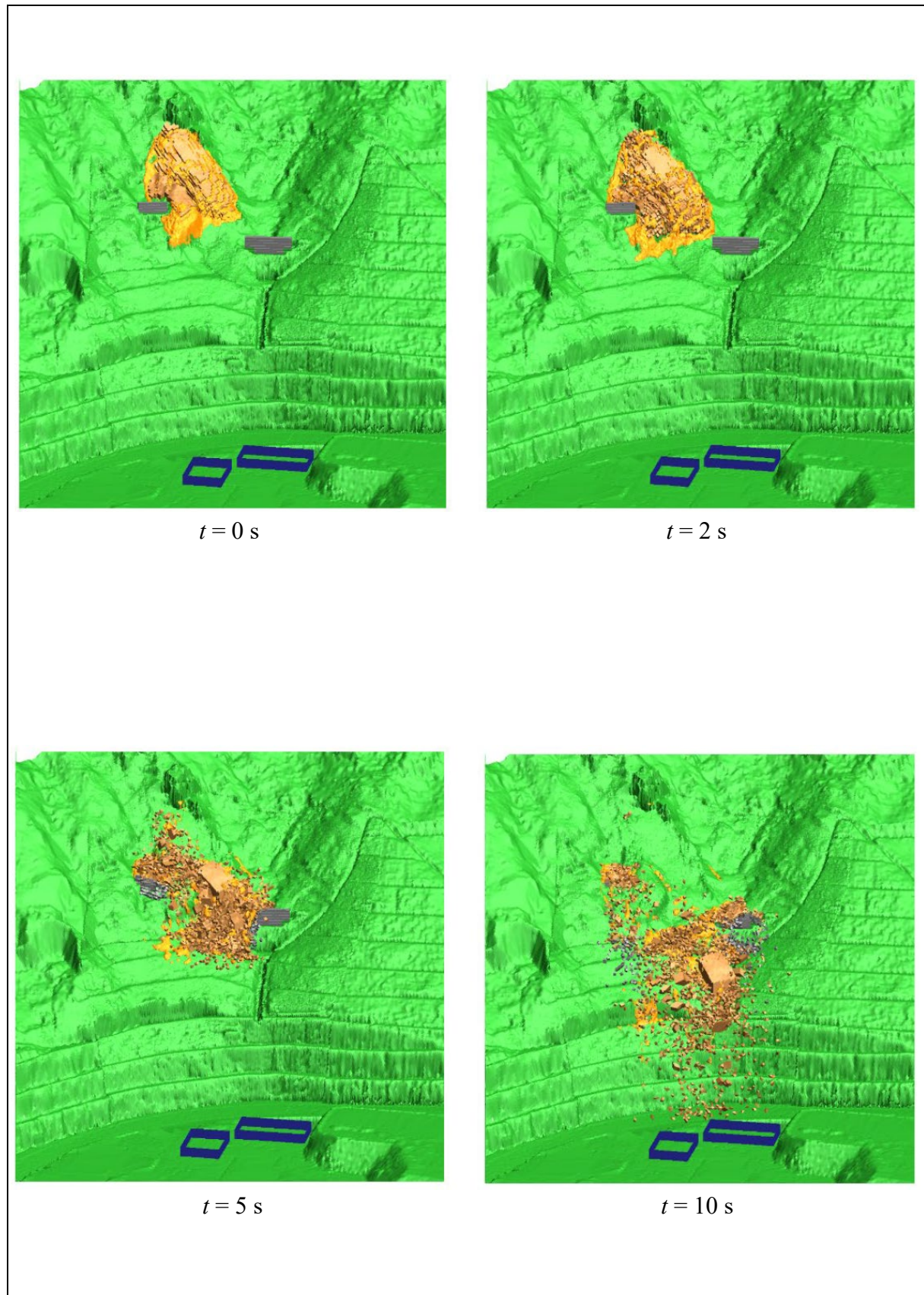
Figure 8.14   Simulation of the Lower Landslide (Sheet 1 of 2)

$t = 15$ s

$t = 20$ s

$t = 25$ s

$t = 30$ s
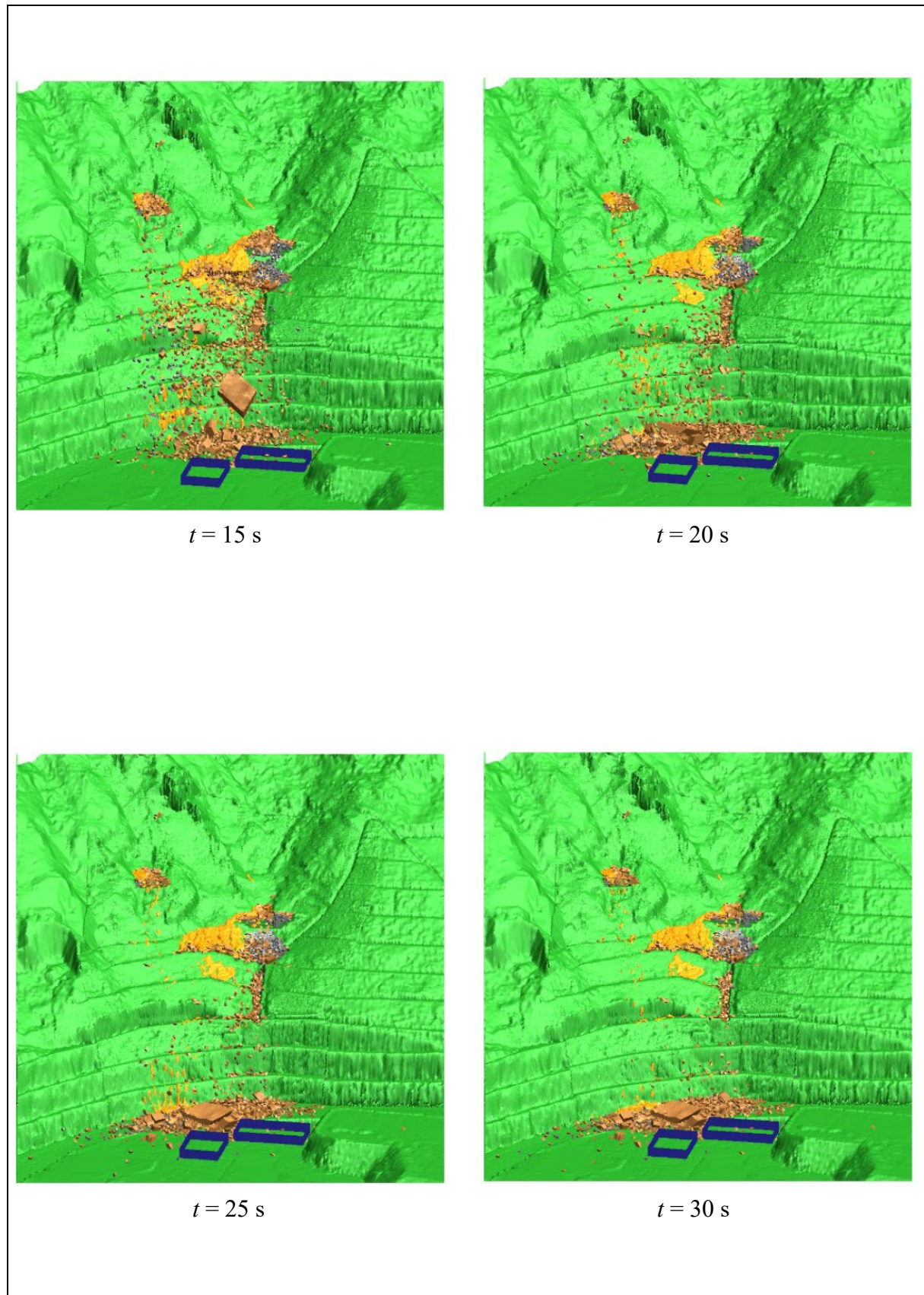
Figure 8.14   Simulation of the Lower Landslide (Sheet 2 of 2)
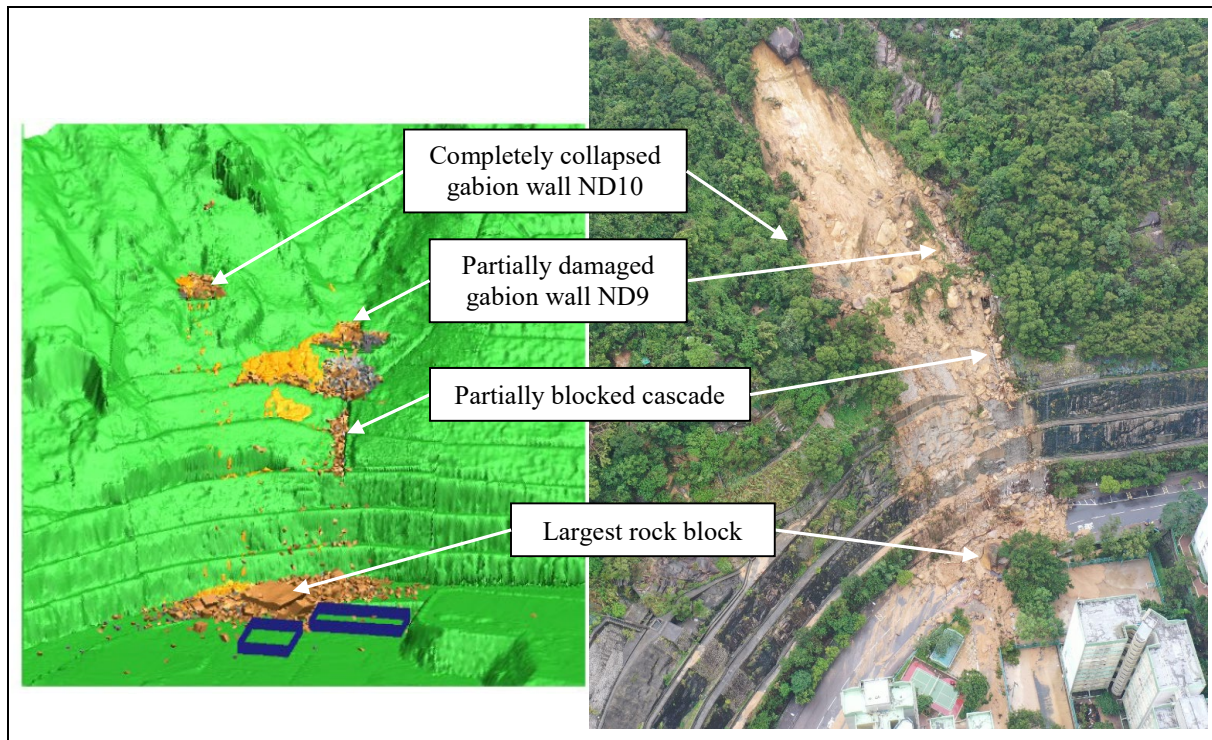
Figure 8.15   Debris Deposition in the Site and the LS-DYNA Model

8.6.5   Consistency with Field Observations and Previous Studies

The LS-DYNA simulation effectively captured the key characteristics and behaviour of the lower landslide, such as the lateral spreading of debris, deposition positions of rock blocks, and damage to structures. The simulation results closely aligned with the observations made after the landslides occurred. The analyses indicate that an apparent basal friction angle of about 28° matched the observed runout of the landslide debris, which is consistent with the previous rheological parameters back-calculated for open hillslope failures in Hong Kong (GEO, 2023).

Overall, the comprehensive debris analyses using LS-DYNA simulation demonstrated a high level of accuracy in predicting the actual landslide behaviour and providing valuable insights into the dynamics and mechanisms of this complex landslide event.

9   Discussion

9.1   General

The 8 September 2023 incident occurred on the natural hillside above Yiu Hing Road during a record-breaking severe rainstorm. The rainfall preceding the incident was the highest ever recorded by the nearby GEO raingauge No. H19 since it began operation in 1984. The landslide process unfolded within a short time frame.

Given the mode of the failure and its occurrence during the heavy rainfall, the incident was rain-induced. As there are no eyewitnesses on the actual sequence of the upper and lower

landslides, it has not been possible to establish confidently whether the two landslides occurred sequentially.

Figures 9.1 to 9.3 illustrate the reconstructed sequence of the events which led to the landslides on 8 September 2023.

9.2 Diagnosis of Probable Causes of the Landslides

The upper landslide was a small-scale, shallow (< 2 m deep) open hillslope translational debris avalanche, with an estimated failure volume of 100 m^3. It occurred at the interface between colluvium and corestone-rich CDG. Direct rainwater infiltration into the slope body was identified as a contributing factor to this landslide.

In contrast, the lower landslide was a massive-scale, structurally controlled translational rockslide involving basal failure along a persistent, locally stepped, undulating to planar sheeting joint, with an estimated failure volume of 3,900 m^3. This type of failure is unusual and is believed to be caused by a combination of several contributory factors specific to the location.

The hillside is steep, with slopes reaching up to 45°. It features distinct rock outcrops displaying persistent northeast-southwest joint patterns, which are evident on both the hillside and within the rocky stream course. The site of the lower landslide is characterised by a layer of corestone-rich CDG overlying the coreslab with tors and partially exhumed corestones along the spurline. The sheeting joint dips at 30° to 35° in a northeasterly direction (about 030° to 040°) and has the same orientation as the hillside. It daylights at the face of an abandoned quarry and along the flanks of the spurline.

The persistent sheeting joint below the source area formed the undulating basal failure plane on which structurally controlled failure could occur. Additionally, clay infill within the sheeting joint may have reduced the shearing resistance along the basal failure plane. The steep terrain profile and the adverse orientation of the persistent sheeting joint could have made it particularly susceptible to failures during rainstorms.

Numerical analyses suggest that the rise in the cleft water pressure in the sheeting joint could have contributed to the lower landslide. Two probable sources of water may have led to this increase in cleft water pressure:

(a) Direct rainwater infiltration: Seepage analyses suggest limited cleft water pressure could develop in the sheeting joint due to direct infiltration into the natural hillside (Section 8.3.2).

(b) Channel runoff: The rocky stream course along the western flank plays a crucial role in the landslide by providing a concentrated source of water. Furthermore, an ephemeral stream course in the hillside depression on this flank exacerbated the situation (Section 6). Seepage analyses indicate a build-up of transient cleft water pressure in the sheeting joint, with channel runoff seeping into the sheeting joint through the open rock joints (Section 8.3.2).
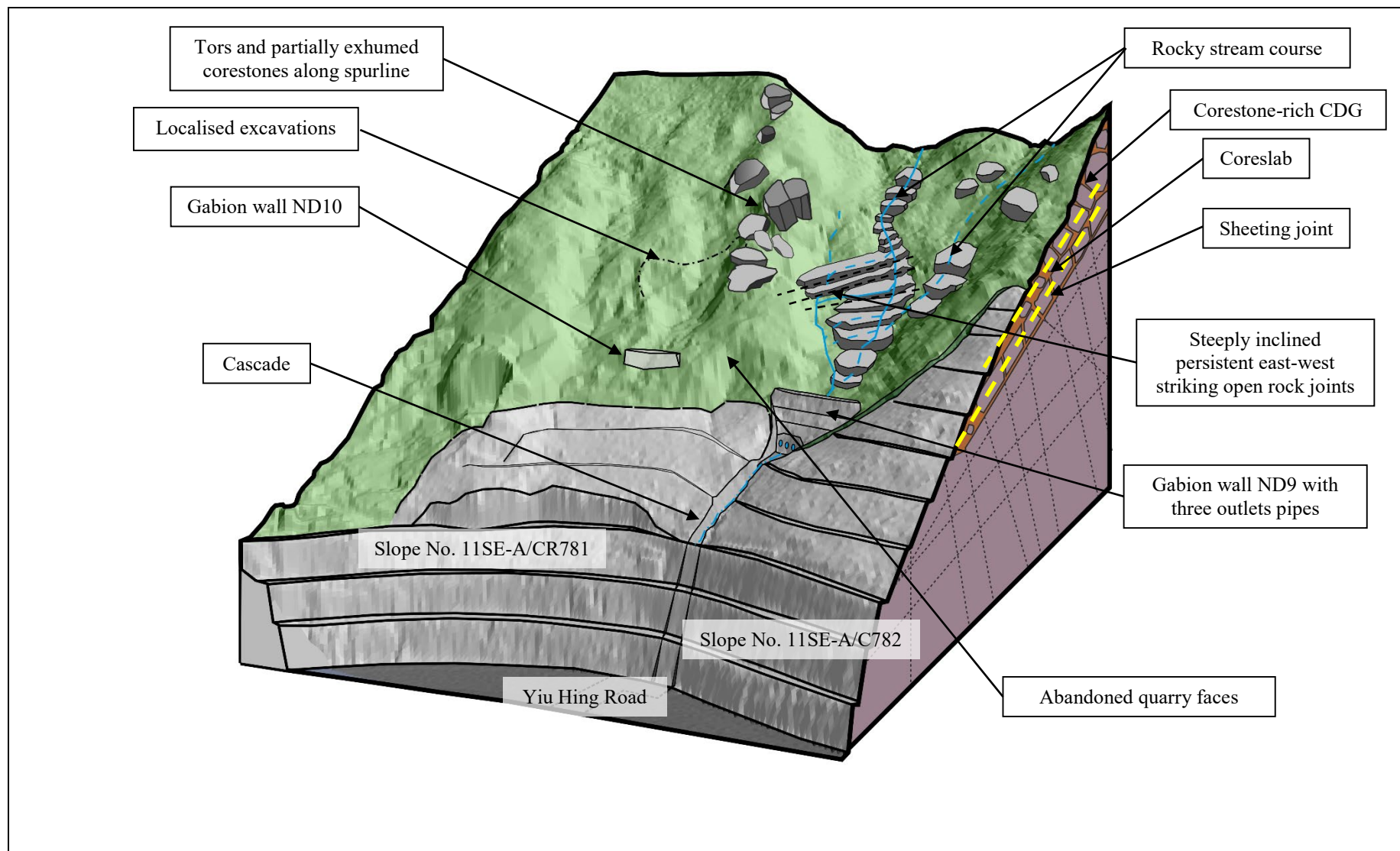
Figure 9.1   Ground Model - Before the Landslides

The labels in the figure are:
- Tors and partially exhumed corestones along spurline
- Localised excavations
- Gabion wall ND10
- Cascade
- Rocky stream course
- Corestone-rich CDG
- Coreslab
- Sheeting joint
- Steeply inclined persistent east-west striking open rock joints
- Gabion wall ND9 with three outlets pipes
- Slope No. 11SE-A/CR781
- Slope No. 11SE-A/C782
- Yiu Hing Road
- Abandoned quarry faces

Direct infiltration into the natural hillside

Excess surface runoff from overflow weirs along the catchwater

The channel runoff contributed abundant surface water to the steeply inclined east-west striking open rock joints.

This promoted water flow to the sheeting joint at the landslide area on the surface and at depth.

Stream course was not confined at flanks and channel runoff spread laterally

Yiu Hing Road

Figure 9.2   Ground Model - During the 7 to 8 September 2023 Rainstorm

Upper landslide scar

Lower landslide scar

Persistent, undulating sheeting joint formed basal failure plane

Gabion wall ND10 completely collapsed

Coreslab partially exposed

Gabion wall ND9 partially destroyed

Yiu Hing Road

Unfailed portion of in-situ material

Landslide debris, including sizable rock blocks, fell onto Yiu Hing Road and scattered on the rock cut slope
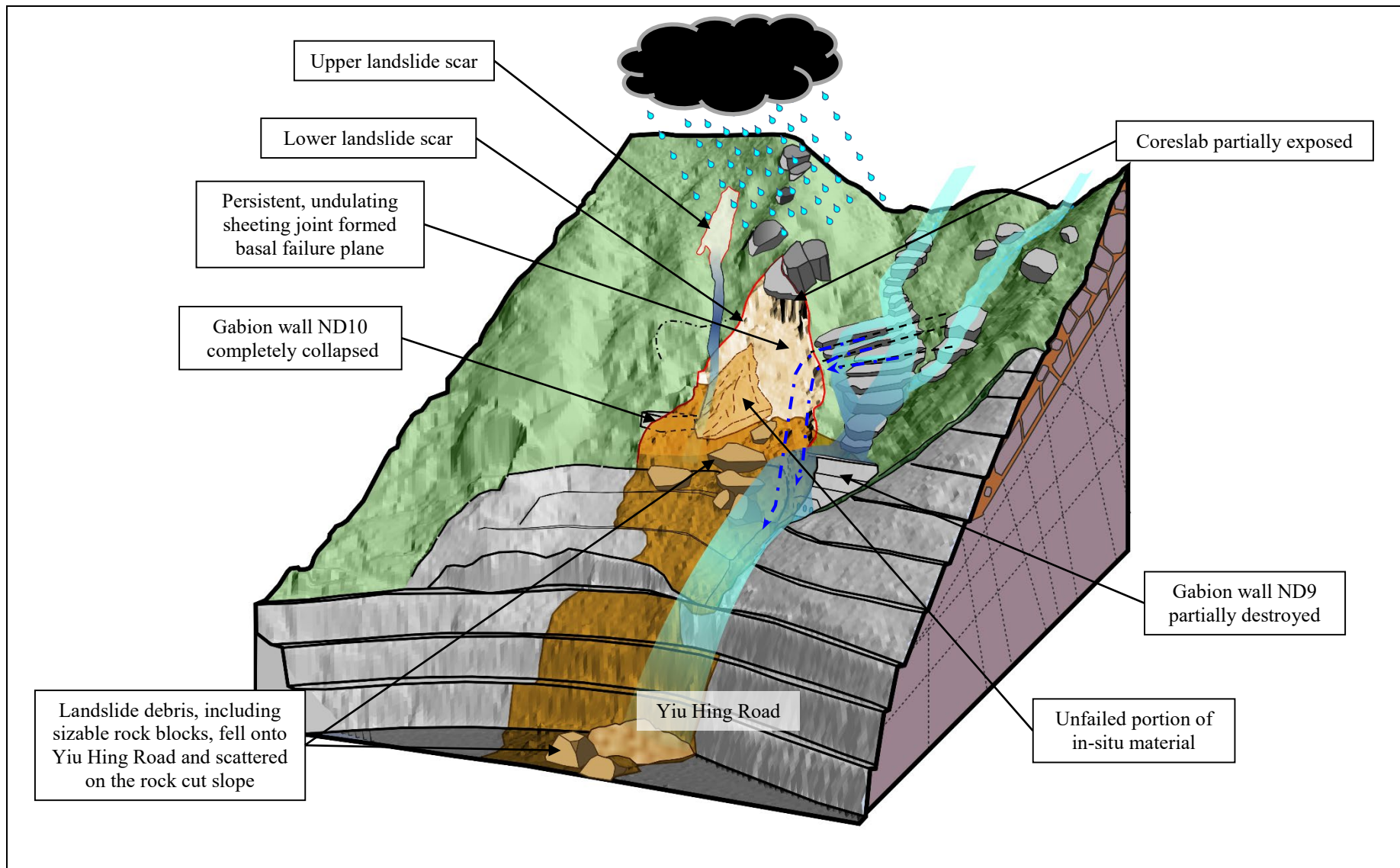
Figure 9.3   Ground Model - After the Landslides

The stream course is not confined to the flanks, allowing channel runoff to spread laterally during heavy rainfall. This area features steeply inclined, persistent, open sub-vertical east-west striking rock joints that facilitate water movement (Section 6.7). Furthermore, excess surface runoff from overflow weirs W4 and W5 could significantly contribute to the lower landslide by directing abundant surface water towards these steeply inclined open rock joints, ultimately channelling it towards the sheeting joint at the lower landslide source area.

This influx of water could promote flow both on the surface and at depth, weakening the groundmass through increased infiltration and surface erosion.

In summary, the combination of the hydrogeological conditions and unfavourable site settings could lead to a build-up of transient cleft water pressure in the sheeting joint. This increase in cleft water pressure could reduce the shearing resistance of the groundmass along the sheeting joint, ultimately contributing to the catastrophic landslide that occurred on the early morning of 8 September 2023.

10   Conclusions

The 8 September 2023 incident at the natural hillside above Yiu Hing Road was rain-induced and initiated when both the Black Rainstorm Warning and Landslip Warning were in effect. The 4- to 24-hour rainfall intensities preceding the incident were the most severe since rainfall data in the area became available.

The upper landslide was a small-scale, shallow open hillslope translational debris avalanche that initiated at the interface between colluvium and corestone-rich CDG. The landslide was triggered by the heavy rain and involved an estimated failure volume of 100 m^3. It was diagnosed that direct rainwater infiltration into the slope body during the rainstorm reduced the safety margin and led to the landslide.

The lower landslide, a massive-scale structurally controlled, translational rockslide, had an estimated failure volume of about 3,900 m^3. Excess surface runoff discharging from the overflow weirs along the catchwater to the rocky stream course could have increased the amount of water ingress through the open rock joints towards the landslide site. The combined effects of direct rainwater infiltration and seepage from the channel runoff in the rocky stream course into the sheeting joint through these open rock joints contributed to the build-up of transient cleft water pressure in the sheeting joint. It was diagnosed that the increased cleft water pressure within the regolith above the sheeting joint during the rainstorm reduced the safety margin and led to the landslide.

This incident highlights the importance of evaluating the unfavourable settings of the rock outcrops along the rocky stream course, as well as examining the underlying geological and geomorphological settings of similar granitic terrains when assessing natural terrain hazards. It furthermore manifests the need of controlling surface runoff along catchwaters in preventing landslides by implementing practical improvements for catchwaters and those associated with overflow weirs.

11   References

AECOM (2018). *Detailed Study of the 21 May 2016 Landslide on the Natural Hillside above Slope No. 8SE-A/F34 at Sai Kung Sai Wan Road, Sai Kung (GEO Report No. 336).* AECOM Asia Company Limited. Report to the Geotechnical Engineering Office, Civil Engineering and Development Department, Hong Kong, 101 p.

Arup (2024). *Additional Services for Back-analysis of 2023 Yiu Hing Road Landslide using 3D Modelling - Final Technical Note.* Ove Arup and Partners Hong Kong Limited. Report to the Geotechnical Engineering Office, Civil Engineering Development and Department, Hong Kong, 23 p.

Bachy (1985). *HDHA Contract No. SI/SKW/1 of 1984 Site Investigation: Shau Kei Wan Foothills.* Bachy Soletanche Group. Report to the Housing Department, Hong Kong, 136 p.

Barton, N. (1973). Review of a new shear strength criterion for rock joints. *Engineering Geology*, Elsevier, Amsterdam, vol. 7, pp 287-332.

Barton, N. & Choubey, V. (1977). The shear strength of rock joints in theory and practice. *Rock Mechanics*, Springer, Vienna, vol. 10, pp 1-54.

Barton, N., Wang, C. & Yong, C. (2023). Advances in joint roughness coefficient (JRC) and its engineering applications. *Journal of Rock Mechanics and Geotechnical Engineering*, vol. 15, pp 3352-3379.

Chan, C.C.L. & Chu, E.K.H. (2024). *Updated Frequency Analysis of Extreme Rainfall Values (Technical Note TN No. 5/2024).* Geotechnical Engineering Office, Civil Engineering and Development Department, Hong Kong, 397 p.

Cheng, Y.M. & Yip, C.J. (2007). Three dimensional asymmetrical slope stability analysis extension of Bishop's, Janbu's, and Morgenstern-Price's techniques. *Journal of Geotechnical and Geoenvironmental Engineering*, vol. 133, pp 1544-1555.

Deere, D.U. & Miller, R.P. (1966). *Engineering Classification and Index Properties of Rock.* US Air Force Weapons Laboratory, Kirtland Air Force Base, NM. Technical Report AFNL-TR-65-116.

Du, S.G., Lin, H., Yong, R. & Liu, G.J. (2022). Characterization of joint roughness heterogeneity and its application in representative sample investigations. *Rock Mechanics and Rock Engineering*, vol. 55, pp 3253-3277.

Enpack (1986a). *HKHA Contract No. 3 of 1985 Term Contract for Site Investigation 1985-87, Works Order No. 123 – Final Fieldwork Report.* Enpack (Hong Kong) Limited. Report to the Housing Department, Hong Kong, 136 p.

Enpack (1986b). *HKHA Contract No. 3 of 1985 Term Contract for Site Investigation 1985-87, Works Order Nos. 144, 145 & 170 – Final Fieldwork Report.* Enpack (Hong Kong) Limited. Report to the Housing Department, Hong Kong, 152 p.

Fredlund, D.G. & Xing, A. (1994). Equations for the oil-water characteristic curve. *Canadian Geotechnical Journal*, vol. 31, No. 4, pp 521-532.

Fugro (2011). *Stage 2 Study (Performance Review Only) Report, S2R 5/2011, Feature No. 11SE-A/C782 (Sub-division No. 1), Yiu Hing Road, Sai Wan Ho*. Fugro (Hong Kong) Limited. Report to the Geotechnical Engineering Office, Civil Engineering and Development Department, Hong Kong, 88 p.

Fugro (2013a). *Stage 3 Study Report, S3R 165/2010, Feature No. 11SE-A/C782 (Sub-division No. 2), Yiu Hing Road, Sai Wan Ho*. Fugro (Hong Kong) Limited. Report to the Geotechnical Engineering Office, Civil Engineering and Development Department, Hong Kong, 330 p.

Fugro (2013b). *Maintenance Manual, MM 124/2013, Feature No. 11SE-A/C782 (Sub-division No. 2), Yiu Hing Road, Sai Wan Ho*. Fugro (Hong Kong) Limited. Report to the Geotechnical Engineering Office, Civil Engineering and Development Department, Hong Kong, 80 p.

Gammon (1989). *HKHA Contract No. 205 of 1986 Term Contract for Site Investigation 1987-89, Works Order No. 60 – Final Fieldwork Report*. Gammon Construction Limited. Report to the Housing Department, Hong Kong, 46 p.

Gammon (1994). *HKHA Contract No. 91 of 1992 Term Contract for Ground Investigation 1993-95, Works Order No. 160 – Fieldwork Report*. Gammon Construction Limited. Report to the Housing Department, Hong Kong, 82 p.

GCO (1980). *Catchwater Study First Report*. Geotechnical Control Office, Public Works Department, Hong Kong, 37 p.

GCO (1981). *Geotechnical Area Study: Shau Kei Wan – GAS Report 6*. Geotechnical Control Office, Public Works Department, Hong Kong, 188 p. plus maps.

GEO (2012). *Hong Kong & Kowloon: Solid and Superficial Geology Edition II*. Hong Kong Geological Survey, Map Series HGM 20, Sheet 11, 1:20,000 scale. Geotechnical Engineering Office, Civil Engineering and Development Department, Hong Kong.

GEO (2020). *Guide to Retaining Wall Design (Geoguide 1) (Continuously updated e-version released on 1 June 2020)*. Geotechnical Engineering Office, Civil Engineering and Development Department, Hong Kong, 245 p.

GEO (2023). *Guidelines on Assessment of Debris Mobility for Open Hillslope Failures (GEO Technical Guidance Note No. 34)*. Geotechnical Engineering Office, Civil Engineering and Development Department, Hong Kong, 16 p.

HD (1986a). *Shaukeiwan East Public Housing Development - First Geotechnical Design Report*. Housing Department, Hong Kong, 211 p.

HD (1986b). *Shaukeiwan East Public Housing Development - Second Geotechnical Design Report*. Housing Department, Hong Kong, 543 p.

HD (1987). *Shaukeiwan East Public Housing Development - Third Geotechnical Design Report*. Housing Department, Hong Kong, 179 p.

Hencher, S.R. (1987). *The Implications of Joints and Structures for Slope Stability*. In: Anderson, M.G. & Richards, K.S., Ed., Slope Stability, John Wiley & Sons Ltd., New York, pp 145-186.

Hencher, S.R. & Richards, L.R. (1982). The basic frictional resistance of sheeting joints in Hong Kong granite. *Hong Kong Engineer*, Hong Kong, pp 21-25.

Intrafor (2010). *CEDD Contract No. GE/2008/36 Feature No. 11SE-A/C782, Yiu Hing Road, Sai Wan Ho, Works Order No. GE/2008/36/31/038(G) – Final Fieldwork Report*. Intrafor Hong Kong Limited. Report to the Geotechnical Engineering Office, Civil Engineering and Development Department, Hong Kong, 126 p.

Intrusion (1990). *HKHA Contract No. 143 of 1988 Term Contract for Site Investigation 1989-91, Works Order No. 237 – Fieldwork Report*. Intrusion-Prepakt (Far East) Limited. Report to the Housing Department, Hong Kong, 30 p.

Koo, R.C.H. (2017). *3D Debris Mobility Assessment Using LS-DYNA (GEO Report No. 325)*. Geotechnical Engineering Office, Civil Engineering and Development Department, Hong Kong, 90 p.

Leung, L.C.F., Li, R.P.M., Leung, S.C.H. & Lee, R.W.H. (2024). *Lesson Learnt: A Showcase to the Unprecedented Scale Emergency Repair Works for a Massive Natural Terrain Landslide at Shau Kei Wan in Hong Kong Occurring in September 2023*. The HKIE-CIE-IEM Tripartite Seminar Hong Kong, 28 November 2024, 17 p.

Look, B.G. (2014). *Handbook of Geotechnical Investigation and Design Tables 2nd Edition*. Taylor & Francis Group, London, UK.

Martin, R.P. (2009). Qualitative risk assessment of catchwaters in Hong Kong based on simplified geomorphological hazard mapping. *Quarterly Journal of Engineering Geology and Hydrogeology*, vol. 42, No. 4, pp 459-471.

Philipson, H.B., Hall, D.L. & Martin, R.P. (1982). *Catchwater Study Second Report (Volume 1)*. Geotechnical Control Office, Public Works Department, Hong Kong, 88 p.

Ram, B.K. & Basi, A. (2019). A modified JRC-JCS model and its applicability to weathered joints of granite and quartzite. *Bulletin of Engineering Geology and the Environment*, vol. 78, pp 6089-6099

Scott Wilson (1999). *Specialist API Services for the Natural Terrain Landslide Study – Interpretative Report & Task B Final Report*. Scott Wilson (Hong Kong) Limited. Report to Geotechnical Engineering Office, Civil Engineering Department, Hong Kong, 41 p. plus 10 appendices.

Strahler, A.N. (1964). *Quantitative Geomorphology of Drainage Basin and Channel Networks*. In: Chow, V., Ed., Handbook of Applied Hydrology, McGraw Hill, New York, pp 439-476

Wong, H.N. & Ho, K.K.S. (1996). *Thoughts on the assessment and interpretation of return periods of rainfall (Discussion Note No. DN 2/96)*. Geotechnical Engineering Office, Civil Engineering Department, Hong Kong, 19 p.

Appendix A

Aerial Photograph Interpretation

Contents

List of Table

List of Figure

A.1 Introduction

This Appendix presents an aerial photograph interpretation (API) of the landslide site and its vicinity, which includes a detailed site development history, geomorphological setting and past slope instabilities. Figure A1 shows a summary of API observations. More than 65 pairs of aerial photographs have been reviewed covering the period from 1945 to 2022 (Table A1).

A.2 Summary

Site Development History

The earlier available aerial photographs in 1945, the hillside below and up to the toe of the 2023 landslide site was dominated by terrain disturbed significantly by anthropogenic activities including artisanal mining, quarrying and agriculture. The toe of the landslide site marked the upper extent of excavations and terraces apparently associated with these activities. Much larger scale excavations are evident within the eastern side of the valley below and to the northeast of the landslide site, and also on the upper ridgeline to the southwest of the landslide site where the scars of excavations are still evident. In addition, within and adjacent to the landslide site, there is evidence of small-scale excavations possibly associated with localised stone quarrying or artisanal mining of quartz veins. Above the landslide site, the catchwater channel and access path were already constructed by 1945. Whilst the construction of the catchwater may have involved some fill placed on the slopes below, there is no obvious evidence of significant fill or disturbance below the catchwater at the landslide site in 1945.

The 1949 photographs were taken at a lower level than the 1945 photographs and provide a clearer view of the disturbed terrain in and around the landslide site. A distinct cut slope is evident at the toe of the landslide site below which agricultural terraces were present at this time. Local, small excavations are evident along the eastern flank of the landslide site and there is evidence of fresh excavations and/or localised erosion of existing excavations. Some agricultural terraces were observed developing on the flat to gently sloping ground below the upper limit of the main excavation.

The 1963 photographs offer the highest resolution images and a number of natural and anthropogenic features are readily apparent in and around the landslide site. The tors and exhumed corestones are evident at the upper face of the lower landslide scar and above the crest. These features are correlated accurately with tors that either failed or remained at the crest of the landslide site. Within the rocky stream course on the western flank, bright tone scars are evident and a pile of stones are present both suggesting minor excavations within the rock exposures. In addition, a bright tone scar extends along the depression along the eastern flank of the lower landslide scar, indicating additional minor excavations have been undertaken between 1949 and 1963. Below the landslide site, huts have been erected throughout the valley and along the eastern valley side as part of a substantial squatter development at that time. Agricultural terraces have also been extended up to and in the vicinity of the landslide site and a footpath can be observed connecting the squatter development to the catchwater above.

A hut is present on a pre-existing flat platform immediately below the toe of the lower landslide scar in the 1969 photographs. By 1972, there was a significant increase in the number

and extent of huts on the gentle terrain below the lower landslide scar and agricultural activities were present on the flat ground on the western flank.

The 1989 photographs indicate the early stages of site formation works for the construction of the Yiu Hing Estate below and adjacent to the landslide source area. At this time, construction of the large cut slopes were in progress and both gabion walls ND8, ND9 and ND10 had been constructed. By 1991, the cut slopes together with the culvert outlet and cascade below, were constructed. In these photographs the margin of gabion wall ND9 is clearly evident and indicates that the gabion wall was constructed across the entire drainage line without any significant gap at both ends.

There were no obvious significant changes to the landslide site since the early 1990's.

Geomorphological Setting and Past Instability

The early photographs, and particularly those taken in 1963, reveal a rocky landscape within the vicinity of the landslide site. This landscape is broadly similar to a truncated spurline and extends from the rocky stream course alongside the western flank, to another well-defined drainage line to the east. The hillside is steep and characterised by a number of subvertical, linear rock cliffs controlled by persistent joints striking predominantly northeast-southwest, and also striking east-northeast-west-southwest and north-northwest-south-southeast. A number of discontinuous depressions flanked by rugged rock outcrops and exhumed corestones are present, but drainage lines and gullies are generally poorly-defined. The landscape together with the clear evidence of quarrying and mining in the vicinity suggest that this part of the hillside may have been modified by human activities.

The catchment above the landslide site extends up to approximately +456 mPD and consists of a relatively narrow and shallow valley which drains in a north-northeast direction. The upper part of the catchment is characterised by a number of rock outcrops and steep cliffs. Below these outcrops the valley is draped with bouldery colluvial deposits whilst the valley sides and boundary spurlines expose residual soils, saprolite, tors and exhumed corestones. Drainage lines are poorly developed within the upper part of the catchment but become increasingly incised within gullies at and below the middle part. The main valley narrows further where two of the main tributaries merge to form the rocky steam course, and this eventually flows north-northeast alongside the western flank. Rock is exposed along the mid to lower parts of this drainage line. Although the rocky stream course flows in a general north-northeast direction, its tributaries display linearity orientated towards the northeast suggesting a degree of structural control.

Below the catchwater, the hillsides of the lower catchment become much steeper and composes of saprolite and rock outcrops with less evidence of colluvial deposits.

The majority of the relict landslides are located on the valley side slopes above the catchwater. Three additional relict landslide features (L1 to L3) have been identified in the 1949 photographs above the landslide site (Figure A1). Three relict landslide features are evident on the slopes below the catchwater and these are located above and to the south of the western flank (ENTLI Nos. 11SEA0264E and 11SEA0265E) and eastern flank (L3) of the lower landslide scar, respectively. Both ENTLI features are classified as C2 relict landslides,

i.e. a broad depression identified with low confidence. Furthermore, ENTLI No. 11SEA0265E is located at a narrow linear depression which appears to be anthropogenic in origin. Landslide L3 has a similar size to ENTLI No. 11SEA0264E. However, it is also possible that both are anthropogenic in origin given the site setting.

A.3   Detailed Observation

Year	Observations

1945   High level stereopair of poor quality. Extensive terrain disturbance observed on the hillside below and up to the toe of the 2023 landslide site, including artisanal mining, quarrying and agriculture. The toe of the landslide site marked the upper extent of excavations and terraces apparently associated with these activities. Within and adjacent to the landslide site, there is evidence of small-scale excavations. Catchwater and access path were already constructed above the landslide site.

1949   Medium level stereopair of good quality. Apart from a clearer view of the disturbed terrain in and around the landslide site, a distinct cut slope was evident at the toe of the landslide site below which agricultural terraces were present. Small excavations were more visible along the eastern flank of the landslide site and evidence of fresh excavations and/or localised erosion of existing excavations observed. Tors and exhumed corestones were evident at the upper surface of the lower landslide scar and above the crest. Some agricultural terraces were observed developing on the flat to gently sloping ground below the upper limit of the main excavation. Three additional relict landslide features (L1 to L3) are identified above the landslide site

1963   Low level stereopair of excellent quality. A number of natural and anthropogenic features are apparent. The tors and exhumed corestones are shown more clearly and correlate accurately with tors that either failed or remained at the crest of the lower landslide scar. Bright tone scars and a pile of stones evident in the rocky stream course along the western flank, suggesting minor excavations. Similar scars were also observed on the eastern flank suggesting further minor excavations since 1949. Substantial squatter development over the disturbed terrain below the landslide site, extending up to the toe. Two relict landslides (ENTLI Nos. 11SEA0264E and 11SEA0265E) are evident above the lower landslide scar. Footpath is observed to be connecting the squatter development to the catchwater above.

1964   High level stereopair of moderate quality. No significant changes are apparent.

1967   Medium level stereopair of moderate quality. No significant changes are apparent.

1969   Medium level stereopair of moderate quality. No significant changes are observed, though a small hut appeared on the pre-existing flat platform immediately below the toe of the lower landslide. The terrain above the disturbed terrain became more vegetated.

Year	Observations
1972	Low level stereopair of good quality. Significant increase in the number and extent of squatter development below the landslide site. Some agricultural activities were present of the flat ground on the eastern flank of the lower landslide scar.
1973	Low level single photograph of moderate quality. No significant changes are apparent.
1974	High level single photograph of moderate quality. No significant changes are apparent.
1975	High level stereopair of moderate quality. No significant changes are apparent.
1976	Low level stereopair of good quality. No significant changes are apparent.
1977	Low level stereopair of good quality. No significant changes are apparent.
1978	Low level single photograph of good quality. No significant changes are apparent.
1979	Low level stereopair of good quality. No significant changes are apparent.
1980	Low level stereopair of good quality. No significant changes are apparent.
1981	High level stereopair of moderate quality. No significant changes are apparent.
1982	High level stereopair of moderate quality. No significant changes are apparent.
1983	High level stereopair of moderate quality. No significant changes are apparent.
1984	Low level stereopair of good quality. No significant changes are apparent.
1985	Low level stereopair of good quality. No significant changes are apparent, except vegetation growth is apparent above the squatter development.
1986	Low level stereopair of good quality. No significant changes are apparent.
1987	Low level stereopair of good quality. No significant changes are apparent.
1988	High level stereopair of moderate quality. No significant changes are apparent except that vegetation grew denser and some agricultural terraces appeared to be abandoned.
1989	Low level stereopair of good quality. Squatter development was cleared and replaced by site development works. Some slope works are apparent to the east and west of the landslide site. Gabion walls ND8, ND9 and ND10 were under construction. Prominent tors and exhumed corestones are still apparent, but denser vegetation covering the surrounding area.

Year	Observations
Year	**Observations**

1990   Low level stereopair of good quality. Gabion walls ND8, ND9 and ND10 appeared to be completed or mostly formed. Gabion wall ND9 appeared to straddle the entire rocky stream course without any significant gap at both ends. Upper portion of slope No. 11SE-A/C782 mostly formed and excavation at slope No. 11SE-A/CR781 at the toe of the lower landslide scar commenced.

1991   Low level stereopair of good quality. Slope No. 11SE-A/C782 was under construction. Cascade between slope Nos. 11SE-A/CR781 and 11SE-A/C782 appeared to be completed.

1992   Low level stereopair of good quality. Stone pitching and hydroseeding are apparent on slope No. 11SE-A/CR781. Dense vegetation is visible across the landslide site.

1993   Low level stereopair of good quality. Site formation was ongoing with foundation of Yiu Kwai House laid. Yiu Hing Road was under construction.

1994   Low level stereopair of good quality. Vegetation growth obscuring gabion wall ND10 and only larger tors and exhumed corestones are observable.

1995   Low level single photograph of good quality. No significant changes are apparent.

1996   Low level stereopair of good quality. No significant changes are apparent.

1997   Low level stereopair of good quality. No significant changes are apparent.

1998   Low level stereopair of good quality. No significant changes are apparent except vegetation fully obscuring gabion wall ND10.

1999   Low level stereopair of good quality. No significant changes are apparent.

2000   Low level stereopair of good quality. No significant changes are apparent.

2001   Low level stereopair of good quality. No significant changes are apparent.

2002   Low level stereopair of good quality. No significant changes are apparent.

2003   Medium level stereopair of good quality. No significant changes are apparent.

2004   Low level stereopair of good quality. No significant changes are apparent.

2005   Medium level stereopair of good quality. No significant changes are apparent.

2006   Medium level stereopair of good quality. No significant changes are apparent.

2007   Medium level stereopair of good quality. No significant changes are apparent.

Year	Observations
2008	Medium level stereopair of good quality. No significant changes are apparent.
2009	Low level stereopair of good quality. No significant changes are apparent.
2010	Medium level stereopair of good quality. No significant changes are apparent.
2011	Medium level stereopair of good quality. No significant changes are apparent except vegetation obscuring the upper portion of slope No. 11SE-A/CR781 and gabion wall ND9.
2012	Low level stereopair of good quality. No significant changes are apparent.
2013	Low level stereopair of good quality. No significant changes are apparent.
2014	Low level stereopair of good quality. No significant changes are apparent.
2015	Medium level stereopair of good quality. No significant changes are apparent.
2016	Medium level stereopair of good quality. No significant changes are apparent.
2017	Medium level stereopair of good quality. No significant changes are apparent.
2018	Medium level stereopair of good quality. No significant changes are apparent.
2019	Medium level stereopair of good quality. No significant changes are apparent.
2021	Medium level stereopair of good quality. No significant changes are apparent.
2022	Medium level stereopair of good quality. No significant changes are apparent.

Table A1   List of Aerial Photographs (Sheet 1 of 3)

Date of Photograph (dd/mm/yyyy)	Photograph Number [1]	Altitude (ft)
11/11/1945	Y475 & Y476	20,000
08/05/1949	Y1435 & Y1436	8,600
01/02/1963	Y7078 & Y7079	2,700
13/12/1964	Y12831 to 12833	12,500
16/05/1967	Y13309 & Y13310	6,250
1969	Y14739 & Y14740	/
24/06/1972	Y1845 & Y1846	2,500
12/12/1973	7019	3,000
21/11/1974	9697	12,500
19/12/1975	11706 & 11707	12,500
28/01/1976	12606 to 12608	4,000
15/09/1977	19290 & 19291	4,000
05/12/1978	23887	4,000
14/09/1979	26846 & 26847	4,000
28/11/1979	28013 & 28014	10,000
16/04/1980	29805 to 29807	4,000
26/10/1981	39020 to 39022	10,000
10/10/1982	44468 & 44469	10,000
30/11/1983	51336 & 51337	10,000
27/01/1984	53370 & 53371	3,500
18/05/1985	A767 & A768	4,000
20/09/1986	A5967 to A5970	4,000
09/09/1987	A10301 & 10302	4,000
16/01/1988	A12213 & A12214	10,000
16/08/1989	A17794 & A17795	4,000
20/03/1990	A20850 & A28051	4,000
04/10/1991	A28071 & A28072	4,000

Note: (1) Photographs numbered with CN, CW, CS and E are in colour. All others are in black and white.

Table A1   List of Aerial Photographs (Sheet 2 of 3)

Date of Photograph (dd/mm/yyyy)	Photograph Number [1]	Altitude (ft)
12/05/1992	A30907 & A30908	4,000
04/02/1993	CN3169 & CN3170	4,000
05/05/1994	CN6863 to CN6864	4,000
07/12/1995	CN12649	3,500
07/06/1996	CN14097	4,000
18/11/1996	CN15711 & CN15712	5,000
23/07/1997	CN17644 to CN17645	4,000
23/10/1998	CN21146	4,000
03/11/1999	CN24030	5,000
16/09/2000	CN28236	4,000
15/03/2001	CN30105 & CN30106	4,000
17/04/2002	CW39531 to CW39532	3,500
31/05/2003	CW47572	4,000
19/10/2003	RW2992 & RW2993	8,000
04/03/2004	CW55557 to CW 55560	4,000
05/03/2005	RW5189	6,000
05/03/2005	RW5216 & RW5217	6,000
19/09/2006	CW72460 & CW72461	4,000
21/12/2006	CS2375	6,000
23/11/2007	CS8749 & CS8750	6,000
26/08/2009	CS83499 & CS83500	3,000
24/05/2010	CS28701 & CS28702	6,000
04/07/2011	CS32829 & CS32830	6,000
09/05/2012	CW96813 to CW96815	2,000
01/06/2013	CW103836 & CW103837	2,000
27/06/2014	CW107998 & CW107999	2,000
01/01/2015	CS54996 & CS54997	6,000

Note: (1) Photographs numbered with CN, CW, CS and E are in colour. RW are infra-red interpretation. All others are in black and white.

Table A1   List of Aerial Photographs (Sheet 3 of 3)

Date of Photograph (dd/mm/yyyy)	Photograph Number [1]	Altitude (ft)
01/01/2016	CS62340 & CS62341	6,000
30/04/2017	E24784C to E24787C	6,900
05/10/2018	E47445C & E47446C	6,900
03/10/2019	E071344C & E071345C	6,000
08/01/2020	E085910C to E085912C	6,900
06/01/2021	E118893C & E118894C	6,900
11/01/2022	E146124C & E146125C	6,900

Note: (1) Photographs numbered with CN, CW, CS and E are in colour. All others are in black and white.
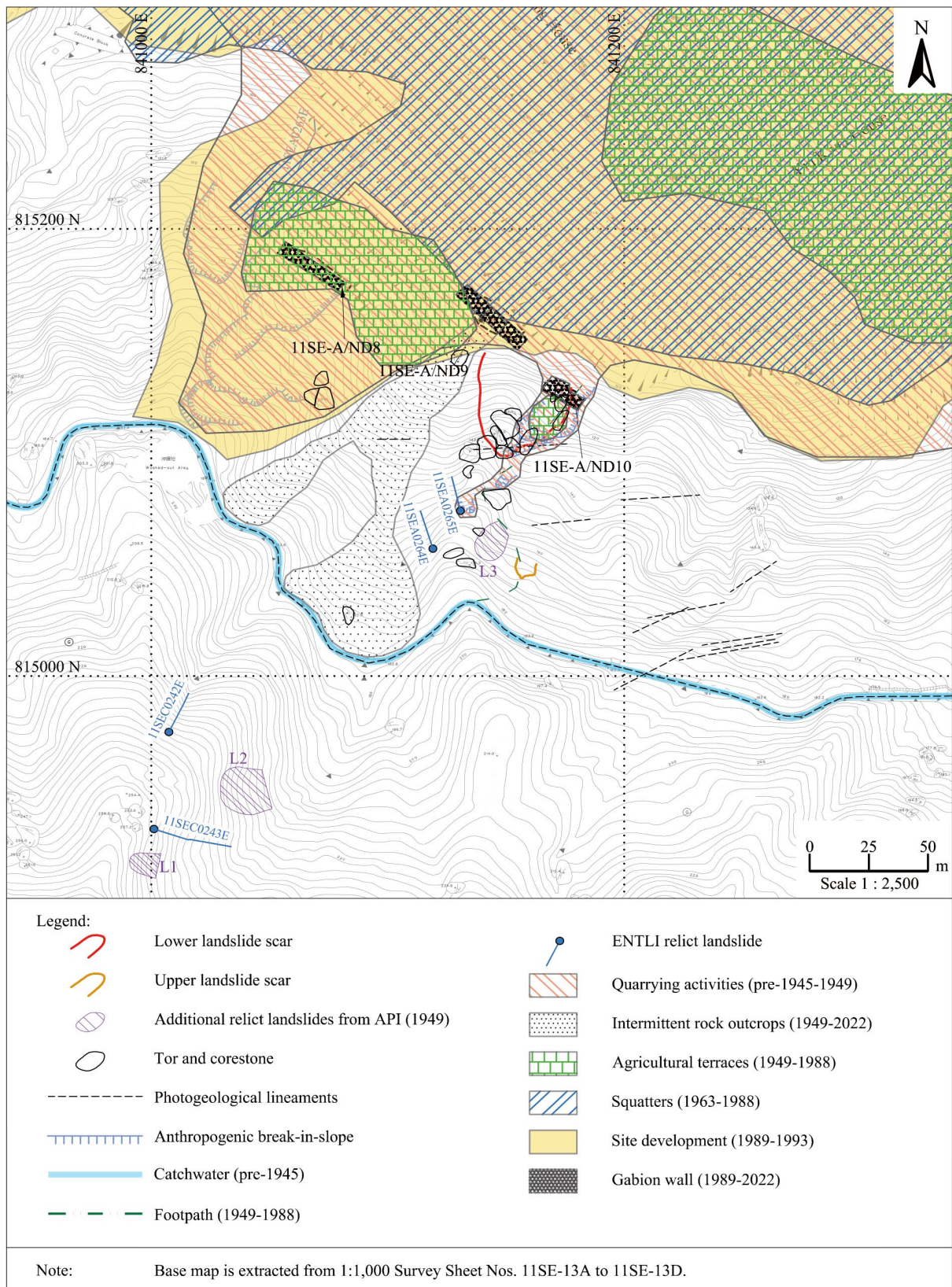
Figure A1   Summary of API Observations

Appendix B

CCTV Footage

Contents

List of Figure

List of Videos

Figure B1   Location Plan of CCTV Cameras

Note: Time shown in the footage is for reference only.

Video B1   Landslide Footage captured by the CCTV Camera at the Pedestrian-covered Walkway near Yiu Kwai House

Note: Time shown in the footage is for reference only.

Video B2 Landslide Footage captured by the CCTV Camera at the Refuse Collection Point near Yiu Kwai House

Note: Time shown in the footage is for reference only.

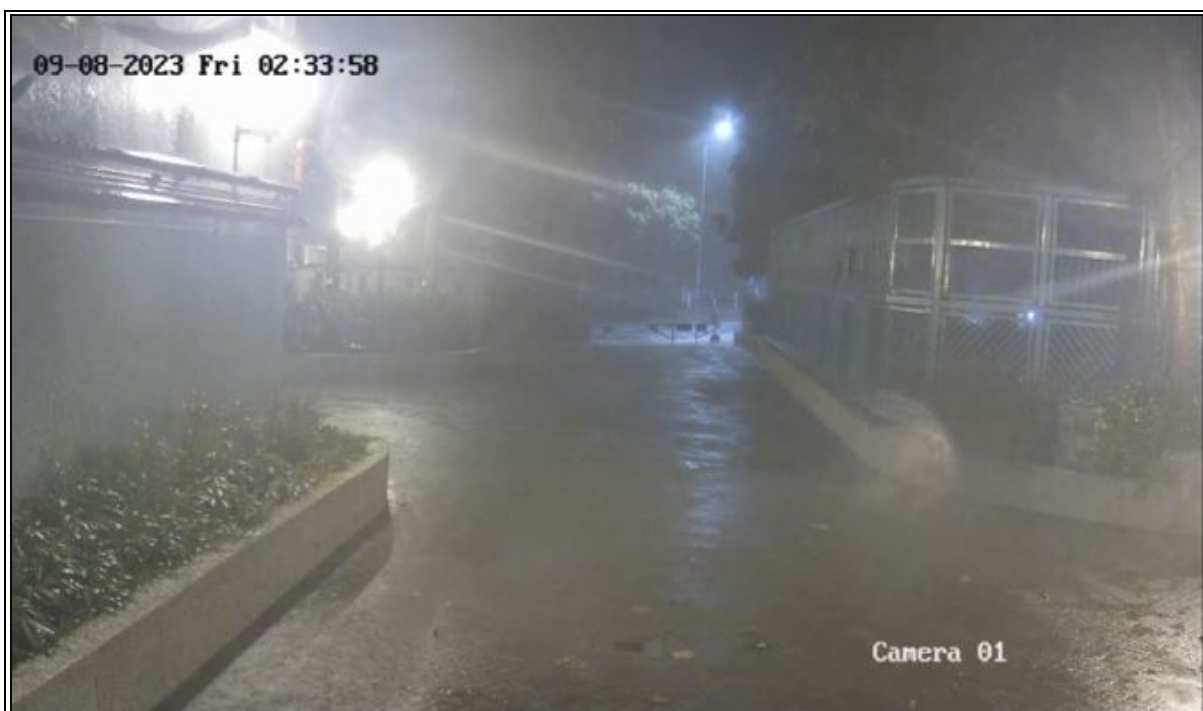**Video B3 Passing Car captured by CCTV Camera at the Pedestrian-covered Walkway near Yiu Kwai House**

Appendix C

Channel Runoff associated with Rainfall

Contents

List of Tables

List of Figures

C.1 General

The Mount Parker Lower Catchwater is an open channel that traverses above the lower landslide scar with the nearest distance of only about 42 m. The channel is trapezoidal in shape, and the flow direction is from the west to the east. The catchwater starts at a small intake dam at the western end, from where channel runoff from a major stream course at Mount Parker can flow into the catchwater (Figure C1). Five overflow weirs (W1 to W5) are provided at different locations along the catchwater before it traverses above the landslide location (Figure C2). The catchwater section between the intake dam and overflow weir W5 is about 370 m long on plan. Discharge from overflow weirs W4 and W5, along with surface runoff collected from the catchment below the catchwater, can flow into the rocky stream course adjacent to the lower landslide scar.

According to the WSD record drawings, the openings at overflow weirs W1, W3, and W5 were enlarged by reducing their crest levels under WSD's Contract 'Improvement to Tai Tam East Catchwaters' around 1995 (Figure C3). However, there is no information available about the structural details and design calculations of the flow capacity of the catchwater and overflow weirs before and after modification works.

Maintenance works, including repair of spalled and delaminated concrete, were carried out locally along the catchwater under WSD's Project 'Reconstruction of Catchwater Channels and Upgrading of Adjoining Priority Slopes on Hong Kong Island and Lantau Island' in around the year 2002. No modifications to the size of the concerned catchwater section or the weirs were made.

This Appendix evaluates the channel runoff in the rocky stream course adjacent to the landslide location at the time of the failure. Due to overflow weirs W1 to W5 and the site setting, the catchment above and below the concerned catchwater section was divided into six sub-catchment areas (Areas 1 to 6) in the assessment as shown in Figure C4.

To assess the impact of the catchwater on the runoff condition adjacent to the landslide location, in addition to the actual site setting at the time of the failure, the channel runoff in the rocky stream course was also estimated in two hypothetical scenarios:

> (a) Overflow weirs W1, W3 and W5 were not modified until around 1995, and

> (b) The catchwater was not constructed before 1945, while all else remains the same.

The catchment area (Area 7) considered in the second hypothetical scenario is shown in Figure C5.
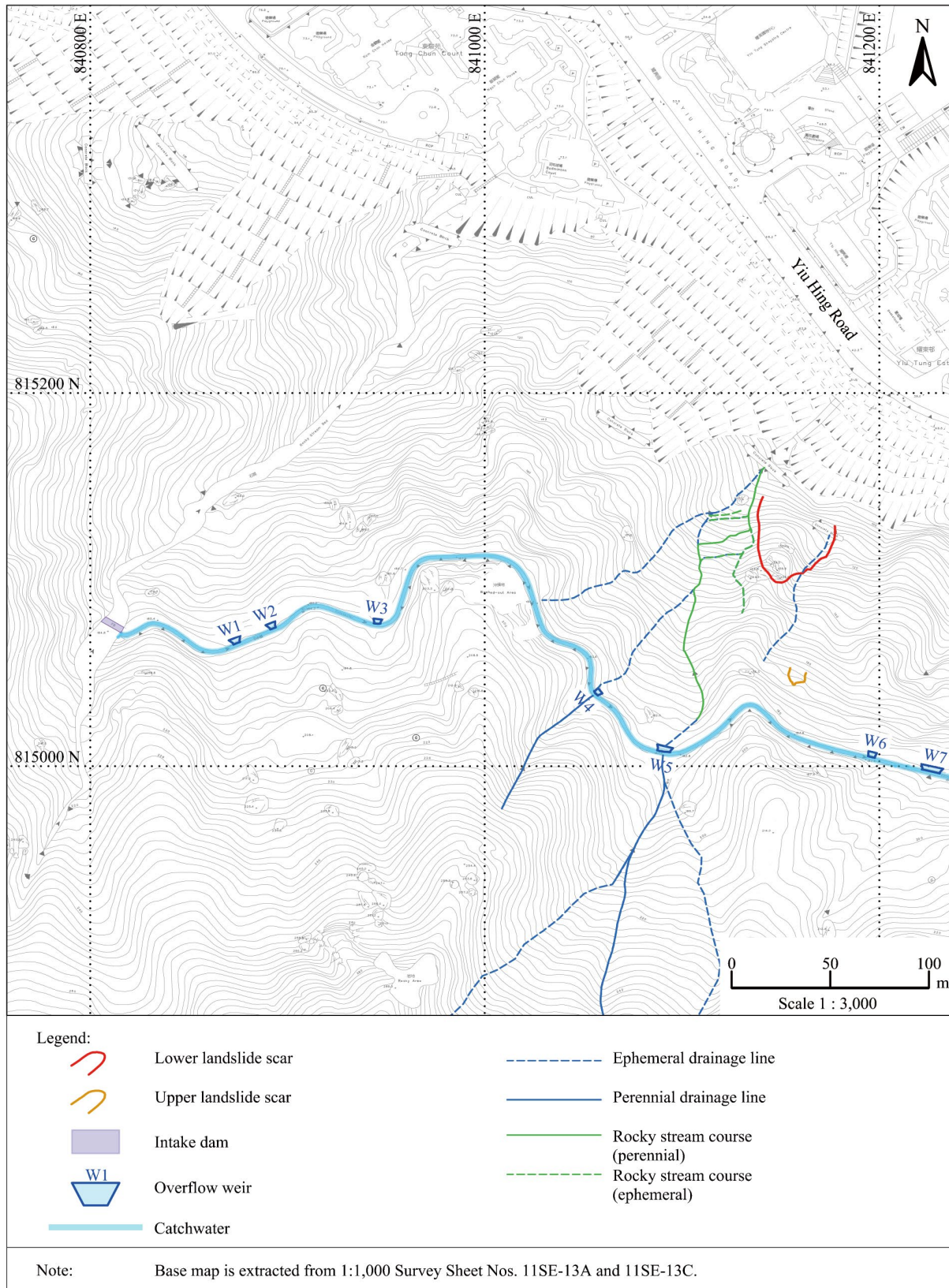
Figure C1 Layout Plan of the Catchwater Section
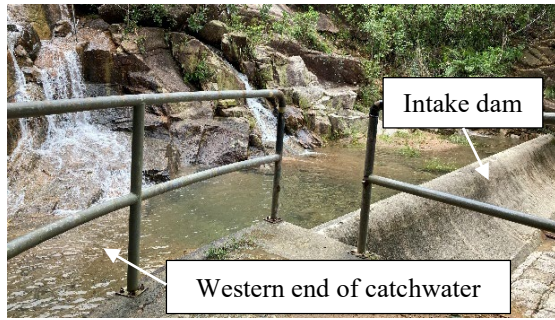
(a) Intake Dam at the Western End of the Catchwater
(Photograph taken on 12 September 2023)

(b) Overflow Weir W1
(Photograph taken on 2 May 2024)

(c) Overflow Weir W2
(Photograph taken on 2 May 2024)

(d) Overflow Weir W3
(Photograph taken on 2 May 2024)

(e) Overflow Weir W4
(Photograph taken on 2 May 2024)

(f) Overflow Weir W5
(Photograph taken on 2 May 2024)

Figure C2   Intake Dam and Overflow Weirs

SECTION B-B

CHAINAGE (m)	Hf (m)	CONTROLLING CRITERION Hmin (m)
3183	0.330	0.320
3413	0.260	0.300
3492	0.190	0.290

ABBREVIATIONS:

Hf = DESIGN FLOW DEPTH ABOVE WEIR CREST.

H = REDUCED HEIGHT OF OVERFLOW WEIR ABOVE REFERENCE DATUM.

Hmin = MINIMUM REDUCED HEIGHT OF OVERFLOW WEIR ABOVE REFERENCE DATUM.

CONCRETE REMOVED

Notes: 1) Extracted from WSD drawing Nos. W10534/1B and W10534/4A.
2) Overflow Wiers W1, W3 and W5 are located at Ch. 3492, 3413 and 3183 respectively.

Figure C3   Record Drawings showing Modifications of Overflow Weirs W1, W3 and W5

Figure C4   Sub-catchment Areas with a Catchwater
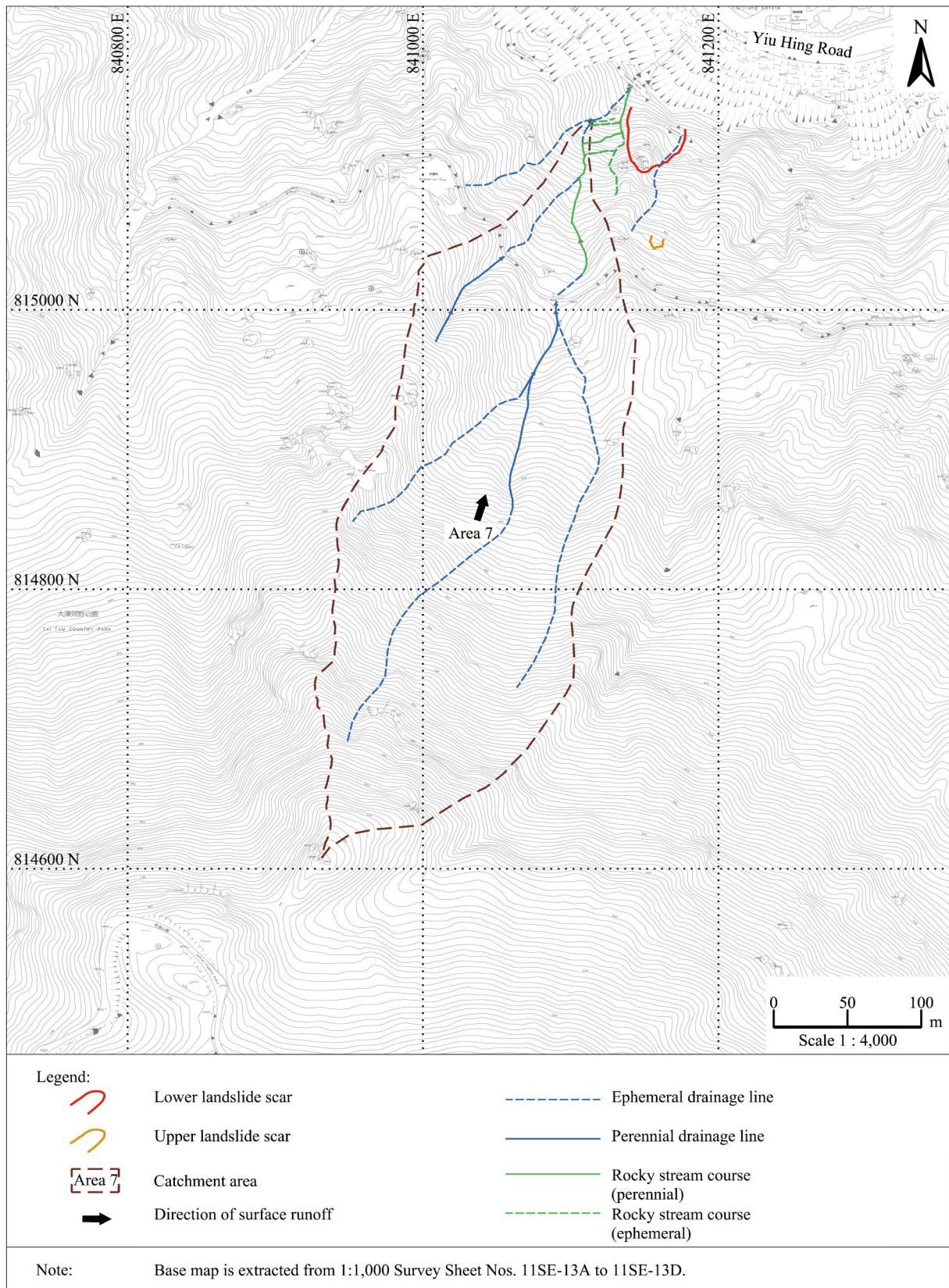
Figure C5   Catchment Area without a Catchwater

C.2 Equations

Surface runoff associated with rainfall at the time of the landslide was estimated in accordance with Geotechnical Manual for Slopes (GCO, 1984) and Stormwater Drainage Manual (DSD, 2018). The time of concentration of surface runoff (t_0) was calculated using the Bransby-Williams equation (Equation C1):

$$t_0 = \frac{0.14465L}{H^{0.2}A^{0.1}} \quad\dots\dots\dots\dots\dots\dots\dots\dots\dots\dots\dots\dots\dots\dots\dots\dots\text{(C1)}$$

where
t_0 = time of concentration of surface runoff (overland flow) (in min)
L = distance (on plan) measured along the line of natural flow between the summit and the point under consideration (in m)
H = average fall from the summit of the catchment to the point of design (in m per 100 m)
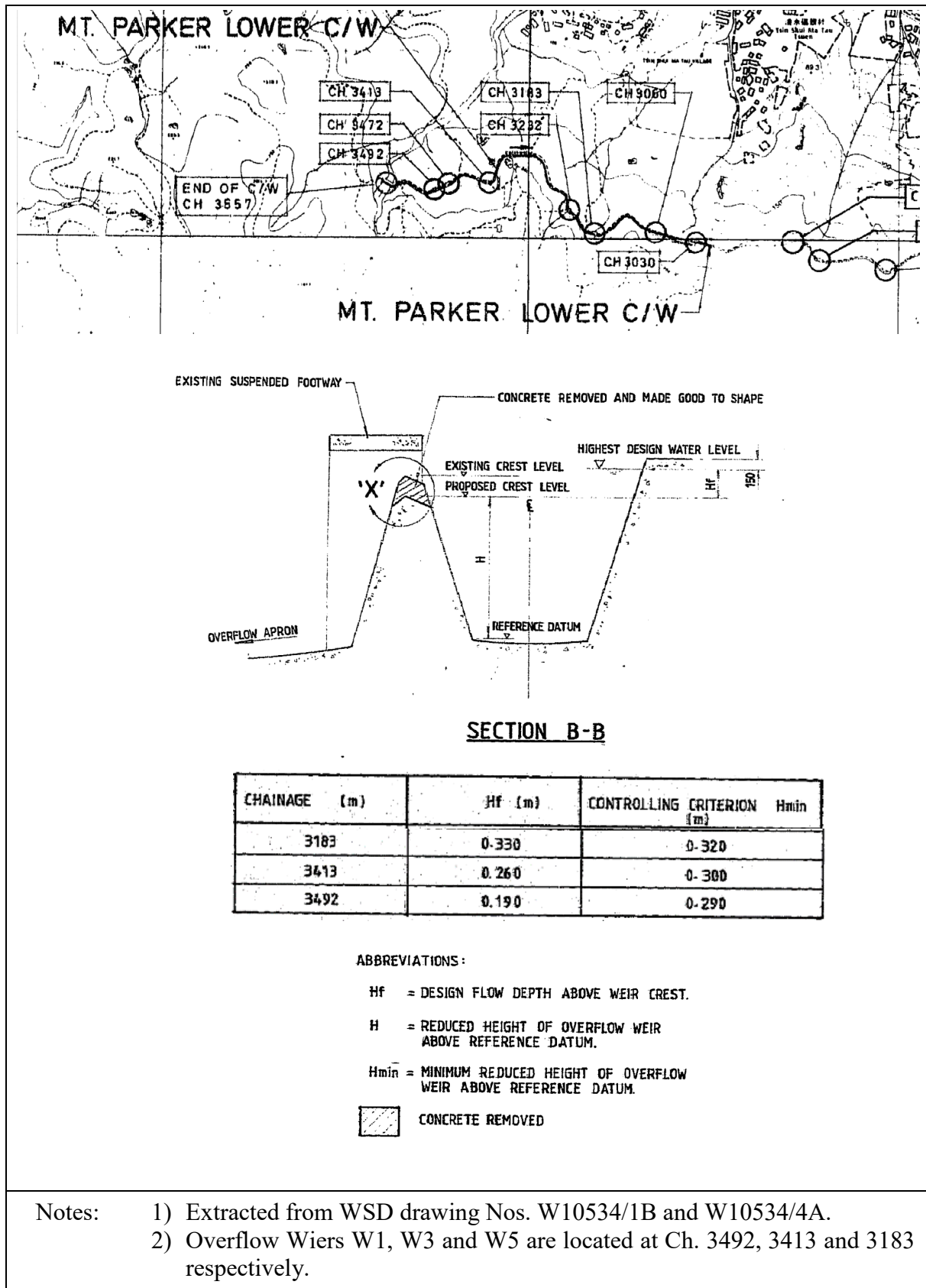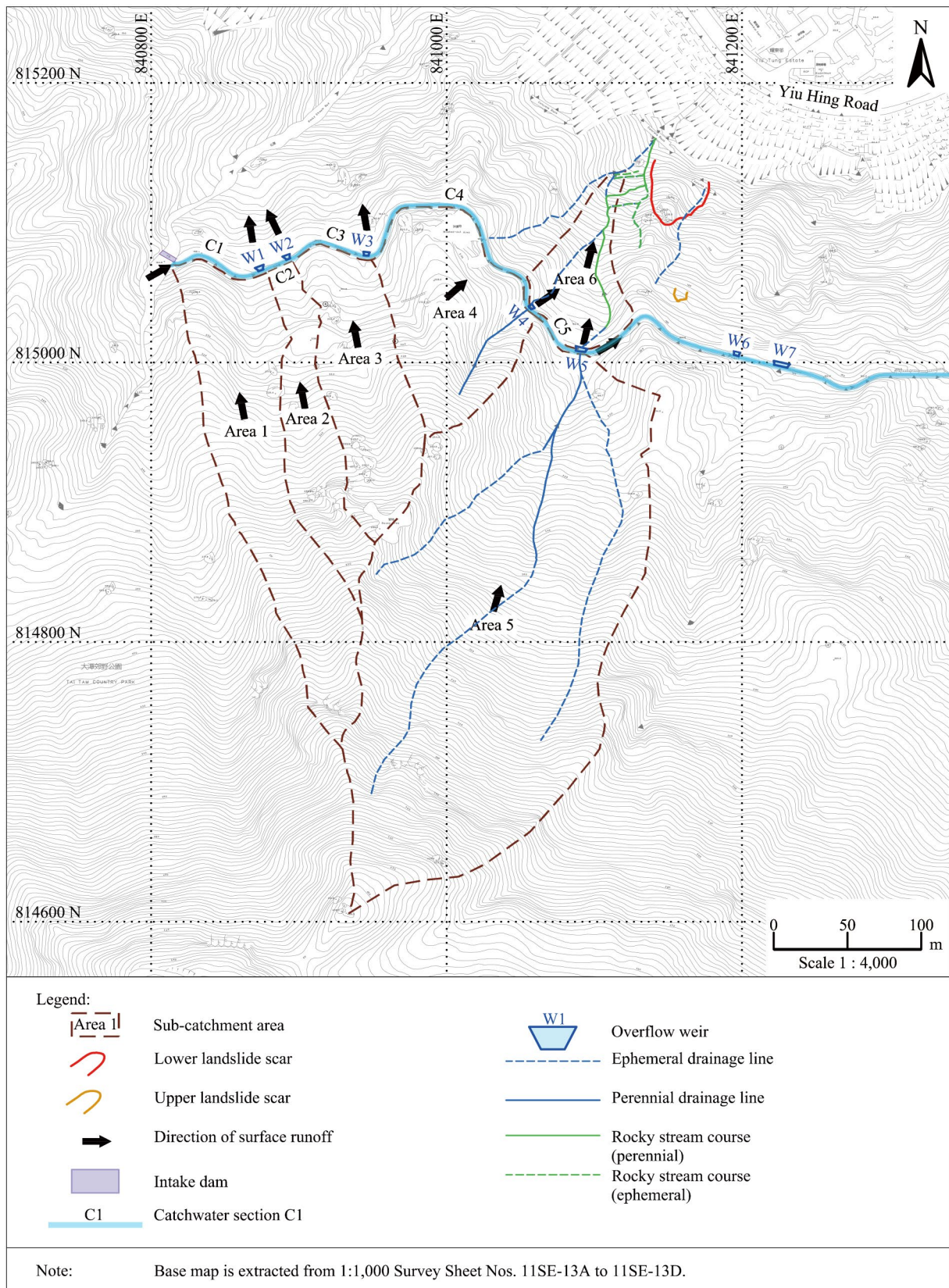A = area of catchment (in m^2)

The total time of concentration (t_c) for each sub-catchment area was calculated by adding together the time of concentration of surface runoff (t_0), the time of flow in the catchwater sections ($t_{f \cdot c}$) and the time of flow along the rocky stream course ($t_{f \cdot sc}$) adjacent to the landslide location.

The surface runoff (Q) was estimated using the Rational Method (Equation C2). Other methods are also available but they are considered less useful for Hong Kong (FSWJV, 2013).

$$Q = \frac{KiA}{3600} \quad\dots\dots\dots\dots\dots\dots\dots\dots\dots\dots\dots\dots\dots\dots\dots\text{(C2)}$$

where
Q = surface runoff (in litres/s)
K = runoff coefficient (dimensionless)
i = intensity of rainfall (in mm/h)
A = area of catchment (in m^2)

The flow velocity (v) in the catchwater and the rocky stream course was estimated using the Manning's equation (Equation C3) (GCO, 1984; DSD, 2018). The corresponding flow rate in the catchwater (Q) was calculated using Equation C4.

$$v = \frac{1}{n}[R^{0.67}S^{0.5}] \quad\dots\dots\dots\dots\dots\dots\dots\dots\dots\dots\dots\dots\dots\text{(C3)}$$

$$Q = A_w v \quad\dots\dots\dots\dots\dots\dots\dots\dots\dots\dots\dots\dots\dots\dots\text{(C4)}$$

where
v = velocity (in m/s)
n = roughness factor (dimensionless)
R = hydraulic mean depth $= A_w/P$ (in m)
P = wetted perimeter (in m)
S = gradient of channel / rocky stream course (dimensionless)
Q = flow rate (in m^3/s)
A_w = wetted cross-sectional area (in m^2)

The discharge capacity of the overflow weirs (Q) was estimated using the discharge formula for rectangular sharp-crested weirs (Equation C5) given in Bos (1989) and the empirical equation for discharge coefficient (C_d) (Equation C6) after Rehbock (1929):

$$Q = \frac{2}{3} C_d \sqrt{2g} b h^{1.5} \quad \text{..} \quad \text{(C5)}$$

$$C_d = 0.611 + 0.08(h/H_w) \quad \text{.............................} \quad \text{(C6)}$$

where
Q = discharge capacity of overflow weirs (m³/s)
g = gravitational acceleration (in m/s²)
b = weir width (in m)
H_w = weir height (in m)
h = water head above the weir (in m)
C_d = discharge coefficient (dimensionless)

C.3 Assumptions

In the estimation of surface and channel runoff associated with rainfall, the following assumptions were made:

(a) The rainfall intensity (i) was determined from the 5-minute rainfall data at GEO raingauge No. H19, which is located at about 500 m northeast of the landslide site. As the time of the landslide was about 2:36 a.m. on 8 September 2023, the 5-minute rolling rainfall data for the period ending at 2:25 a.m. was used for calculating i based on the overall time of concentration (t_c).

(b) The surface runoff was estimated using a runoff coefficient (K) of 0.9, which is applicable to steep natural slopes where a shallow soil surface is underlain by an impervious rock layer (DSD, 2018).

(c) The western end of the catchwater is connected to the intake dam intercepting the major stream course at Mount Parker (Figure C2(a)). This allows the channel runoff from the stream course to flow into the catchwater. The crest level of the intake dam is 0.67 m higher than the invert level of the adjoining catchwater, based on on-site measurements. The intake dam was assumed to be full during the severe rainstorm prior to the landslide. This assumption is considered reasonable given the high-intensity rainfall in the hours preceding the landslide. In addition, a field observation on 12 September 2023 revealed that the water level in the intake dam stood very close to the crest level, even though only minor rainfall was recorded on the day.

C.4 Calculations

The estimated times of concentration (t_0, t_f and t_c) and the input parameters used for the calculations are summarised in Tables C1 to C3. The surface runoffs (Q) for the sub-catchment areas are summarised in Table C4. The discharge rates at the overflow weirs at the time of the landslide (Q_d) are given in Table C5, whilst the discharge rates in the hypothetical scenario where the overflow weirs were not modified are given in Table C6.

Table C1   Time of Concentration of Surface Runoff

Parameter	Catchment Area / Sub-Catchment Area						
	Area 1	Area 2	Area 3	Area 4	Area 5	Area 6	Area 7
Area, A (m^2)	16,344	6,797	10,421	11,307	55,919	5,130	67,467
Distance of flow path, L (m)	343	259	214	168	439	143	566
Change in Elevation (m)	195.3	141.5	108.5	68.4	273.2	71.5	342
Average fall, H (m/100 m)	56.9	54.6	50.7	40.7	62.2	50	60.4
Time of concentration, t_0 (min)	8.4	7.0	5.6	4.6	9.3	4.0	11.9

Note: Figure C4 shows the sub-catchment areas (Areas 1 to 6) for the two scenarios (one real, one hypothetical) considering the catchwater. Figure C5 shows the catchment area (Area 7) for the hypothetical scenario without the catchwater.

Table C2 Time of Flow in Catchwater Sections and Rocky Stream Course Adjacent to the Landslide Site

Parameter	Catchwater Section [1]					Rocky Stream Course [1]
	C1	C2	C3	C4	C5	SC
Type	Trapezoidal channel					Irregular shape
Depth [2] (m)	1.0					Varies
Length [3] (m)	60.7	20.1	59.1	182.0	47.9	143
Bottom width [2] (m)	0.72	0.67	0.73	0.73	0.65	-
Gradient of sidewall [2]	1 : 0.35					-
Hydraulic mean depth, R (m)	0.317	0.276	0.290	0.262	0.325	0.121
Gradient of fall, S [3]	1 : 227					28° (average)
Roughness factor, n	0.011					0.030
Flow velocity, v (m/s)[4]	Approx. 2.7 [4]					Approx. 6.0 [4]
Time of flow, $t_{f \cdot c}$ or $t_{f \cdot sc}$ (s)	22.5	7.4	21.9	67.4	17.7	24.0
Time of flow, $t_{f \cdot c}$ or $t_{f \cdot sc}$ (min)	0.37	0.12	0.37	1.12	0.3	0.4

Notes:
(1) Figure C4 shows the catchwater sections and the rocky stream course.
(2) The depth, bottom width and gradient of the sidewalls of the catchwater sections were determined by field measurements at the weir locations.
(3) The length, and gradient of fall of each catchwater section were determined from the record drawings from WSD.
(4) Flow velocities in the catchwater sections and in the rocky stream course were determined from Equations C3 and C4.

Table C3 Total Time of Concentration for Runoff to Reach the Rocky Stream Course Adjacent to the Landslide Site

Sub-catchment Area	Elements of Time of Concentration of Surface Runoff (t_o), Time of Flow in Catchwater Sections ($t_{f \cdot c}$) and Rocky Stream Course ($t_{f \cdot sc}$) [1]	Total Time of Concentration, t_c (min)
Area 1 [2]	$t_c = t_o(A1) + t_{f \cdot c}(\text{part C1}) + t_{f \cdot c}(C2) + t_{f \cdot c}(C3) + t_{f \cdot c}(C4)$ $+ t_{f \cdot c}(C5) + t_{f \cdot sc}$	10.8 (max.)
Area 2 [2]	$t_c = t_o(A2) + t_{f \cdot c}(\text{part C2}) + t_{f \cdot c}(C3) + t_{f \cdot c}(C4) + t_{f \cdot c}(C5)$ $+ t_{f \cdot sc}$	9.2
Area 3 [2]	$t_c = t_o(A3) + t_{f \cdot c}(\text{part C3}) + t_{f \cdot c}(C4) + t_{f \cdot c}(C5) + t_{f \cdot sc}$	7.4
Area 4 [2]	$t_c = t_o(A4) + t_{f \cdot c}(\text{part C4}) + t_{f \cdot c}(C5) + t_{f \cdot sc}$	6.1
Area 5 [2]	$t_c = t_o(A5) + t_{f \cdot c}(\text{part C5}) + t_{f \cdot sc}$	9.7
Area 6	$t_c = t_o(A6)$	4.0
Area 7	$t_c = t_o(A7)$ [3]	11.9 (max.)

Notes: (1) 'A' and 'C' denote area and catchwater respectively.

(2) For example, due to the estimated flow path of surface runoff in Area 1, only the flow time for part of catchwater section C1 needs is considered. The same rule applies to Areas 2 to 5.

(3) In the hypothetical scenario where the catchwater was not constructed, only the time of concentration for surface runoff in Area 7 is relevant.

Table C4 Surface Runoff over Catchment Areas

Parameter	Catchment Area / Sub-Catchment Area [1]						
	Area 1	Area 2	Area 3	Area 4	Area 5	Area 6	Area 7
Area, A (m^2)	16,344	6,797	10,421	11,307	55,919	5,130	67,467
Runoff coefficient, K	0.9						
Rainfall intensity, i (mm/hr)	74.5						
Surface Runoff, Q (m^3/min)	18.3	7.6	11.6	12.6	62.5	5.7	75.4

Note: (1) Figure C4 shows the sub-catchment areas (Areas 1 to 6) for the two scenarios (one real, one hypothetical) considering the effect of the catchwater. Figure C5 shows the catchment area (Area 7) for the hypothetical scenario without the catchwater.

Table C5 Discharge from Overflow Weirs at the Time of the Landslide

Parameter	Overflow Weir [1]				
	W1	W2	W3	W4	W5
Weir width, b (m) [2]	2.96	3.00	2.80	2.90	6.00
Weir height, H_w (m) [2]	0.48	0.60	0.40	0.60	0.30
Water depth in catchwater (m) [3]	0.74	0.62	0.63	0.53	0.83
Water head above crest level of weir, h (m) [4]	0.260	0.016	0.229	0	0.534
Discharge, Q (m³/min) [5]	45.5	0.7	35.7	0	95.5

Notes: (1) Figure C1 shows the locations of overflow weirs.

(2) The width and height of the weirs were determined by field measurements.

(3) The water depth in catchwater was calculated from the flow rate (Equations C3 and C4).

(4) The water head (h) was taken as the level difference between the water level of the flowing water in the catchwater at the location just before the weir and the crest level of the weir.

(5) Discharge from an overflow weir was determined by comparing the discharge capacity (calculated using Equations C5 and C6) and the flow rate in the catchwater above the crest level of the weir.

Table C6   Discharge from Overflow Weirs at the Time of the Landslide in a Hypothetical Scenario where the Openings were not Enlarged

Parameter	Overflow Weir [1]				
	W1	W2	W3	W4	W5
Weir width, b (m) [2]	2.96	3.00	2.80	2.90	6.00
Weir height, H_w (m) [2]	0.67	0.60	0.66	0.60	0.63
Water depth in catchwater (m) [3]	0.74	0.78	0.69	0.73	0.95
Water head above crest level of weir, h (m) [4]	0.070	0.179	0.0027	0.130	0.321
Discharge, Q (m³/min) [5]	6.0	25.6	1.4	15.1	69.4

Notes: (1) Figure C1 shows the locations of overflow weirs.

(2) The width and height of the weirs were determined by field measurements.

(3) The water depth in catchwater was calculated from the flow rate (Equations C3 and C4).

(4) The water head (h) was taken as the level difference between the water level of the flowing water in the catchwater at the location just before the weir and the crest level of the weir.

(5) Discharge from an overflow weir was determined by comparing the discharge capacity (calculated using Equations C5 and C6) and the flow rate in the catchwater above the crest level of the weir.

Table C7 Channel Runoff in the Rocky Stream Course Adjacent to the Landslide Location at the Time of the Landslide

Scenario	Surface Runoff in the Rocky Stream Course, Q (m³/min)
Actual landslide scenario [1]	101.2
Hypothetical scenario where the openings of the overflow weirs were not enlarged in around 1995 [1]	90.2
Hypothetical scenario where the catchwater was not constructed before 1945 [2]	75.4

Notes: (1) The channel runoff in the rocky stream course was determined by adding the surface runoff from Area 6 and the discharge from Overflow Weirs W4 and W5.

(2) In the absence of a catchwater, the channel runoff in the rocky stream course adjacent to the landslide location is equal to the surface runoff from sub-catchment Area 7.

C.4 Results

Based on the assessment, the channel runoff associated with rainfall that could have reached the rocky stream course adjacent to the landslide location at the time of the landslide was about 100 m³/min. If the overflow weirs had not been enlarged in around 1995, the channel runoff at the time of the landslide would have been 90 m³/min. If the catchwater had not been constructed before 1945, the channel runoff at the time of the landslide would have been 75 m³/min. These results show that the catchwater and the modification works resulted in more runoff reaching the rocky stream course adjacent to the landslide location.

C.5 References

Bos, M.G. (1989). *Discharge measurement structures (3rd revised edition).* International Institute for Land Reclamation and Improvement/ILRI, Wageningen, The Netherlands, 401 p.

FSWJV (2013). *Review of Methods in Estimating Surface Runoff from Natural Terrain (GEO Report No. 292).* Fugro Scott Wilson Joint Venture. Report to the Geotechnical Engineering Office, Civil Engineering and Development Department, Hong Kong, 98 p.

GCO (1984). *Geotechnical Manual for Slopes (2nd Edition).* Geotechnical Control Office, Hong Kong, 302 p.

DSD (2018). *Stormwater Drainage Manual, Planning Design and Management (5th Edition)*. Drainage Services Department, Hong Kong, 193 p.

Rehbock, T. (1929). Discussion of precise weir measurement by EW Schoder and KB Turner. *Transactions of ASCE*, vol. 93, pp. 1143-1162.

Appendix D

Records of Surface Roughness Measurement and Joint Roughness Coefficients

Contents

List of Figures

Figure D1   Field Measurement of Surface Roughness and Joint Roughness Coefficients Using a Profilometer

Note: Profiles 28 and 29 could have covered pockets of infilled materials on the failure scar.
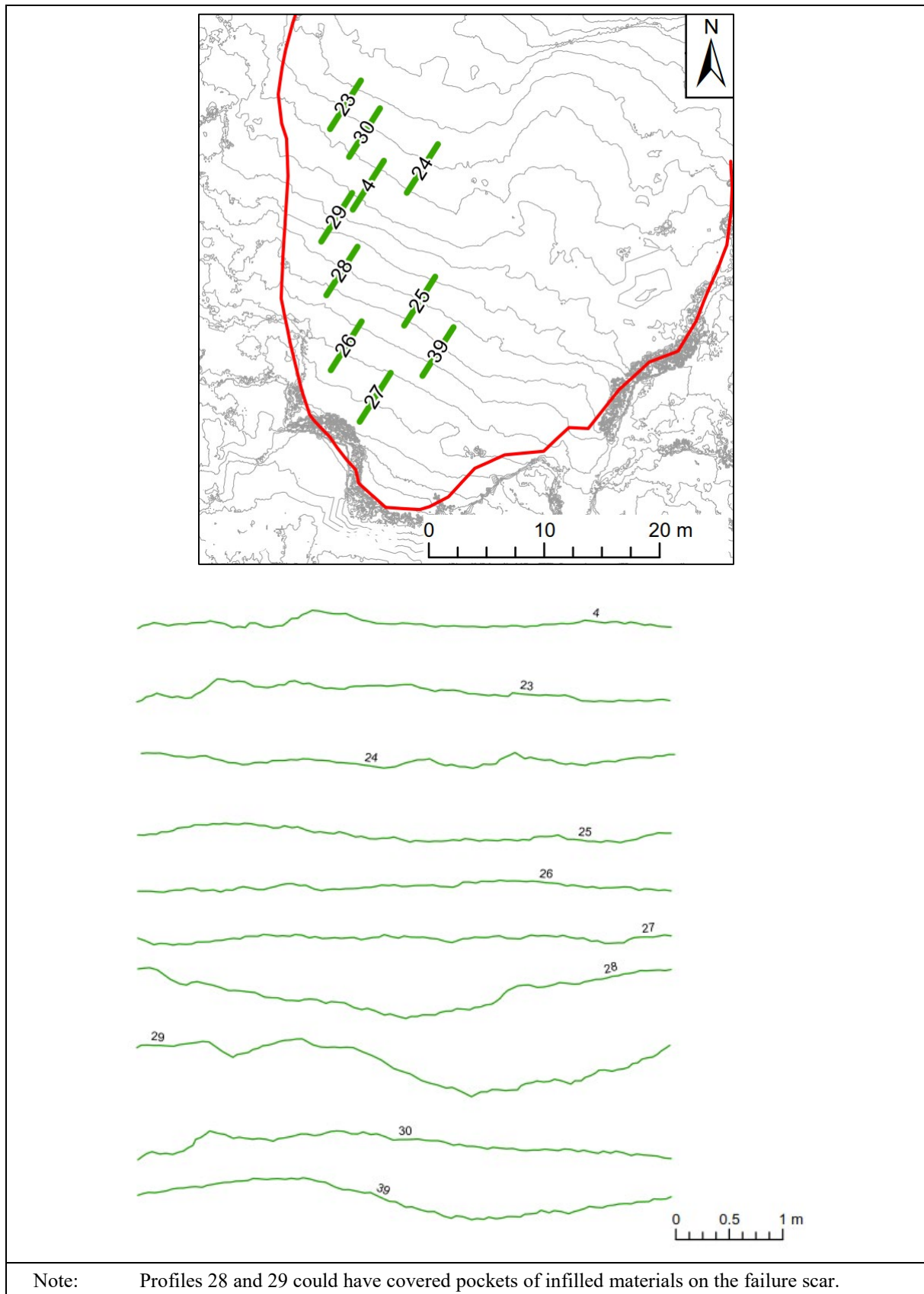
Figure D2   Surface Roughness of 5-m Profile Lines in Digital Photogrammetric Model

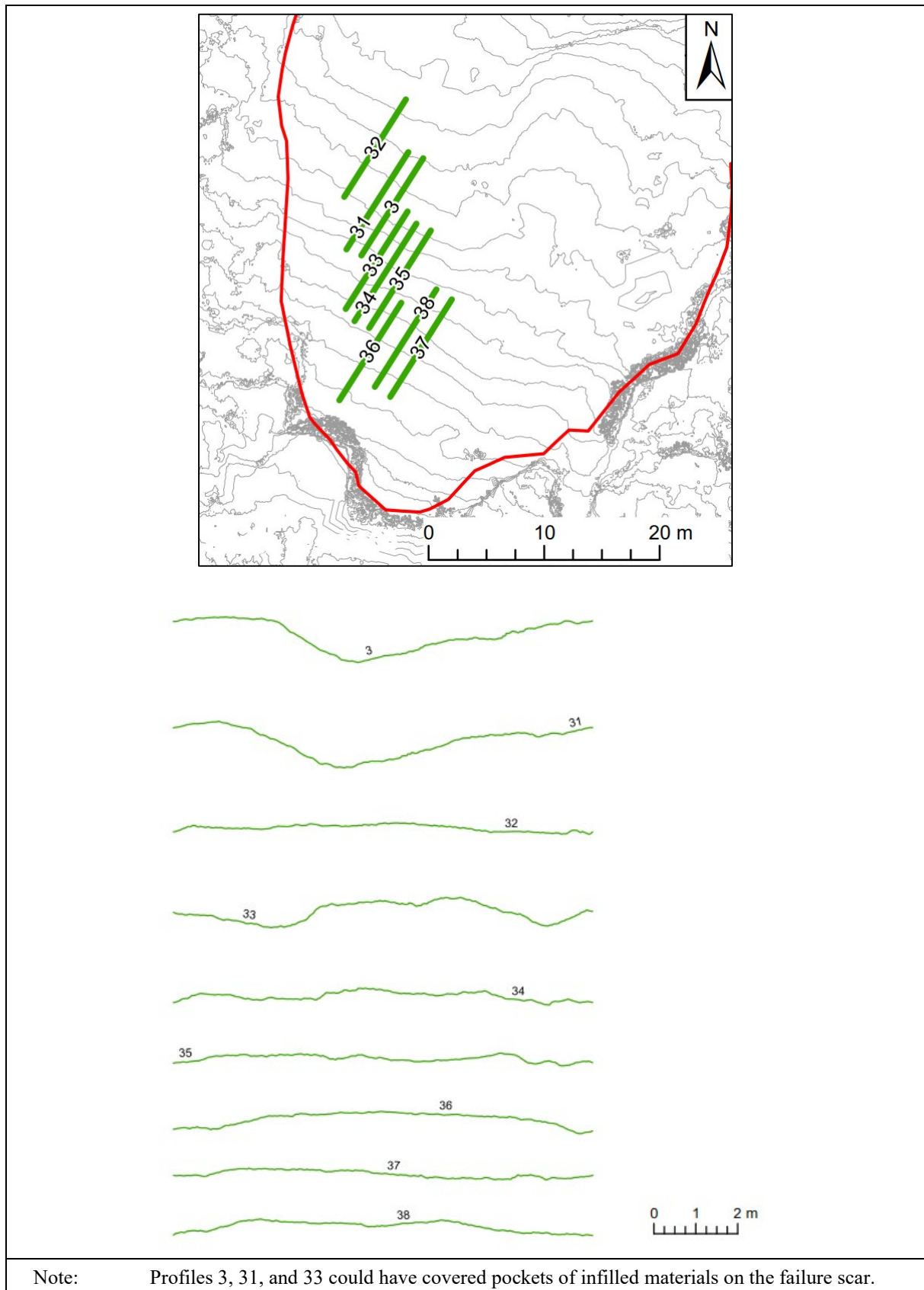Note: Profiles 3, 31, and 33 could have covered pockets of infilled materials on the failure scar.

Figure D3   Surface Roughness of 10-m Profile Lines in Digital Photogrammetric Model

Appendix E

Landslide Simulation

Contents

List of Video

Video E1   Simulation of the Lower Landslide using LS-DYNA

GEO PUBLICATIONS AND ORDERING INFORMATION
土力工程處刊物及訂購資料

An up-to-date full list of GEO publications can be found at the CEDD Website http://www.cedd.gov.hk on the Internet under "Publications" - "GEO Publications". The following GEO publications can also be downloaded from the CEDD Website:Manuals, Guides and Specifications
   i. GEO technical guidance notes
   ii. GEO reports
   iii. Geotechnical area studies programme
   iv. Geological survey memoirs
   v. Geological survey sheet reports

詳盡及最新的土力工程處刊物目錄，已登載於土木工程拓展署的互聯網網頁http://www.cedd.gov.hk 的"刊物" - "土力工程處刊物"版面之內。以下的土力工程處刊物亦可於該網頁下載：
   i. 指南、指引及規格
   ii. 土力工程處技術指引
   iii. 土力工程處報告
   iv. 岩土工程地區研究計劃
   v. 地質研究報告
   vi. 地質調查圖表報告

Copies of some GEO publications (except geological maps and other publications which are free of charge) can be purchased either by:

Writing to
Publications Sales Unit,
Information Services Department,
Room 626, 6th Floor,
North Point Government Offices,
333 Java Road, North Point, Hong Kong.

or
– Calling the Publications Sales Section of Information Services Department (ISD) at (852) 2537 1910
– Visiting the online Government Bookstore at http:// www.bookstore.gov.hk
– Downloading the order form from the ISD website at http://www.isd.gov.hk and submitting the order online or by fax to (852) 2523 7195
– Placing order with ISD by e-mail at puborder@isd.gov.hk

讀者可採用以下方法購買部分土力工程處刊物(地質圖及免費刊物除外):

書面訂購
香港北角渣華道333號
北角政府合署6樓626室
政府新聞處
刊物銷售組

或
– 致電政府新聞處刊物銷售小組訂購 (電話：(852) 2537 1910)
– 進入網上「政府書店」選購，網址為 http://www.bookstore.gov.hk
– 透過政府新聞處的網站 (http://www.isd.gov.hk) 於網上遞交訂購表格，或將表格傳真至刊物銷售小組 (傳真：(852) 2523 7195)
– 以電郵方式訂購 (電郵地址：puborder@isd.gov.hk)

1:100 000, 1:20 000 and 1:5 000 geological maps can be purchased from:

Map Publications Centre/HK,
Survey & Mapping Office, Lands Department,
6th Floor, North Point Government Offices,
333 Java Road, North Point, Hong Kong.
Tel: (852) 2231 3187
Fax: (852) 2116 0774

讀者可於下列地點購買1:100 000、1:20 000及1:5 000地質圖：

香港北角渣華道333號
北角政府合署6樓
地政總署測繪處
電話: (852) 2231 3187
傳真: (852) 2116 0774

Any enquires on GEO publications should be directed to:

Chief Geotechnical Engineer/Planning and Development,
Geotechnical Engineering Office,
Civil Engineering and Development Department,
Civil Engineering and Development Building,
101 Princess Margaret Road,
Homantin, Kowloon, Hong Kong.
Tel: (852) 2762 5155
Fax: (852) 2714 0275
E-mail: geo_publications@cedd.gov.hk

如對本處刊物有任何查詢，請致函：

香港九龍何文田公主道101號
土木工程拓展署大樓
土木工程拓展署
土力工程處
規劃及拓展部總土力工程師
電話: (852) 2762 5155
傳真: (852) 2714 0275
電子郵件: geo_publications@cedd.gov.hk